Doctoral Thesis

Study of planetary-scale waves in the Venus cloud top layer based on long-term observation with ground-based telescopes and AKATSUKI/UVI

（地上望遠鏡及びあかつき搭載紫外線カメラによる
金星雲頂部の長期観測に基づいた惑星大気波動の研究）

Masataka Imai

今井 正尭

Planetary and Space Group, Department of Cosmosciences,
Graduate School of Science, Hokkaido University

北海道大学 大学院理学院 宇宙理学専攻 惑星宇宙グループ

March 2018

Acknowledgment

I would like to express my most profound gratitude to Professor Dr. Yukihiro Takahashi for his passionate advice and comments. Millions of his words through our discussion and conversation not only help to direct my study but also grow me as a scientific researcher. I would like to extend my gratitude to Dr. Toru Kouyama for his thoughtful supports and pointed advice in scientific discussion and technical suggestions. I am deeply grateful for the many experimental instructions by Senior Lecturer Dr. Mitsuteru Sato, Associate Professor Dr. Masaki Ishiwatari, Professor Dr. Kiyoshi Kuramoto, and Assistant Professor Dr. Shunichi Kamata.

I owe a lot of efforts and supports from Associate Professor Dr. Makoto Watanabe, Dr. Seiko Takagi, and my colleague students Dr. Hikaru Nakao, Mr. Ko Hamamoto, Mr. Shuhei Gouda, Mr. Yuya Goda, Mr. Tatsuharu Ono, Ms. Yuki Futamura, and Mr. Yuki Sato, who work with me as a member of "Pirka telescope team" for managing the Pirka telescope, developing the observatory, and spending many times for observing. Primarily, I would like to express my great acknowledgment to Dr. Makoto Watanabe for his wide-ranging assists for my observation.

I also appreciate the thoughtful supports of my stay in the Nayoro-city observatory from following people; Mr. Yasuo Sano, the ex-director of the observatory, Mr. Yasuhiko Murakami, the director of the observatory, Mr. Fumitake Watanabe, Dr. Hiroyuki Naito, Mr. Katsuhito Nakajima, Ms. Yuko Kato, and Mr. Ryoma Nagayoshi.

This study could not make a good science without AKATSUKI UVI data. I am deeply grateful to the AKATSUKI project and UVI instrument team member especially, Professor Dr. Masato Nakamura, Professor Dr. Takeshi Imamura, Professor Dr. Takehiko Sato, Professor Dr. Shigeto Watanabe, Assistant Professor Dr. Atsushi Yamazaki, Dr. Shin-ya Murakami, Dr. Takao Sato, Associate Professor Dr. Takeshi Horinouchi for leading the project to a successful conclusion and providing valuable data.

I extend my sincere thanks to all of the corroborators Professor Dr. Koji Kawabata, Dr. Masayuki Yamanaka, Mr. Tatsuya Nakaoka, Ms. Miho Kawabata for supporting this study and observing Venus from Higashi-Hirosima observatory.

March 2018 (Masataka Imai)

I sincerely appreciate giving great experiences through studying Venus by Dr. Ralph Lorenz, Dr. Thomas Widemann, Dr. Pedro Machado, and I want to express gratitude to the people I meet through this study. All of the experiences with them, encourage and support my research.

I would like to thank my seniors and friends Dr. Shotaro Sakai, Dr. Yasuto Takahashi, Dr. Kensuke Watanabe, and Dr. Tomohiro Ogawa. I could have a fruitful time researching in Hokkaido Univ.

Finally, I would like to express my profound gratitude to my family for their heartfelt encouragements and supports for my study and life.

This work was supported by JSPS KAKENHI Grant Number JP17J03862.

Masataka Imai
Sapporo, Hokkaido, Japan
February, 2018

Abstract

Our neighbor planet Venus is characterized by the thick global cloud, and there are prominent fast zonal winds named the super-rotation. The winds velocity increases as a function of altitude, and it reaches 100 m/s at ∼70 km cloud top. The atmosphere rotates with ∼4 days against the 224 days rotation period of the solid globe, which means the wind is 60 times faster than the rotation of the surface. The super-rotation is controversial to explain the mechanism, and it can be an essential issue for understanding the general atmospheric dynamics on planets.

∼4-day Kelvin and ∼5-day Rossby wave are two types of planetary-scale waves observed at the cloud top of Venus with zonal wavenumber 1. They could contribute to the formation of planetary-scale features seen in at 365 nm of the unknown absorption band. During the Pioneer Venus (1978–1992) and Venus Express (2006–2014) mission periods, it was observed that the wave types changed one to another in every observational period. Since the momentum deposition by planetary-scale waves can accelerate the mean-winds, these waves could be a candidate of momentum transporter to maintain the super-rotation. Previous observations were based on the UV image of dayside. Since the spacecraft was operated in the polar orbits nearly fixed inertial space, the dayside observations were limited, and there were significant data gaps over half of the Venusian year (one Venusian year is ∼224 Earth days) between one and next observational period. The continuities of obtained data were not longer than 2–3 months, therefore, the lifetime of each wave or transient behavior of planetary-scale waves with sub-Venusian year timescales were obscured.

The purposes of this study are realizing the long-term continuous observations of planetary-scale waves on Venus and revealing the fundamental property of them such as the appearance (disappearance) and transient behavior. For these purposes, we developed an image analysis method for measuring the rotation period of planetary-scale UV features using ground-based telescopes. This method measures the latitudinal relative brightness from the equatorial to mid-latitudinal regions in both hemispheres for each image and deduces the rotation period from the cyclical variations of the relative brightness. Our method allows to neglect the extinction effect of the Earth's atmosphere, the high variability of the sky opacity, and gradual change in Sun–Venus–Earth phase angle. Additionally, this method is useful for analyzing the satellite observed images to cancel out the brightness variation caused by the different observation geometry.

We obtained the ground-based continuous data over a half Venusian year by using ground-based telescopes. Observations were mainly conducted with 1.6-m Pirka telescope, which managed by Hokkaido University, and its installed instrument the Multi-Spectral Imager (MSI) with a 365 nm narrow band filter. Pirka telescope is primarily decided for observing planets of the solar system, and it was ideal telescopes to apply for our long-term Venus monitoring in the daytime. The observational periods were divided into three; OP2015 (21/04/2015–17/07), OP2017A (03/01/2017–19/02), and OP2017B (23/04/2017–10/09). Additionally, we analyzed Venus images obtained by Ultraviolet Imager (UVI) onboard AKATSUKI (the Japanese Venus Climate Orbiter). UVI observation covered partially the same periods of the ground-based as OP2017A (06/11/2016–02/03/2017) and OP2017B (15/06/2017–31/09). Over 300 days continuous data from December 2016 to September 2017 was investigated in this study, with only 50 days data missing interval in March and April 2017.

The periodicities in the relative brightness variations were analyzed to investigate the continuous existence of planetary-scale waves. Periodical analysis of unevenly sampled data was conducted with Lomb-Scargle periodogram Scargle [1982]. To capture the continuous variability in periodicity through the observational periods, we made sub-dataset with $\pm$14 days shifting window and stepped it with the 1-day interval. Thus, our final obtained results have the information of periodicity as the function of time. Three latitudinal bands of EQ (10°S–10°N), SM (50°S–30°S), and NM (30°N–50°N) were investigated, and it was validated that ground-based and space-based data has a high agreement and directly comparable.

In most of our observational periods, two prominent modes with 3.5–4.0-day and 5-day period were confirmed. The 3.5–4.0-day modes were observed mainly and tended to survive for a longer time. In contrast, 5-day mode sporadically appeared and sometimes last longer than 30 days. We estimated zonal wind velocity at the cloud top for each latitudinal bands with 1° width. This method tracks the zonal displacements of mesoscale cloud features maximizing 2D cross-correlation between two images separating by $\sim$2 hours. The estimated zonal mean-wind velocity was $\sim$100 m/s, which corresponds to the 4.4-day period rotation around the planet at the equator, and observed modes could be classified as faster (westward) propagating wave against mean-winds with 3.5–4.0-day period or slower (eastward) propagating wave with a 5-day period. Following previous studies (e.g., Del Genio and Rossow [1990]; Kouyama et al. [2015]), the faster mode should be equatorial Kelvin wave,

and the slower mode was suggested as Rossby wave in mid-latitudes.

It was confirmed that wave transient occurred within a sub-Venusian year, and observed wave transient behavior in this study could be classified into two types. One is completely mode transient from 4-day to 5-day with ∼20 days interval. The other one is continuous periodicity change from 4-day to 5-day, where 4-day mode was continuing, and double-mode was observed at the moment. Since the zonal mean-wind during the observational periods were almost constant at ∼100 m/s at the cloud top, the vertical propagation of planetary-scale waves is not controlled by the zonal mean-wind velocity near the cloud top as proposed by Kouyama et al. [2015]. The periodicities in the fluctuations of equatorial zonal winds were distinctly different from that in the brightness variation in the equatorial region. One of the interpretation is that 5-day wave in mid-latitudes has the more significant amplitude of fluctuating winds than 4-day wave at the equator. In parallel, another explanation is acceptable that the 4-day wave observed with planetary-scale features reflects at a lower altitude than the that of the 5-day wave measured by mesoscale cloud tracking. Kelvin wave is expected to decay during the vertical propagation because the zonal mean-wind velocity becomes faster at higher altitudes or the strong radiative dumping is work. Thus Rossby wave could survive at a higher level than where Kelvin wave can propagate. The wave source and wave transition mechanism are still unclear, but the second explanation is qualitatively in the case. Therefore these facts possibly indicate that some momentum energy flow from Kelvin wave to Rossby wave occurs at lower altitudes.

Contents

List of Figures

List of Tables

1 General Introduction

1.1 About Venus

To understand the atmospheric dynamics on planets, the orbital eccentricity, obliquity to the orbit, which is important for the latitudinal balance of the solar energy, and the rotation speed of the solid globe are key parameters. In the case of Venus, the eccentricity and obliquity are 0.006 78° and 177.3°. Ttherefore, solar flux varies by only 2.8% during the revolution, and considerable seasonal variations are small. The orbital and rotation periods of Venus are 243.0 Earth days (after this used as "days") and 224.7 days respectively. The direction of the rotation of Venus is retrograde (globe surface moves westward) which is opposite direction compared to most of the other solar planets. Parameter comparisons between Venus and the Earth including major physical characteristics are summarized in Table 1.1.

Since Venus is an inferior planet, the Venus–Earth distance and Venus illuminated phase (Venus–Sun–Earth) angle largely change. The synodic period of both planets is 584.0 days, which is the time interval between one and the next inferior conjunction, is longer than 2 Venus year. Figure 1.1 illustrates the orbit of Venus (left) and the orbital relationship between Venus and the Earth (right). Venus–Earth distance and phase angle change largely during one cycle of a synodic period, and there are two times of opportunity for observing dayside of Venus (see Section 2.2).

Table 1.1: Physical parameters of Venus and the Earth. Data listed in this table is obtained from JPL's HORIZONS system or their supplemental documents.

	Venus	Earth
Mean radius [km]	6051.84	6371.01
Mass [10^{-24} km]	4.8685	5.97219
Density [g/cm^3]	5.204	5.515
Equ. gravity [m/s^2]	8.870	9.7803267715
Sidereal rot. per. [day]	-243.0185	365.25636
Mean solar day [day]	116.7490	1.002738
Sidereal orb. per. [day]	224.70079922	365.25636
Distance from the sun [AU]	0.72333566	1.00000261
Eccentricity	0.00678	0.0167
Obliquity to orbit [deg]	177.3	23.45
Inclination to Sun's equator [deg]	3.86	7.155
Atmos. pressure [bar]	90	1.0
Mean Temperature [K]	735	270
Geometric albedo	0.65	0.367
Planetary Solar Const [W/m^2]	2613.9	1367.6

Because of the similarity of the physical characteristics of the solid planet (e.g., mass, size, and density) between Venus and the Earth, we sometimes call Venus as a twin of the Earth. However, Venus is covered by thick global clouds, which locate from ∼50 to ∼70 km altitude range, and hazes above the clouds. The main composition of the clouds is H_2SO_4 droplets. 96% of the atmosphere consists of CO_2 and remains are N_2, CO, CO, H_2O, Ar, and SO_2. Due to the extreme greenhouse effect of CO_2 and dense atmosphere, the surface temperature and pressure are 700 K and 90 bar respectively. Figure 1.2 shows a typical profile of temperature and pressure versus altitude. The troposphere is the near surface area, where temperature decreases with altitude and is under convective equilibrium as the Earth. In the case of the Earth, there is an ozone layer in $\sim 10^0$ bar (15–30 km altitude) above the troposphere, where oxygen molecules or ozone are dissociated into atomic oxygen by absorbing solar EUV (Extreme ultraviolet), and atmospheric heating occurs. Therefore, the temperature increase with altitude in that layer and we distinguish it as the stratosphere. Generally speaking, there is no local temperature maximum, and the atmosphere is stably stratified in the stratosphere, and the radiation process takes the dominant role in heating and cooling compare. The cloud top region is in radiative equilibrium where the photochemistry is essential, and haze layer produced

and is nearly isothermal. The mean lapse rate is ∼8 K km^{-1} which is the highest value within the solar system.

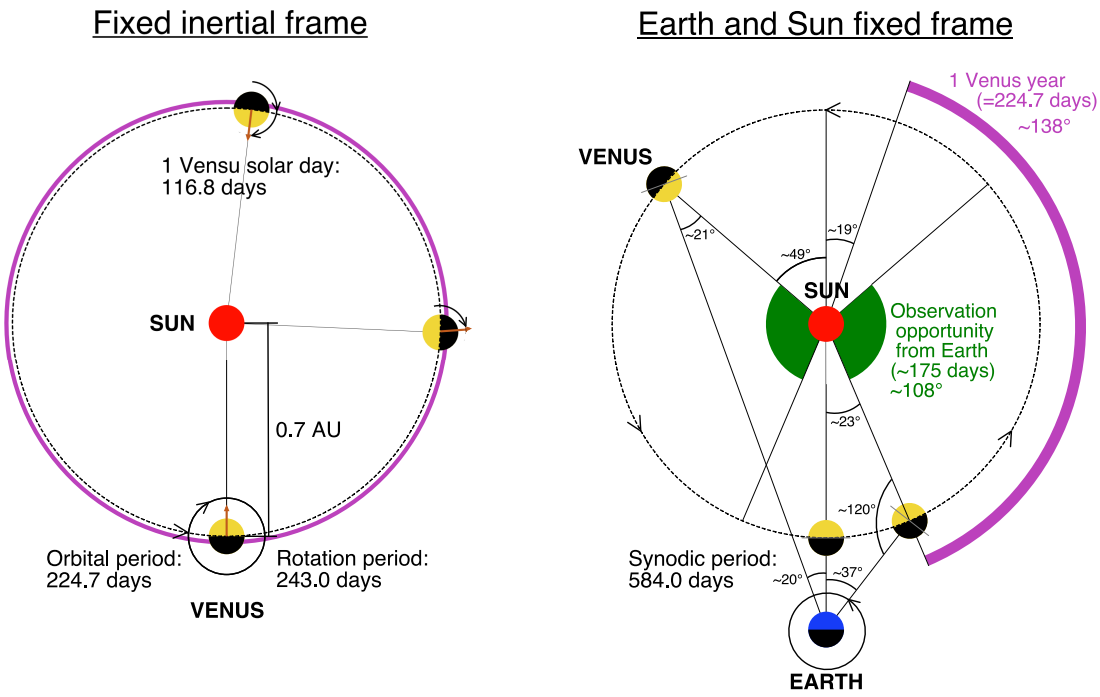

Figure 1.1: Illustrations of Venus orbital properties and geometries. In the left figure, a radial direction to a specific longitude from Venus center is shown with orange arrows, and Venus–Sun geometric relationship during a 1 Venus solar day is depicted in a fixed inertial frame. The right figure shows geometric relationship within one synodic period of 584.0 days between Earth and Venus as drown the Earth and Sun are in a fixed position in the figure. Observational opportunities for this study are shown with green fan shape area, and typical angular conditions are denoted.

On Venus, 200% of solar energy incoming relative to the Earth (100%). In total, 152% of the energy is reflected by the surface, clouds, and the atmosphere. 42% of the energy is absorbed by the atmosphere, but that is only 6% by the surface (in the Earth case, 20% and 50% respectively), therefore, more than 85% of the solar energy absorption occurs in the atmosphere. However, it is less than 30% on the Earth. The atmosphere of Venus is entirely different from that of the Earth, and this kind of difference leads to the unfamiliar atmospheric dynamics on Venus. Mainly, we focus on the prominent planetary-scale UV absorption features on the cloud top level (Section 1.3), and the remarkable fast global winds named the super-rotation (Section 1.4).

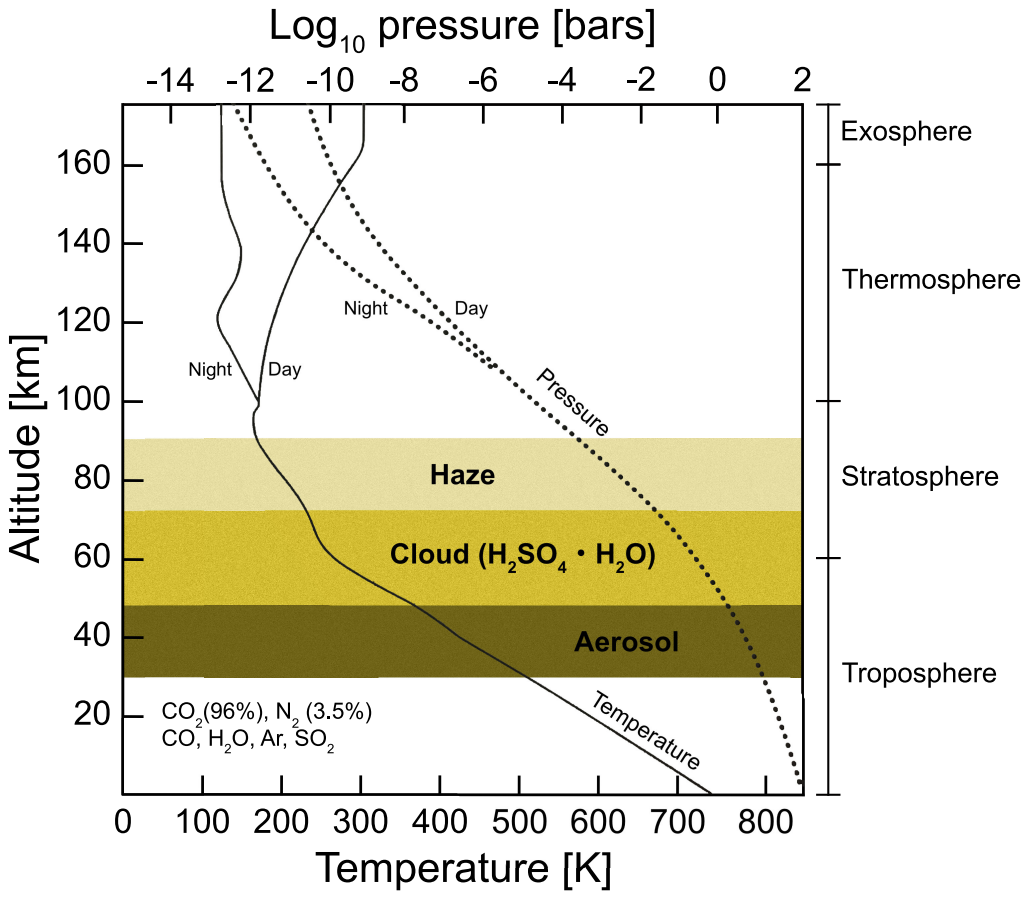

Figure 1.2: A schematic illustration of the structure of Venus atmosphere with the vertical profile of temperature and pressure. Basic information is referred from a book –Taylor, F. W., 2014. *The Scientific Exploration of VENUS*. New York: Cambridge University Press.

1.2 Exploration of Venus

Before going into the detail of the meteorological phenomena on Venus, the key space mission exploring Venus is introduced. Here we summarize the observational instruments used for monitoring the cloud motions in UV wavelength.

Pioneer Venus & OCPP

The Pioneer Venus mission was signed by NASA (National Aeronautics and Space Administration) in 1974, and the spacecraft placed in Venus orbit on December 4, 1978, (Colin [1980]). Pioneer Venus was in a high eccentricity, nearly polar and 24-hour orbit with small perturbations during its 14-year lifetime. The orbiter cloud photopolarimeter (OCPP) instrument onboard Pioneer Venus orbiter (the mission

consists of the 'orbiter' and 'multiprobe bus') uses a positionable 3.7 cm Cassegrain telescope, and by measuring the viewing angle from the spacecraft spin axis, the instrument conducted two-dimensional coverage spin scanning while the spacecraft orbital motion. This imaging mode uses a 365 nm filter with 0.4 by 0.45 mrad aperture with a single photodiode detector, and the typical resolution was 30 km at the sub-spacecraft point TRAVIS et al. [1979]. The instrument was optimized to use the long apoapsis portion of the orbit, where the spacecraft longitude varies only small range. Therefore, the favorable illumination geometry for imaging (the phase angle was lower than 60°.) occurs during approximately 100 days out of the 225-day Venus year. Before the Pioneer Venus era, Mariner-10 obtained first high-resolution UV image but only for eight days, and OCPP firstly permitted to observe large-scale cloud morphology, measure the cloud-tracked winds and wave propagation in the atmosphere over several months.

Venus Express & VMC

Venus Express was the first European mission to Venus by ESA (European Space Agency) and arrived at Venus in 2006. The spacecraft was inserted into an elliptical polar orbit with a 24-hour period. The apocenter distance was ∼66,000 km, and the pericentre altitude was in the 250–350 km range. The pericentre was placed near the North pole. Thus the Venus Express observations combined a global and view of the planet with less variation of observing geometry in the southern hemisphere and high resolving snapshots in the northern hemisphere. Venus Monitoring Camera (VMC) was a wide-angle camera with the ∼17.5° field of view, and the spatial resolution varied from ∼50 km in apocenter to a few hundred meters in pericentre. VMC had four channels of UV (365 nm), visible (513 nm), near-IR of water vapor band (965 nm) and that of the continuum (1010 nm). During the eight years long mission life, VMC captured many images and succeeded to reveal the long-term global changes especially in zonal winds, and the mission was finished at the end of 2014.

AKATSUKI & UVI

AKATSUKI (Figure 1.3) is the Japanese Venus Climate Orbiter, which was launched on May 21, 2010. On December 7, 2010, the initially planned orbit insertion was failed because of the trouble of the orbital maneuver engine, and five years later on December 7, 2015, the orbit re-insertion succeeded. After the orbit insertion, several period control maneuvers were conducted, and the current orbital period is 10.8 days with orbital altitudes at pericentre and apocentre are 1,000–10,000 km and 370,000 km respectively Nakamura et al. [2016]. This alternative orbit of AKATSUKI is

high elliptical of which inclination is <10° inclination having the advantage to observe lower latitudes compared to Venus Express. AKATSUKI equips five cameras, ultraviolet imager (UVI; Figure 1.4), 1 µm infrared camera (IR1), 2 µm infrared camera (IR2), Long-wave infrared camera (LIR), and lightning and airglow camera (LAC). Former four cameras obtain the Venus images using different wavelength and enable to reveal the cloud motions at different altitudes. As the prior ultraviolet instruments OCPP and VMC, UVI captures high contrast cloud features usable for measuring cloud-tracked winds with 365 nm of unknown and 283 nm of SO_2 absorption bands. The large variety of the observation geometry provides global imaging, close-up imaging, and limb imaging.

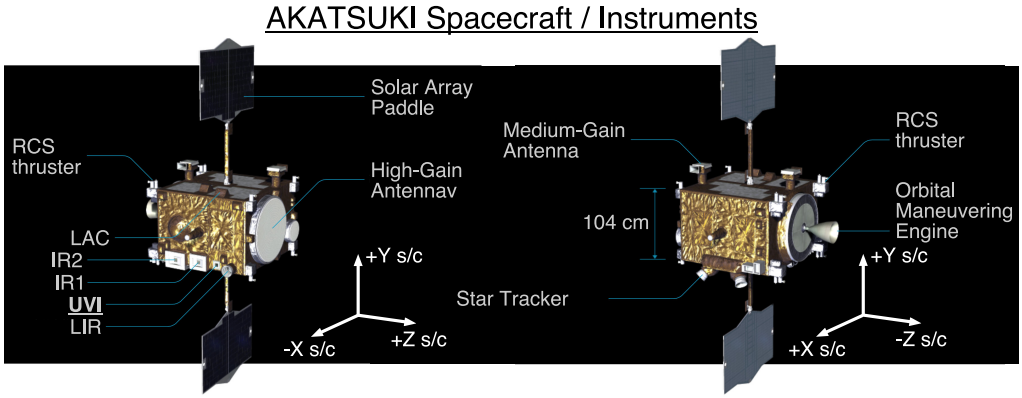

Figure 1.3: The outer appearance of AKATSUKI spacecraft and onboard instruments. Used graphics are obtained from the official AKATSUKI mission web site: http://akatsuki.isas.jaxa.jp/en/mission/spacecraft/

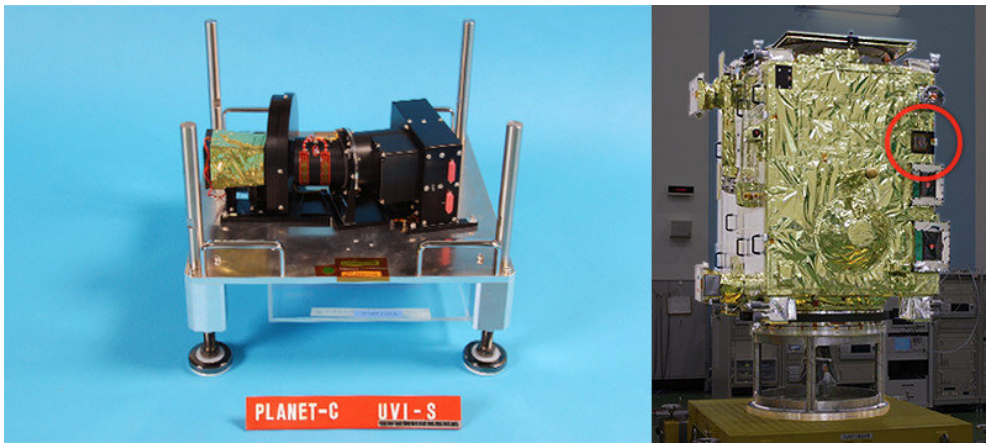

Figure 1.4: Pictures of the UVI instrument.

1.3 UV absorbers and planetary-scale UV features

Venus reflects and scatter the light from the sun and is seen as is a bright yellow planet without prominent feature at the visible wavelength. However, when we observe Venus in UV range, we can find the various scale of cloud features on the disc. Figure 1.5a is a recent UV image of 365 nm taken by UVI/AKATSUKI. There are large-scale features, and the combination of longitudinal bright and dark patterns in low latitudinal regions and the sharp, bright and dark boundary from ∼60° to ∼30° in both hemispheres form prominent planetary-scale features.

It can be confirmed that the higher latitudinal regions than ∼45° are brighter at this wavelength (e.g., see Fig.1 of Peralta et al. [2007]). By the Pioneer Venus era, this kind of planetary scale feature is well known, and since it looks like a sideways character "Y," this feature sometimes called as Y- or ψ- feature. Figure 1.5b is the high pass filtered image of 1.5a. In the equatorial region, the turbulent and convective features are prominent, and in contrast, there are many streak features at midlatitudes. Several types of features observable in UV wavelength are illustrated in Figure 1.6, which was drown based on Pioneer Venus images, such as s dark equatorial band including small patchy cells, bow shapes, dark midlatitude bands, and bright polar bands.

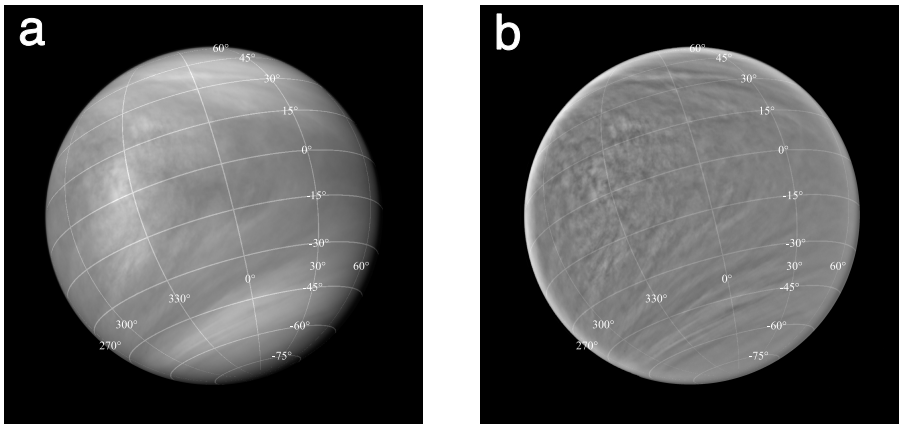

Figure 1.5: Venus UV image (uvi_20170126_073446_365_l2b_v20171201) taken by UVI in the 365 nm filter with graticule. Left figure is a original image and right figure is high-pass filtered one.

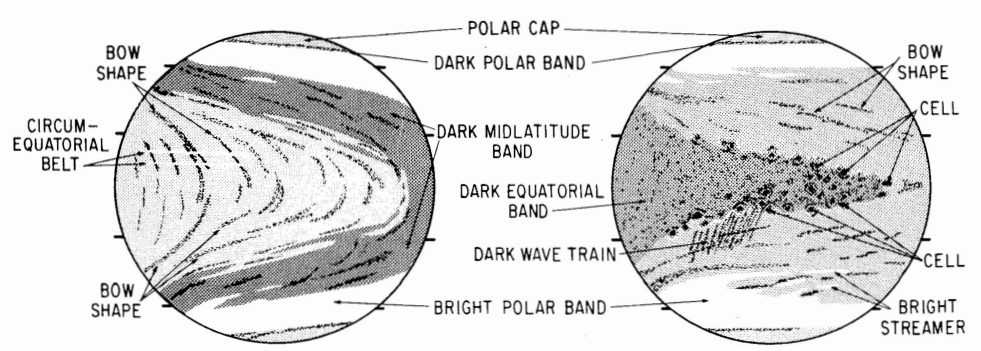

Figure 1.6: Schematic illustration of several types of UV features on Venus cited from Rossow et al. [1980]. The planetary-scale Y-feature does not always keep the constant shape and is considered variable.

It has been known for a long time some UV absorber(s) exist in the Venusian clouds, and it is responsible for the low UV albedo and dark features. SO_2 is the strong candidate for the absorption shorter than 320 nm. However, it is still controversial the substance absorption longer than 320 nm, e.g., Bertaux et al. [1996]; Pollack et al. [1980]. Figure 1.7 shows the monochromatic albedo of Venus. The solid line (or dashed lines) are the result of ground-based spectrometry summarized by Barker et al. [1975] showing a steep decline in 300–500 nm and indicating broad absorption band between 320 nm and 400 nm.

Esposito [1980] showed Venus in UV range is darkest at the nadir point, which means instruments line of sight penetrates the cloud tops perpendicularly. It can be confirmed any Venus UV images and suggesting a substantial amount of absorbing material(s) exists in the deep cloud layer. Based on the in-situ measurements with photometric instruments carried by Venera-13 and -14, 90% of UV flux absorption occurs above 60 km altitude, and the rest of absorption does between 55 km to 48 km Ekonomov et al. [1984]. VEGA 1 and 2 entry probes also measured the UV opacity excluding the SO_2 absorption band, and the results indicated that the unknown absorber concentrate just above the lower cloud deck at 47 km Bertaux et al. [1996] (see Figure 1.8). Since previous in-situ measurements were less reliable above the 60 km altitude, the vertical distribution of unknown absorber around the cloud top layer is poorly understood. However, it is believed that the unknown absorber well concentrates in middle and lower cloud layer, and Molaverdikhani et al. [2012] proposed that they are well-mixed above $\sim$63 km or they exist as a thin pure layer at $\sim$71 km near the cloud top altitude.

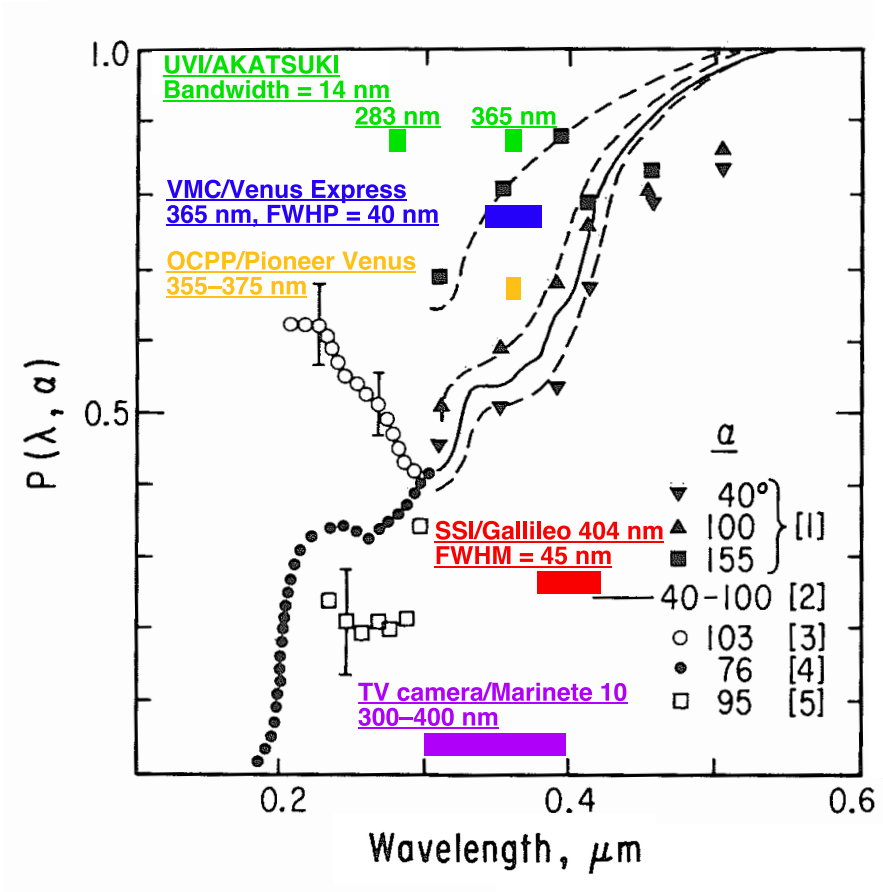

Figure 1.7: The monochromatic albedo of Venus as a function of wavelength the relative geometric albedo is given according to the data of [1] Irvine 1968] [2] Barker et al. 1975 [3] Anderson et al. 1969 [4] Wallace et al. 1969 [5] Evans 1966 [6] Sinton 1963b [7] Moroz 1964 [8] Pollack et al., 1978. α is the phase angle Original figure was obtained from V. I. Moroz Venus book, and additional information of the coverage of the instruments onboard, Mariner-10, Galileo, Venus Express AKATSUKI are included.

The contrast of Venus UV feature is empirically known to be high at 365 nm which cannot be explained by the SO_2 absorption. Instruments onboard Venus explorers equipped UV filters whose center wavelength is ∼365 nm as shown in Figure 1.7, and UV features have been used as tracers of the cloud top winds for a long time.

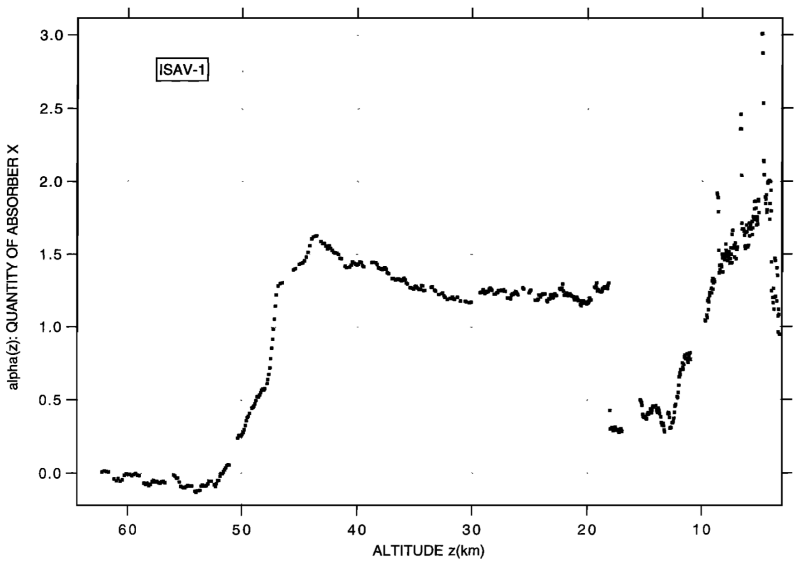

Figure 1.8: The relative opacity of the unknown UV absorber as a function of altitude measured by VEGA 1 entry probe. Plotted data is based on the differential of quantitive absorption data in the wavelength bins 331–394, where SO_2 absorption is negligible Bertaux et al. [1996].

There is some difficulty in estimating the cloud top altitude, and the temporal variation in cloud top altitude is still not clear. The earlier estimated altitude was 66–72 km, but it has not been clear whether the global pattern arises from differences in cloud top altitude, compositional variations or temperature contrasts. The multi-wavelength observation using VMC and infrared (1–5 µm) mapping spectrometer VIRTIS onboard Venus Express revealed that the measured cloud top was the remarkably constant altitude of 72 ± 1km in low and middle latitudes, and there is no correlation with the UV dark and bright pattern. Therefore, it was suggested that the UV brightness variation is not a result of the elevation change Titov et al. [2008] (Figure 1.9). The following processes can be considered to cause the regional or local brightness variation (a) waves (from mesoscale ∼100 km to planetary scale ∼10,000 km), (b) solar tides, and (C) Chemical process or compositional change. Consequently, the UV images include both periodic cloud patterns identifying the phase velocity of waves and cloud-tracked winds for retrieving the background winds velocity. Additionally, since small cloud movements tell us the information of background winds, the cloud top altitude or the altitude where UV features exist is important for estimating winds velocity by cloud tracking method. Cloud tracking method is widely developed by several works, e.g., Horinouchi et al. [2017]; Ikegawa

and Horinouchi [2016]; Khatuntsev et al. [2013], and most of them used 65 km as the reference altitude.

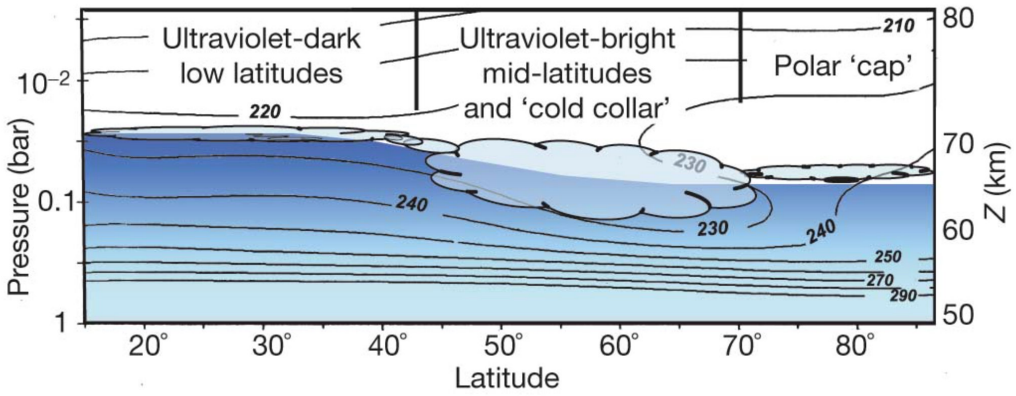

Figure 1.9: Illustrates of the global morphology of Venus cloud top altitude from Titov et al. [2008]. Conservatively scattering ultraviolet-bright cloud is shown in light blue, and the ultraviolet-absorbing layer is in dark blue.

1.4 Super-rotation

1.4.1 Basic characteristics

UV features on Venus were firstly detected in 1911 by Quénisset [1921] using photographs, and since then, several ground-based telescopes (for example see Dollfus [1975]) observed the movements of the features. In the 1960s, a recurrence of the UV pattern namely the planetary scale of the Y-feature was recognized with exactly 4 days, and a rapid retrograde rotation of Venus upper atmosphere in four days was widely known [Boyer and Camichel, 1961]. In 1973, Mariner-10 closed to Venus at a distance of 10,000 km and succeeded to provide Venus images from space. These well spatially resolved images allowed to determine global circulation at the cloud top, e.g., Limaye and Suomi [1981]. Figure 1.10 is one of the early work measuring the angular velocity of ∼3.5–4.0 days period in zonal winds as a function of latitudes.

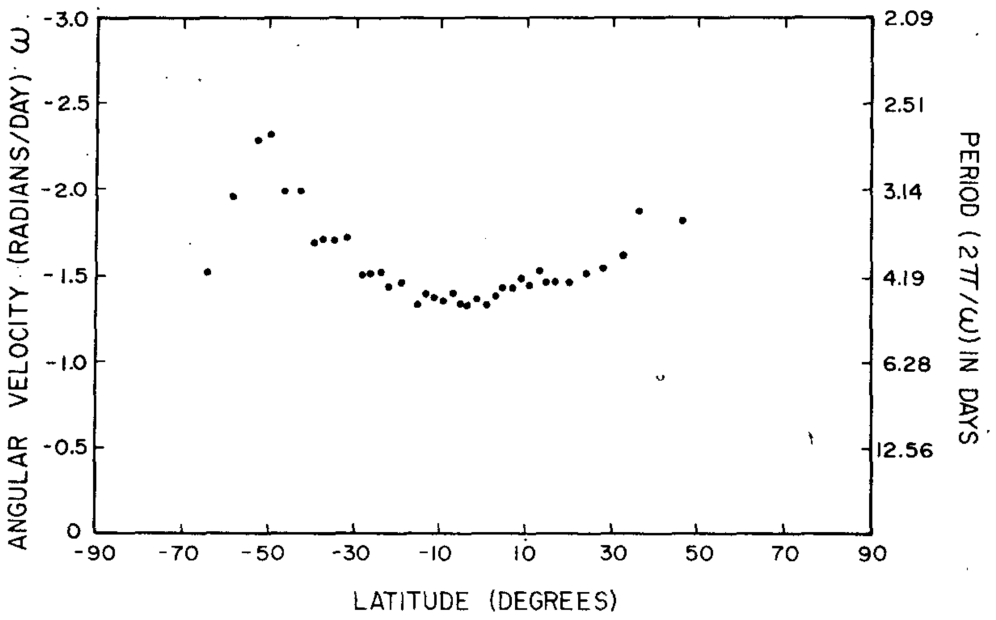

Figure 1.10: Latitudinal profile of longitudinally averaged zonal component over the Mariner-10 observation period. An equatorial mean is ∼97 m/s, and ∼108 m/s at 50° latitudes in northern hemisphere Limaye and Suomi [1981].

Around that time, the rotation period of the solid globe was measured by the Earth-based radar experiment. Shapiro et al. [1979] summarized the data gathered between 1964 and 1977 and reported the resulting rotation period is 243.01 ± 0.03 days. It was also measured by using Magellan radar images acquired from August 1990 to September 1992, and the result showed a rotation period of 243.0185 ± 0.0001 days Davies et al. [1992]. These facts mean that the Venus atmosphere rapidly moves in the westward direction, reaching velocities 60 times faster than the rotation velocity of the solid globe. This fast atmospheric flow against the solid globe rotation is now called the super-rotation, and it is unique phenomena in the solar system.

Various types of wind measurements were applied for understanding the Super-rotation phenomena on Venus, and three-dimensional structure of wind fields. The detail of each technique is well summarized in Table 1 in a review paper of Sánchez-Lavega et al. [2017]. Here, we should note that these wind measurements only showed a snapshot picture. Since there is a limitation of available observation data, the continuous and long-term behavior of winds and relevant phenomena are still poorly understood.

Figure 1.11 is typical examples of the retrieved wind data. The left figure shows the vertical profile of zonal winds by the measurement of Doppler shifted radio wavelength by descending probes. These are the only methods to know the winds lower than 45 km altitudes of the cloud deck. The middle figure is a recent cloud-tracking result using AKATSUKI data. The cloud-tracking method is the most common and widely developed approach to the Pioneer Venus, Venus Express, and AKATSUKI era. We assume small features as passive tracers of flow and measure the horizontal winds. The right figure depicts the comparison of cloud-tracked winds velocity and that of determined from ground-based Doppler-shifted lines. Measuring the shift of the Fraunhofer solar spectrum or CO_2 absorption allow sounding 65–75 km near the cloud top altitude.

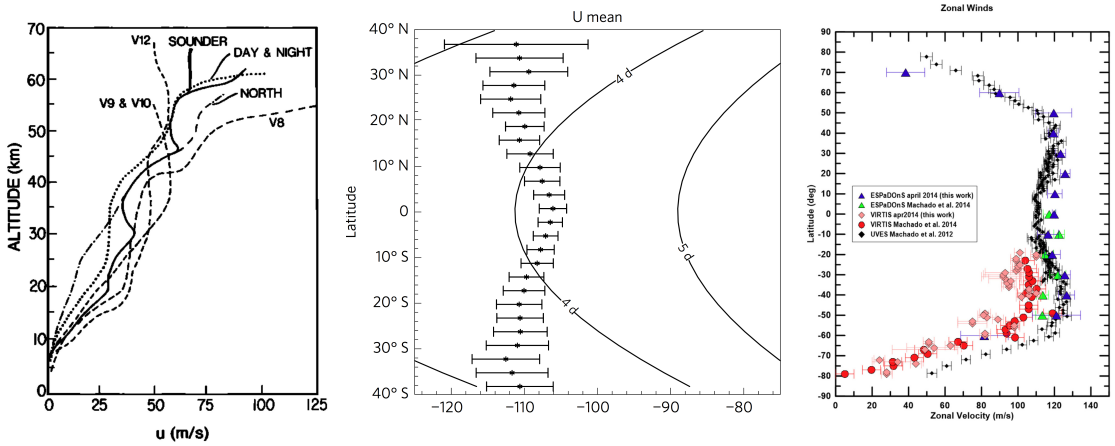

Figure 1.11: Observational results of winds velocity (left) winds profile from the direct measurements by descending probes Schubert et al. [1980]; (middle) latitudinal zonal winds velocity in middle cloud layer by cloud tracking method Horinouchi et al. [2017]; (right) latitudinal zonal winds velocity at the cloud top layer taken by ground-based spectroscopy and accompanying comparable data from spacecraft measurements by Machado et al. [2017]

1.4.2 Proposed mechanism

The important point of understanding the super-rotation mechanism is to reveal how the angular momentum being transported. In the case of Venus, since the fast zonal flow is dominant, the longitudinal thermal gradient can be small, and only the meridional circulation is considered playing an important role. Here we pick up the brief introduction of the proposed mechanism of super-rotation reviewing Sánchez-Lavega et al. [2017].

There is a classical scenario illustrated as the "Gierasch-Rossow-Williams mechanism" (Gierasch [1975]; Rossow and Williams [1979]). The basic concept is founded on the effect of a thermally-direct, axisymmetric overturning circulation which has the same form of meridional circulation as shown in Figure 1.12A. The circulation is led the prograde (westward) zonal flow at higher levels and spinning-up the flow in mid-latitudes from equatorial to the pole. There is a problem that the depleting of the angular momentum occur in the equatorial region, and Gierasch [1975] closed the problem by invoking a set of unspecified eddy processes to bring the equatorward angular momentum transport. The horizontal mixing vorticity, the horizontal molecular viscosity or the large-scale barotropically unstable eddies were proposed as other candidates for the depleting angular momentum.

The other scenario was shown in Figure 1.12B. In this case, the meridional circulation extracts angular momentum from the surface level and transporting it upwards and polewards. And other plausible candidates causing up-gradient in the vertical direction are suggested such as solar-locked thermal tides, Kelvin-like modes or other inertia-gravity waves on a planetary scale, and small-scale internal gravity waves. Thermal tides are excited in the cloud layer and propagate both upward and downward and transport angular momentum vertically to accelerate the cloud-level atmosphere westward (e.g., Fels and Lindzen [1974]; Newman and Leovy [1992]; Takagi and Matsuda [2006, 2007]).Kelvin wave or other planetary-scale waves might be excited in the lower atmosphere and propagate upward to reach the cloud level, and transport angular momentum to accelerate the cloud-level atmosphere (e.g., Del Genio and Rossow [1990]; Imamura [2006]; Kouyama et al. [2015]; Peralta et al. [2015]; Yamamoto and Tanaka [1997]).They can contribute to the effective vertical transport of angular momentum, and it should be noted that the acceleration or deceleration of zonal flow can occur in the levels where these waves are generated or dissipated. In the case of the Earth, these waves act in a somewhat same manner to propagate upper ward from the troposphere and driving the Quasi-Biennial Oscillation in the equatorial stratosphere as described in Section 1.6 (or c.f. Baldwin et al. [2001]). At present, there is no particular mechanism allowing to construct the adequately self-consistent model and to reproduce the observed property of super-rotation. Additionally, the lack of observational evidence to evaluate the proposed models is a critical issue for understanding this phenomenon.

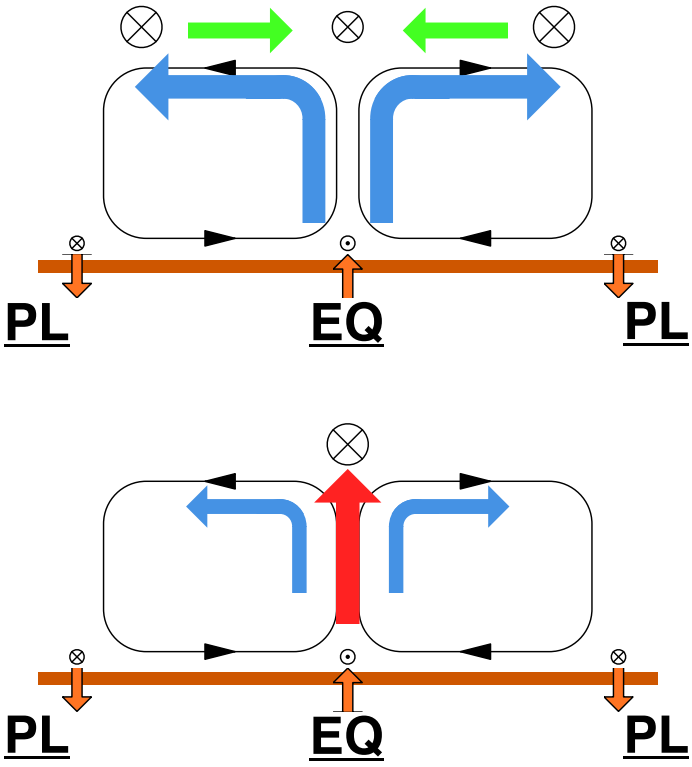

Figure 1.12: Schematic diagram of the super-rotation mechanism based on the review paper Sánchez-Lavega et al. [2017]. Upper: the classical "Gierach-Rossow-Williams" scenario, lower: an alternative scenario in which up-gradient fluxes of angular momentum occur predominantly in the vertical. EQ and PL denote the equatorial and polar region. The circle with cross or dot means the zonal jet of in prograde and retrograde direction respectively.

1.5 Planetary-scale waves on Venus

Planetary-scale waves are one of an important clue for understanding the eddy angular momentum transport. Furthermore, as explained in the following sentence, the transient behavior of these waves could allow us to access the observed variability in the winds or UV features. Fluctuations in winds velocity provide direct information of waves and eddies, and wave-like features can also be detected indirectly by the migration of planetary-scale UV brightness pattern. While there is an ambiguity interpreting observed variation regarding the meteorological quantities, the brightness data has an advantage for the usability and comprehensiveness of long-term continuous data compared to the cloud-tracked winds variation.

The first investigation of the transient behavior of the planetary-scale waves on Venus was conducted through the eight years monitoring of the Venus UV features by Pioneer Venus/OCPP. OCPP images were acquired during the long apoapsis portion of the elliptical orbit, and a maximum of four full-disk images could be obtained on a single 24-h orbit. OCPP images cover both northern and southern hemispheres, but usable images can exist no longer than about three months. Del Genio and Rossow [1990] conducted Fourier analysis for the time series of longitudinal mean normalized image brightness and investigated the propagation characteristics for longitudinal wavenumber 1 from spring 1979 to summer 1986. Figure 1.13 shows the result of Fourier analysis as a function of latitude for each observational period. The propagation of planetary scale UV features caused the periodical variation of UV brightness mostly with the period 4 or 5 days especially confirmed prominently in spring 1979, spring 1980 and spring 1982. In spring 1979, the equatorial region had 4-day circulation, and mid-latitudinal areas in both hemispheres had 5-days. After that, the periodicity had changed independently for equatorial and mid-latitudinal areas. In fall 1979, slightly shorter period than 4-day was confirmed. As demonstrated in the result of spring 1983 and spring1985, the periodicity was not always clear comparing to the early observation epoch. In the paper, 4-day and 5-day waves were identified as Kelvin wave and Rossby(-Haurwitz) wave (see Appendix A).

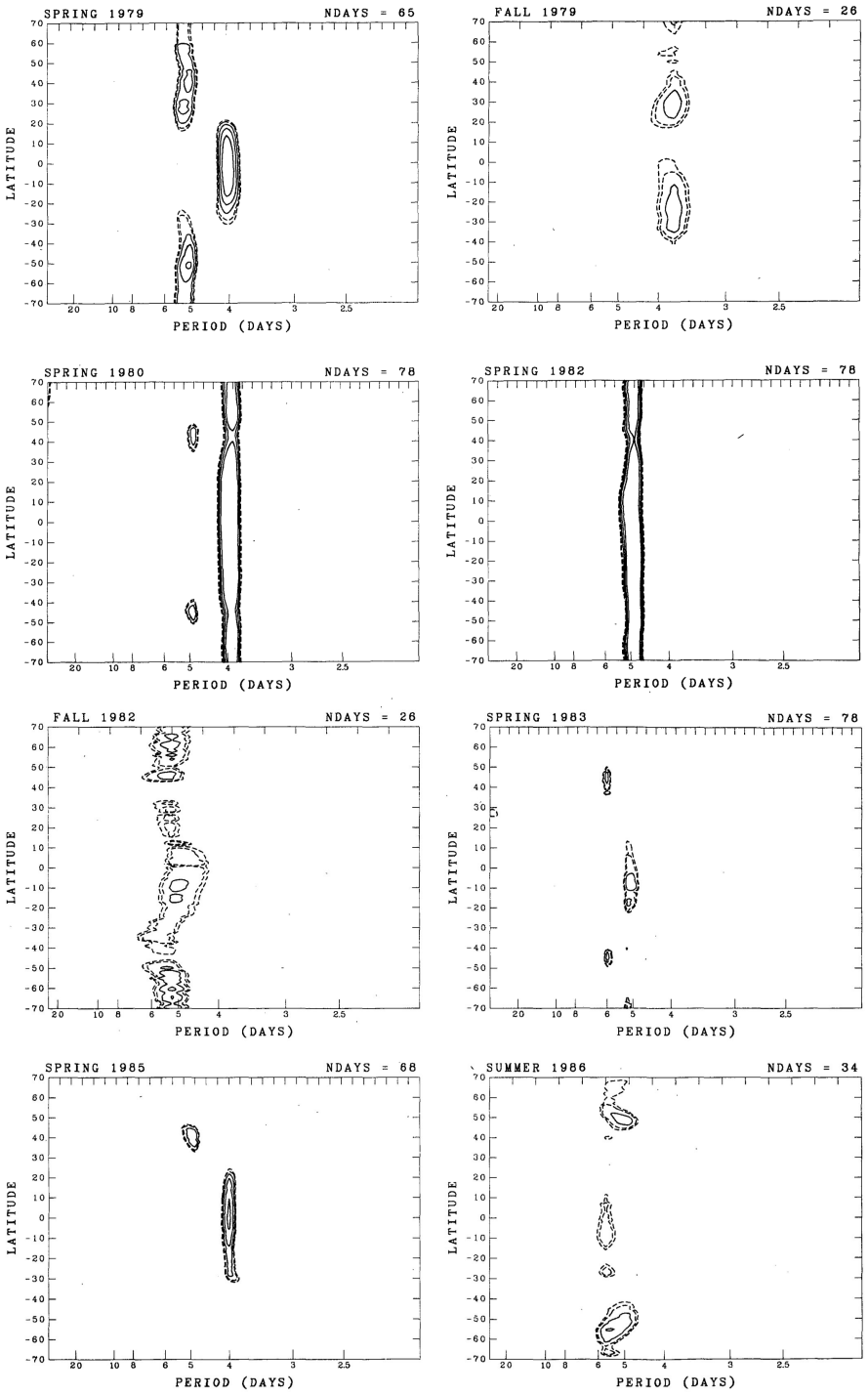

Figure 1.13: Pioneer Venus observe the periodicity of UV brightness variation and found the change of its period. Del Genio and Rossow [1990]

Del Genio and Rossow [1990] further investigated the transient of waves, and they suggested that the period of brightness variation corresponds to the propagation of the planetary-scale wave. They compared the corresponding rotation period of

brightness variation and that of mean zonal flow which derived from cloud-tracked velocity in the equatorial region. It can be confirmed that the propagation velocity of the equatorial planetary-scale waves is correlated with the wind speeds at the cloud level (Figure 1.14). They argued that the cloud level atmosphere vacillates between two distinct dynamical states on a time scale of perhaps 5–10 years. One suggested configuration is that planetary-scale equatorial wave became active and equatorial zonal winds are maximum from 1979 to 1980. Over the 2–3 year interval, this gives way to an alternative configuration in which equatorial waves are weaker, absent or different in character and equatorial zonal winds are weaker. Then, the first configuration returned over the same interval.

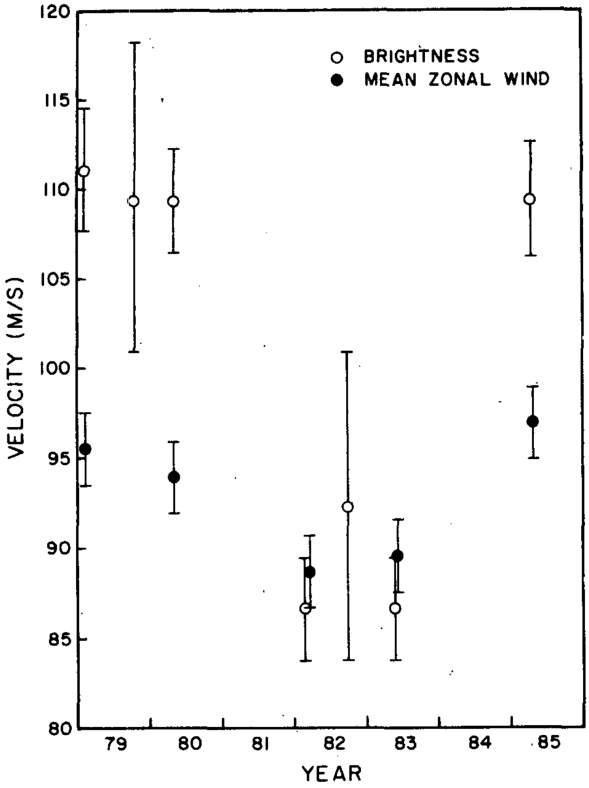

Figure 1.14: Mean equatorial cloud-tracked zonal wind speeds and propagation phase speeds implied by UV brightness periodicity. 5–10 years fluctuation seems to exist. Del Genio and Rossow [1990]

After the PVO mission period, these transient behaviors of the waves had been studied through the measurements of zonal mean wind velocity using the cloud-tracking method deduced from the Venus Express spacecraft. Kouyama et al. [2015] found that the Kelvin and Rossby waves alternately dominated from 2006 to 2010.

Figure 1.15. They investigated the observed appearance and disappearance of the waves could be explained by the filtering effect of background zonal wind velocity as the that Kelvin waves can reach the cloud top height when the background wind speed is slow, whereas Rossby waves can reach the cloud top when the wind speed is fast.

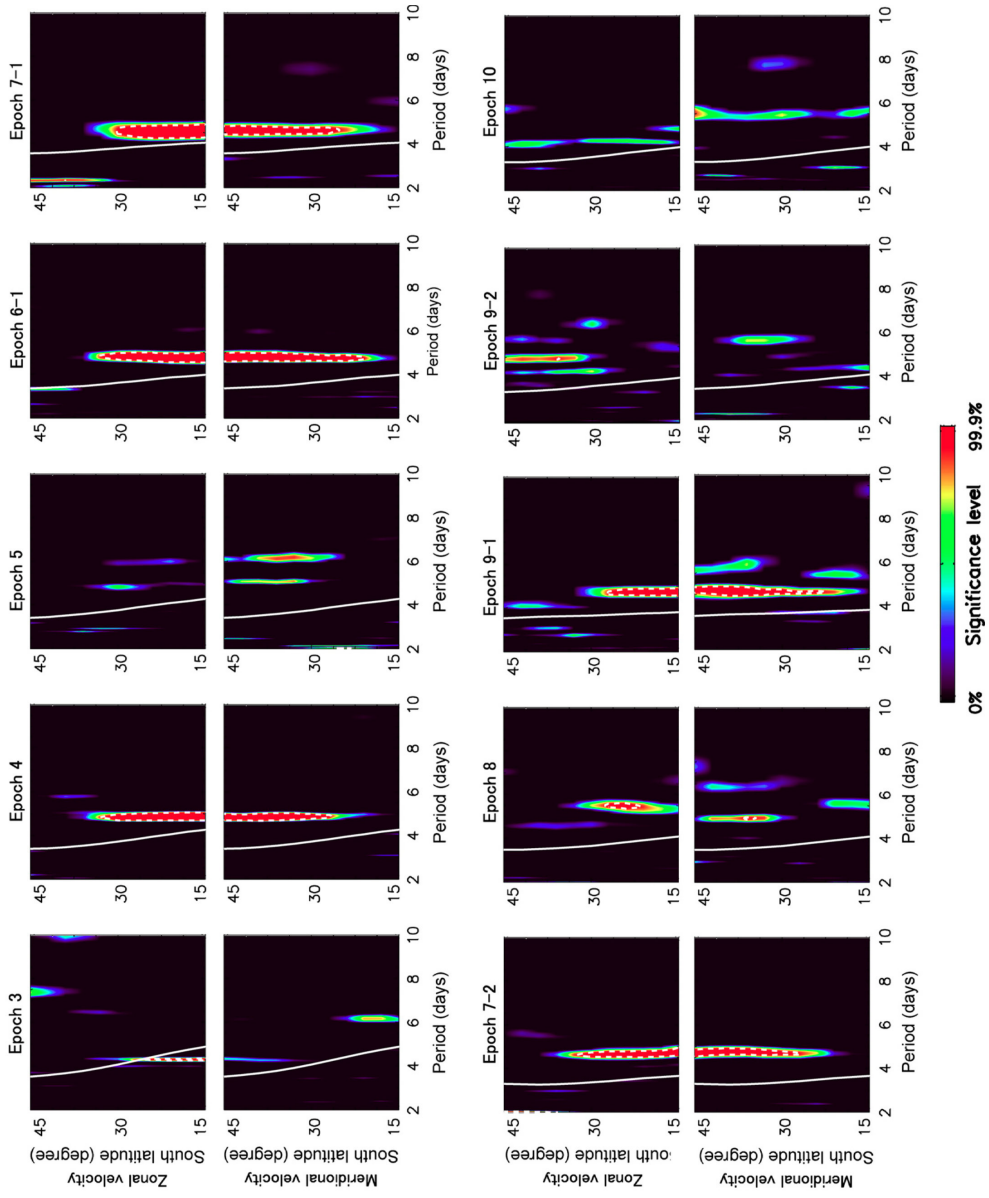

Figure 1.15: Time series power spectra of the zonal and meridional cloud-tracked velocities as functions of period and latitude. Colors represent statistical significance levels, and dotted contours indicate 90% significance level. The periods corresponding to the dayside-average zonal velocities are also plotted (solid curve) Kouyama et al. [2015]. The periodicity was changed in each observation epoch.

Planetary-scale waves can be related to the cloud top planetary-scale UV features, which could determine the global absorption efficiency of the solar radiation and be important for the energetic balance in the atmosphere. They also have an essential role for the super-rotation as a transporter of the angular momentum from the lower level. Therefore, the transient behavior of planetary-scale waves could alter the dynamical state of the atmosphere and could be related to the other meteorological phenomenon on Venus. However, since the observational work for studying planetary-scale waves on Venus were quite limited, and large gaps exist between the observational periods in previous observations, it has never investigated the variability within each observational period, and transient events occur within a time-scale of the sub-Venusian year was not considered.

Although the observations of the planetary-scale waves were not sufficient to reveal their general properties, several studies investigated the atmospheric dynamics of Venus based on their numerical models (e.g., Lebonnois et al. [2016]; Sugimoto et al. [2014]). Their recent model succeeded to reproduce fast super-rotating zonal wind of 100–120 m/s and Rossby waves can be confirmed developed from such as baroclinic waves. However, as described in Sugimoto et al. [2014] there is a disagreement between these modes and observations such as Kelvin wave cannot be found at the cloud top level in their numerical study, and is still challenging to reconstruct and explain the mechanism of the transient of planetary-scale waves.

1.6 Contribution of planetary-scale waves to the climate of the Earth

The planetary atmospheres commonly support a wide range of different waves and eddies. These waves and eddies could contribute to the transport of momentum, energy, and tracers. Planetary-scale wave is one of the important waves on planets and having a significant role in developing and maintaining the global circulation and climate. QBO (quasi-biennial oscillation) of stratospheric zonal winds on the Earth is the representative phenomenon being relevant to planetary-scale waves. Figure 1.16 shows the changes in the direction of winds from easterly to westerly and back with an observed average period of about 28 months. Periods of one year or harmonics of it are observable in many atmospheric quantities. However, the period of 28 months had been unexplained over decades.

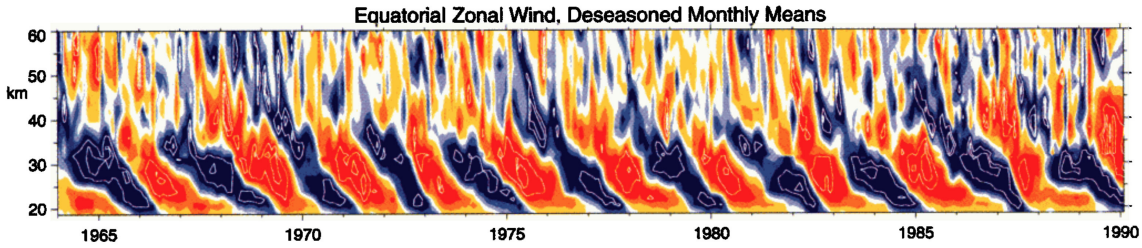

Figure 1.16: Time-height section of the monthly-mean zonal wind component (m/s), with the seasonal cycle removed for 1964–1990 observed by radiosonde and rocketsonde. The contour interval is 6 m/s, with bands between -3 and +3 unshaded. Red represents positive (westerly) winds. Baldwin et al. [2001]]

Generally speaking, revealing and understanding of this kind of meteorological phenomena requires a large amount of and continuous observation. In the case of the QBO, we had to wait for the regular balloon sounding in the 1950s for discovering and advancing our understanding of the alternation of prevailing easterly and westerly winds. Based on the observations, it has been suggested that vertically propagating equatorial waves had to be involved in the transport of zonal momentum. The developed conceptual models explained the QBO with wave-mean-flow interactions resulting from a combination of eastward and westward traveling waves, and some recent theories were constructed with the equatorial planetary-scale waves (Kelvin and mixed Rossby-gravity waves).

1.7 Limitation of the observations of UV features on Venus

Since the UV features are only visible on the dayside of Venus, the cloud top winds measured by mesoscale cloud tracking and the Y-feature observed with UV wavelength cannot be studied when the satellite apocenter is located on the night side of the revolving planet (e.g., Khatuntsev et al. [2013]). In the case of PVO data, images can be used no longer than about three months. And for Venus Express data, usable images were mainly constrained to southern hemisphere because the spacecraft was in the elliptical quasi-polar orbit, with its apocenter in the southern hemisphere, precluding a global-scale investigation of the Y-feature. Therefore, it has long been difficult for conducting continuous dayside observations and for investigating the variability of the Venusian atmosphere. Table 1.7, and 1.7 summarize the observation length and interval for the two study of Del Genio and Rossow [1990] and Kouyama et al. [2015]. The maximum continuous observation days is approximately < 3 month, and there are intervals of several months. As a result, the periodicity variations on sub-yearly timescales (one Venusian year is $\sim$224 Earth days) were obscured by the limitations of continuous dayside observations.

Table 1.2: Days information of observation lengths and intervals of Pioneer Venus Del Genio and Rossow [1990].

Imaging epoch	Days of year	Length [days] (Days of missing)
Spring, 1979	7–72	66 (0)
interval	= 212 days	
Fall, 1979	283–309	27 (8)
interval	= 146 days	
Spring, 1980	88–166	79 (0)
interval	= 603 days	
Spring, 1982	35–113	79 (0)
interval	= 146 days	
Fall, 1982	258–284	27 (6)
interval	= 204 days	
Spring, 1983	121-199	79 (12)
interval	= 608 days	
Spring, 1985	73–141	69 (13)
interval	= 451 days	
Summer, 1986	195–229	35 (13)

Table 1.3: Days information of observation lengths and intervals of Venus Express Kouyama et al. [2015]

Orbit no.	Length [days]
30–74	44
interval	= 134 days
208–298	90
interval	= 138 days
436–515	79
interval	= 133 days
648–741	93
interval	= 128 days
869–940	71
interval	= 142 days
1082–1133	51
interval	= 38 days
1171–1189	18
interval	= 131 days
1320–1347	27
interval	= 27 days
1374–1420	46
interval	= 169 days
1589–1638	49
interval	= 132 days
1770–1812	42
interval	= 2 days
1814–1856	42
interval	= 175 days
2031–2080	49

Additionally, because of the less continuity of the observation data or small temporal coverage of the time series dataset, it has never studied how the planetary-scale waves appeared and disappeared on Venus cloud top. In another word, there is no observational information on the continuous behavior during the "wave switching."

Figure 1.17 shows the current understanding of planetary-scale waves on Venus cloud top mainly based on the result from Del Genio and Rossow [1990]. The illustration clearly shows the large data gap between each observation epoch and also, the continuous existence of waves were not studied in detail.

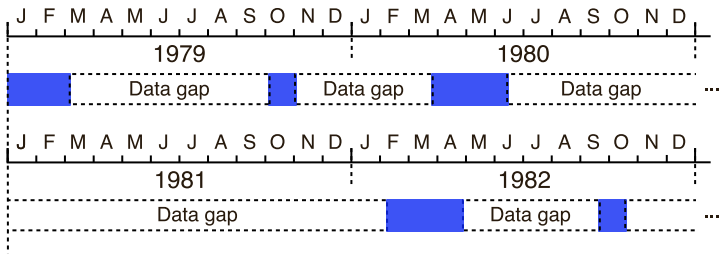

Figure 1.17: Coverage of the previous space-based observation by Pioneer Venus Del Genio and Rossow [1990]. Large gaps between the observational periods are due to the orbit nearly fixed inertial frame of reference, and that observation limitation could occur in other mission to Venus.

In the actual conditions with a limited number of desirable Venus explorations, it is clear that only the spacecraft based observation could not easily break through the current observation limit. On the other hand, ground-based observations have a potential to contribute to monitoring Venus. For example, planetary-scale UV feature (such as Y-feature) could be observed. As the Venus–Earth synodic period is 584 days, Venus can be almost continuously observed over one Venusian year (except for the conjunction seasons). In the left side of Figure 1.17, the expected scale of the opportunity of Venus ground-based observation is displayed. This figure shows, ground-based observations could complement the spacecraft observations for elucidating annual phenomena on Venus. From the Earth, observations of Venus are complicated by several factors, such as the changing phase angle (which alters the dayside area of Venus), the short nighttime observation period (the direction to Venus approximates that to the Sun), weather conditions, and the Earth ' s atmospheric extinction. However, ground-based observations have sufficient spatial resolution to observe the planetary-scale features in both hemispheres (e.g., Dollfus [1975] and also allow continuous observations, as mentioned above. Currently, since the occupation of telescopes for the single scientific target has many difficulties, the large problem for realizing the long-term and continuous observation is that only a few telescopes are available in the world.

Since the first photographic detection of the UV features on Venus was done in 1911 in France by Quénisset, (1921), there were many attempts for monitoring the UV features on Venus (see, e.g., Table 2 of Dollfus [1975]). A great effort to improve time coverage in monitoring Venusian UV feature was made by combining observatories from several sites in the world under the offer from International Astronomical Union. However, it has never well established for investigating the pe-

riodical properties of the rotation of UV features in the prime era of ground-based Venus observation, and increasingly, the mainstream of Venus observations moved into spacecraft based.

1.8 Purpose of this study

It is clear that atmospheric waves and its propagation have a very important role not only for shaking the atmosphere but also contributing to the entire climate on the planet. Traveling waves transport the energy and momentum and release them when they break. The transported momentum is considered having an effect on the jet in the middle atmosphere and troposphere, the balance of global structure of temperature, pressure, and winds on the Earth as described in Section 1.6. In the case of Venus, planetary-scale waves can determine the global pattern of UV feature at the cloud top, which should be crucial for the absorption of solar radiation in the cloud layer. Additionally, it is suggested that the vertical momentum transport of planetary-scale waves is one of the important clues for maintaining the fast zonal flow of the super-rotation. However, the understanding of planetary-scale waves on Venus is still poor, and the previous space-based observations covered limited time range as shown in Section 1.7.

The first purpose of this study is observing the appearance and transit behavior of planetary-scale waves on Venus for a longer time. It has never conducted, but ground-based observation could have great potential to conduct long-term Venus observation (see Figure 1.1 or Section 2.2). Therefore, this study attempts to establish the methodology of planetary-scale waves observation from the ground, evaluate the consistency of ground-based with space-based data, and obtain the long-term continuous data.

The second purpose of this study is revealing the basic characteristics of the planetary-scale waves in the Venus at the cloud top layer. For example, answering the following questions – which waves are more widely observed? – how is the lifetime of each wave? –how to wave transient occur (does filtering the of vertical wave propagation by zonal mean-wind velocity? (suggested by Kouyama et al. [2015]) works) are the motivation of this study. Especially, observing the time continuous behavior of the appearance and disappearance of the waves is the main objective. These characteristics could help us investigating the climate of our twin planet, and also direct to

understanding the mechanism of the Super-rotation.

To achieve above purposes, we investigated the propagation period of the planetary-scale UV feature at the cloud tops over one Venusian year using ground-based telescopes and AKATSUKI spacecraft. From the high spatial resolved UV images obtained by AKATSUKI/UVI, the fluctuation period and the mean of zonal cloud-tracked wind velocity also analyzed to investigate the propagated planetary-scale waves in fast zonal winds. Chapter 2 of this paper describes the long-term ground-based observations and the methodology of analyzing images. Chapter 3 describes the detail of observations and the analysis procedure of the AKATSUKI/UVI obtained images. The analytical method of the periodicity changes in continuous long-term data and observed periodicity of the variation in UV brightness and zonal winds velocity are presented in Chapter 4. Chapter 5 discusses the implications of the periodicity variation as the manifestation of planetary-scale waves. The observed results of the time continuous behavior of the appearance and disappearance of planetary-scale waves are interpreted with the characteristics of the vertical propagation of waves. The study is summarized in Chapter 6.

2 Observation and data analysis of Ground-based images

Since Venus is an inner plant, there are some difficulties to observe Venus from the Earth. However, ground-based observations have a great advantage for keep monitoring the same local time region. In previous, planetary-scale waves on Venus has never monitored from the Earth. In this section, the developed methodology realizing the Venus long-term continuous observation. In Section 2.1, used telescopes and instruments are shown and the detail information of obtained data are described in Section 2.2. Image reduction and analysis method are included in Section 2.3, and further analysis for measuring the relative brightness variation, which was to used retrieving the period of planetary-scale waves are described in Section 2.4.

2.1 Telescopes and instruments

Our ground-based observations were conducted with the multi-spectral imager (MSI; Figure 2.1 Left) Watanabe et al. [2012] mounted on the Pirka telescope (Figure 2.1 Right) at Nayoro in Hokkaido, Japan, where the city is in the center of the basin, and the observatory is located at 142.5° E longitude and latitude 44.4° N at 151 m above sea-level. The 1.6-m Pirka telescope, operated by the Faculty of Science of the Hokkaido University, is primarily dedicated to observations of the planets of the Solar System. Using this telescope, we can continuously monitor Venus over several months. The MSI has a 512 × 512 pixel electron-multiplying charge-coupled device (EMCCD) camera with a pixel scale of 0.388 arcsec (the field of view is 3.3 × 3.3 arcmins). In this study, we used the MSI with the normal CCD mode, and 0.035 s can be used as the minimum exposure time at the selected observation mode by employing a partial (sub-array 512 × 128 pixel) readout.

The observation site is usually favored by fine weather in daytime (the success rate is over 70% without winter season), and it is, thus suitable for ground-based observations of Venus. The natural seeing size (FWHM in R-band) at the observatory is 1.3–2.3 arcsec (typically 1.8 arcsec in median), which is enough to observe planetary-scale UV features ($\geq$ 10,000 km) on Venus. The observational requirement is then determined that the angular diameter of Venus is bigger than about 15 arcsec to distinguish 10° latitudinal bands. While there is a lot of snow in the winter season, there is no rainy season in June, which is common in other islands of Japan. Ttherefore we can have a good ratio of fine weather. The detail of the specifications of Pirka telescope and MSI is listed in Table 2.1 and 2.2.

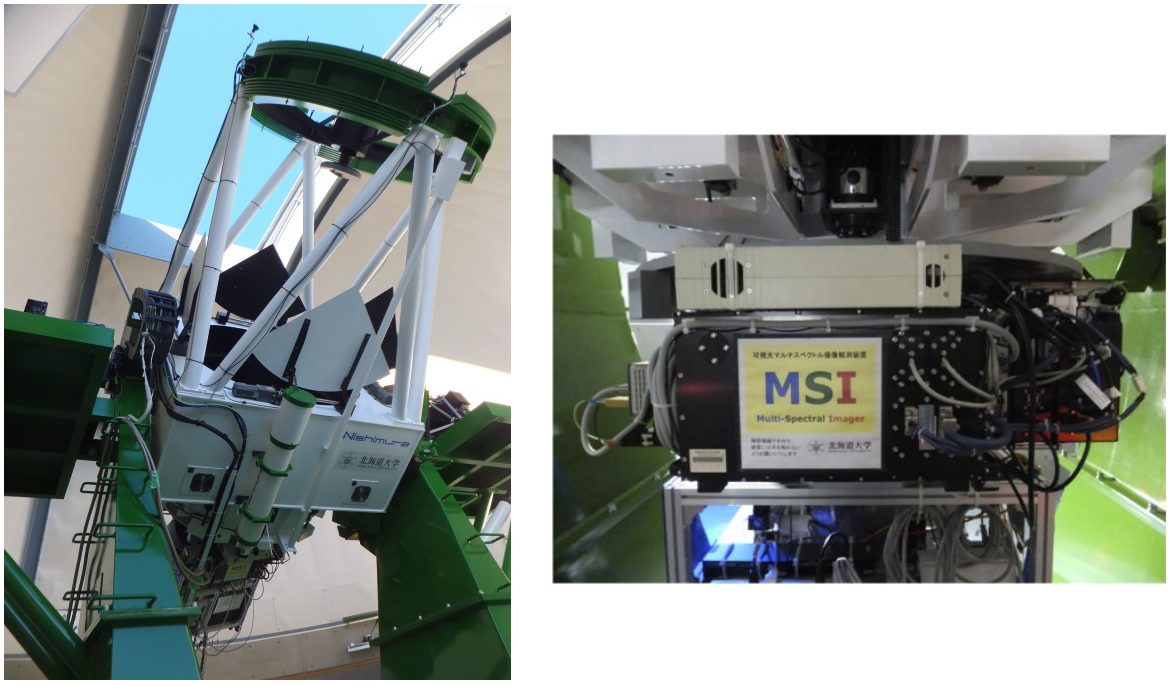

Figure 2.1: Pictures of 1.6-m Pirka telescope(left) and MSI(right). The left figure was taken during the Venus observation in the daytime. MSI is mounted at the Cassegrain focus where the bottom part of the primary mirror cell in the left figure.

Additionally, the cooperative observation was conducted from June to August 2017, using the imaging mode of the high-speed spectrometer (HSCAM) installed on 1.5-m Kanata telescope at Higashi-Hiroshima in Hiroshima, Japan (Figure 2.2). Hiroshima is well distant from Hokkaido, and the weather is independent. Since there is a risk

[†1]Some alternative narrow-band filters are installed currently.

Table 2.1: The major specifications of the Pirka telescope.

Location coordinate	44°22′ N 142°28′ E
Height of observatory	151 m
Optical system design	Ritchey-Chretien
Primary mirror	
- Effective aperture	1600 mm
- Principal focal length	19237.7 mm (F/12.0)
Focal length	
Cassegrain FOV	3 arcmin
Nasmyth A FOV	10 arcmin
Nasmyth B FOV	20 arcmin
Manufacturer	Nishimura Co., Ltd

Table 2.2: The major specifications of the Multi Spectral Imager.

Spectral coverage	360–1050 nm
Field of view	151 m
- Resolution	3.3′ × 3.3′ (0.389″/pixel)
Filters	
- Liquid crystal tunable filters	CRi VariSpec VIS-10: 400–720 nm, $\Delta\lambda$ ∼10 nm (@ 650 nm)
	CRi VariSpec SNIR-10: 650–1100 nm, $\Delta\lambda$ ∼10 nm (@ 900 nm)
- Narrow-band filters[†1]	360, 365, 370, 380, 390 nm ($\Delta\lambda$ = 10 nm), H α ($\Delta\lambda$ = 1 nm)
- Broad-band filters	Johnson-Cousins U ,B, V, R, I
Camera (CCD)	Hamamatsu Photonics C9100-13
Array format	512 × 512 pixel (Pixel size: 16 × 16 µm)
Readout modes	EMCCD mode, Normal CCD mode
Pixel clock rates	11 MHz (EMCCD mode only), 0.69 MHz, 2,75 MHz
Maximum frame rates (full-frame)	31.9 frames/s (EMCCD mode), 2 frames/s (Normal CCD mode)
Minimum exposure times (full-frame)	0.031 s (EMCCD mode), 0.488 s (Normal CCD mode)
EM gain	4 - 1200
CCD cooling method & temperature	Peltier with forced-air, -65°C

of long spells of bad weather, this cooperative observation could help to avoid large data missing. The HSCAM has 512 × 512 pixel format of CCD with 0.26″ of pixel size and 2.3′ × 2.3′ of FOV. The available exposure time ranges from 27.1 msec 10 sec, and major specifications of the instrument and telescope are satisfied the requirement of our observation. (The detail can be seen in, e.g., `http://www.kwasan.kyoto-u.ac.jp/~nogami/HSspec/`).

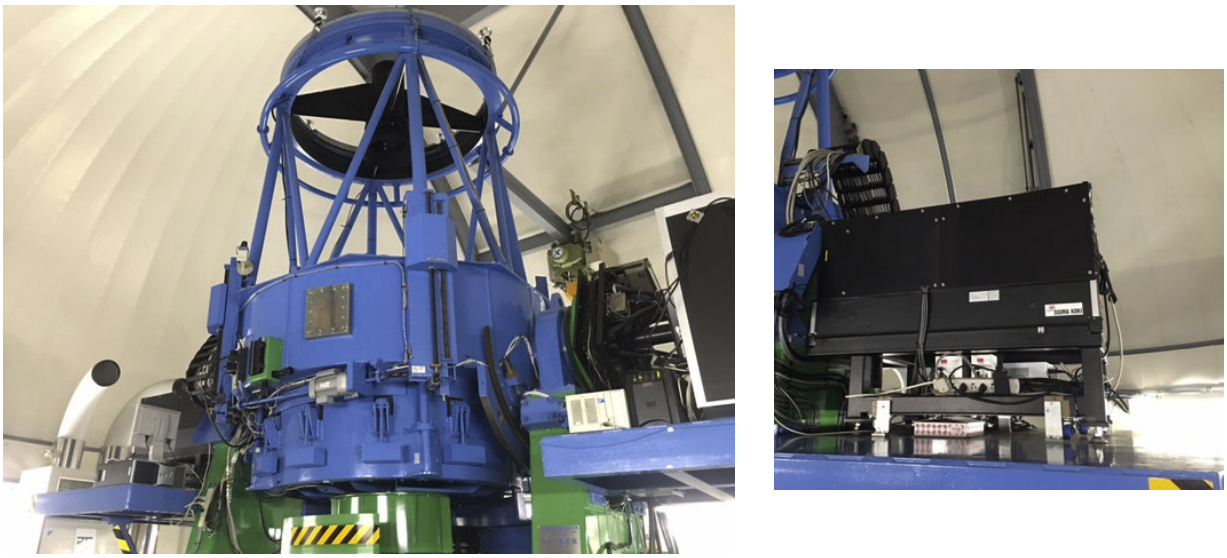

Figure 2.2: Pictures of 1.5-m Kanata telescope and HSCAM.

2.2 Observations and data

Since the seeing at a low elevation is worse, most of the Venus images were taken during the daytime, although it contains high background noise. The altitudes of Venus ranged from 20° to 65° during the observation time, and were typically ∼45° in the daytime. 20 sky images were taken for making flat frame (daylight flat) and after the observation, and bias frames (10 images for one set) were taken adequately during the whole observation time. Photometric standard stars were not observed with because the main observation time is in the daytime. Maximum observation times were about 4 hours in a day and took at least 200 images. Imaging size is modified to $512pix \times 128pix$ enabling the fast read out. We adopt dithering method when we take Venus images in order to include the uncertainty of flat fielding into

the variance of the data as the observational error.

The cloud top features are better contrasted at 365 nm in the near-UV range, and the day-to-day variation is up to 40% Lee et al. [2015]. We used narrow-band filters with a center wavelength of 365 nm (± 2nm) and FWHM of 10nm (± 2 nm) and FWHM of 20 nm (± 2 nm). The later filter was installed in March 2017 to improve the transmittance, and the difference in the FWHM can be neglect because of the broad absorption band as shown in Figure 1.7. This center wavelength is the same as those used by on the OCPP/Pioneer Venus and VMC/Venus Express.

The brightness variations due to the UV contrast on Venus disc were expected to be larger than the sky background noise observed even in daytime. To measure brightness variations exceeding 10%, we selected Venus images with signal-to-noise (S/N) ratios is more than 10 in the 60° latitudinal band. Since the major sources of total ADU (Analog-Digital Unit) counts are the light from Venus (∼10,000 ADUs) and the sky background (∼20,000 ADUs). The readout noise the CCD at the observation mode is ∼30. Here, we assumed that the noise can be properly described with the Poisson statistics, and the S/N ratio in the 60° latitudinal band can be expressed as

$$\mathrm{S/N} = \mathrm{GC_{max}}/\sqrt{\mathrm{G}(\mathrm{C_{max}}\cos 60^\circ + \mathrm{C_{sky}})}, \tag{2.1}$$

where $\mathrm{C_{max}}$ is the maximum counts in each raw image, $\mathrm{C_{sky}}$ is the mean counts of the sky background and G represents the gain of the EMCCD (1.4 e-/ADU). The sky background was estimated from the pixels in the annulus region, whose inner and outer radii are equal to twice and four times radius of Venus, respectively. Additionally, we selected images, whose the standard deviation in the sky background area was smaller than the square root of the mean sky background, to remove images affected by partly cloudy weather. The exposure time (0.035–0.1 s) was preferably adjusted so that $\mathrm{C_{max}}$ = 30,000–35,000, ensuring > 99.5% linearity of the MSI ' s EM-CCD. Since longer exposed image is suffered larger blurring (seeing) effect, the typical exposure time was 0.035 s.

Our ground-based observations were conducted from April to July 2015 and January to September 2017. Since the inferior conjunction of Venus occurred on March 25, 2017, and we have snow season from November to March at the observation site, the data were separated into three observational periods as labeled OP2015 (21/04/2015–17/07), OP2017A (03/01/2017–19/02), and OP2017B (23/04/2017–

10/09). The data acquisition rates were 65/84 (77%), 27/45 (60%), (90/141 (61%) respectively as shown in Figure 2.3–2.5. Sun–Venus–Observer angles were 64.8°–126°, 83.4°–119°, and 142°–43.9°, and angular diameter were 15.6″–44.6″, 22.1″–40.1″, and 43.1″–12.0″ respectively. Figure 2.6 shows the plots of the angular diameter of Venus and Sun–Venus–Earth elongation angle from 2015 to 2017, and yellow colored box corresponds to each observation period. As shown in Figure 2.7, Venus angular diameter and phase angle gradually change. Our observational requirements are that Venus diameter should be larger than ∼14″ to resolve 10° latitudinal bands for capturing planetary-scale features and the phase angle larger lower than 120° to ensure the same local time region is visible. Blue and red horizontal dashed lines indicates the lower limit of Venus diameter and the upper limit of elongation angle respectively defining our opportunity of Venus observation.

OP2015

01-Apr-15		01-May-15	P	01-Jun-15	P	01-Jul-15	
02-Apr-15		02-May-15	P	02-Jun-15	P	02-Jul-15	P
03-Apr-15		03-May-15	P	03-Jun-15		03-Jul-15	P
04-Apr-15		04-May-15		04-Jun-15		04-Jul-15	P
05-Apr-15		05-May-15	P	05-Jun-15	P	05-Jul-15	P
06-Apr-15		06-May-15	P	06-Jun-15	P	06-Jul-15	P
07-Apr-15		07-May-15	P	07-Jun-15		07-Jul-15	P
08-Apr-15		08-May-15		08-Jun-15	P	08-Jul-15	P
09-Apr-15		09-May-15	P	09-Jun-15		09-Jul-15	P
10-Apr-15		10-May-15	P	10-Jun-15		10-Jul-15	P
11-Apr-15		11-May-15	P	11-Jun-15	P	11-Jul-15	P
12-Apr-15		12-May-15		12-Jun-15	P	12-Jul-15	P
13-Apr-15		13-May-15	P	13-Jun-15		13-Jul-15	
14-Apr-15		14-May-15	P	14-Jun-15	P	14-Jul-15	P
15-Apr-15		15-May-15	P	15-Jun-15	P	15-Jul-15	
16-Apr-15		16-May-15	P	16-Jun-15	P	16-Jul-15	P
17-Apr-15		17-May-15	P	17-Jun-15	P	17-Jul-15	P
18-Apr-15		18-May-15	P	18-Jun-15	P	18-Jul-15	
19-Apr-15		19-May-15		19-Jun-15	P	19-Jul-15	
20-Apr-15		20-May-15	P	20-Jun-15	P	20-Jul-15	
21-Apr-15	P	21-May-15	P	21-Jun-15	P	21-Jul-15	
22-Apr-15	P	22-May-15	P	22-Jun-15		22-Jul-15	
23-Apr-15	P	23-May-15	P	23-Jun-15		23-Jul-15	
24-Apr-15	P	24-May-15	P	24-Jun-15	P	24-Jul-15	
25-Apr-15	P	25-May-15	P	25-Jun-15		25-Jul-15	
26-Apr-15	P	26-May-15		26-Jun-15	P	26-Jul-15	
27-Apr-15	P	27-May-15	P	27-Jun-15	P	27-Jul-15	
28-Apr-15	P	28-May-15	P	28-Jun-15		28-Jul-15	
29-Apr-15	P	29-May-15	P	29-Jun-15		29-Jul-15	
30-Apr-15	P	30-May-15	P	30-Jun-15		30-Jul-15	
		31-May-15	P			31-Jul-15	

Figure 2.3: Observation day and data acquisition status in OP2015. “P” denotes observations with Pirka telescope.

OP2017A

01-Jan-17		**01-Feb-17**	
02-Jan-17		**02-Feb-17**	P
03-Jan-17	P	**03-Feb-17**	P
04-Jan-17	P	**04-Feb-17**	P
05-Jan-17	P	**05-Feb-17**	P
06-Jan-17	P	**06-Feb-17**	
07-Jan-17		**07-Feb-17**	P
08-Jan-17	P	**08-Feb-17**	
09-Jan-17		**09-Feb-17**	P
10-Jan-17		**10-Feb-17**	P
11-Jan-17		**11-Feb-17**	
12-Jan-17		**12-Feb-17**	
13-Jan-17	P	**13-Feb-17**	
14-Jan-17	P	**14-Feb-17**	
15-Jan-17		**15-Feb-17**	P
16-Jan-17		**16-Feb-17**	
17-Jan-17		**17-Feb-17**	P
18-Jan-17	P	**18-Feb-17**	
19-Jan-17	P	**19-Feb-17**	P
20-Jan-17	P	20-Feb-17	
21-Jan-17	P	21-Feb-17	
22-Jan-17		22-Feb-17	
23-Jan-17	P	23-Feb-17	
24-Jan-17	P	24-Feb-17	
25-Jan-17	P	25-Feb-17	
26-Jan-17	P	26-Feb-17	
27-Jan-17		27-Feb-17	
28-Jan-17		28-Feb-17	
29-Jan-17			
30-Jan-17	P		
31-Jan-17	P		

Figure 2.4: Same figure as Fig. 2.3.

OP2017B

01-Apr-17		**01-May-17**	P	**01-Jun-17**		**01-Jul-17**		**01-Aug-17**	P, K	**01-Sep-17**	
02-Apr-17		**02-May-17**	P	**02-Jun-17**		**02-Jul-17**		**02-Aug-17**	P	**02-Sep-17**	
03-Apr-17		**03-May-17**	P	**03-Jun-17**		**03-Jul-17**		**03-Aug-17**	P, K	**03-Sep-17**	P
04-Apr-17		**04-May-17**	P	**04-Jun-17**	P	**04-Jul-17**		**04-Aug-17**	P	**04-Sep-17**	P
05-Apr-17		**05-May-17**	P	**05-Jun-17**	P	**05-Jul-17**		**05-Aug-17**	P	**05-Sep-17**	P
06-Apr-17		**06-May-17**	P	**06-Jun-17**		**06-Jul-17**		**06-Aug-17**	P	**06-Sep-17**	P
07-Apr-17		**07-May-17**		**07-Jun-17**		**07-Jul-17**	P	**07-Aug-17**	P, K	**07-Sep-17**	P
08-Apr-17		**08-May-17**	P	**08-Jun-17**	P	**08-Jul-17**	P	**08-Aug-17**	P	**08-Sep-17**	P
09-Apr-17		**09-May-17**	P	**09-Jun-17**		**09-Jul-17**		**09-Aug-17**	P	**09-Sep-17**	
10-Apr-17		**10-May-17**		**10-Jun-17**		**10-Jul-17**		**10-Aug-17**	P, K	**10-Sep-17**	P
11-Apr-17		**11-May-17**	P	**11-Jun-17**	P	**11-Jul-17**		**11-Aug-17**		11-Sep-17	
12-Apr-17		**12-May-17**	P	**12-Jun-17**	P, K	**12-Jul-17**	P	**12-Aug-17**		12-Sep-17	
13-Apr-17		**13-May-17**	P	**13-Jun-17**	K	**13-Jul-17**	P	**13-Aug-17**		13-Sep-17	
14-Apr-17		**14-May-17**		**14-Jun-17**	K	**14-Jul-17**	P	**14-Aug-17**		14-Sep-17	
15-Apr-17		**15-May-17**		**15-Jun-17**	K	**15-Jul-17**		**15-Aug-17**	P	15-Sep-17	
16-Apr-17		**16-May-17**		**16-Jun-17**	P	**16-Jul-17**		**16-Aug-17**	P	16-Sep-17	
17-Apr-17		**17-May-17**	P	**17-Jun-17**	P, K	**17-Jul-17**		**17-Aug-17**		17-Sep-17	
18-Apr-17		**18-May-17**	P	**18-Jun-17**	P	**18-Jul-17**		**18-Aug-17**	P	18-Sep-17	
19-Apr-17		**19-May-17**	P	**19-Jun-17**	P	**19-Jul-17**	K	**19-Aug-17**	P, K	19-Sep-17	
20-Apr-17		**20-May-17**		**20-Jun-17**	P	**20-Jul-17**	P	**20-Aug-17**	P, K	20-Sep-17	
21-Apr-17		**21-May-17**		**21-Jun-17**		**21-Jul-17**	P	**21-Aug-17**		21-Sep-17	
22-Apr-17		**22-May-17**		**22-Jun-17**	K	**22-Jul-17**	P	**22-Aug-17**		22-Sep-17	
23-Apr-17	P	**23-May-17**		**23-Jun-17**		**23-Jul-17**		**23-Aug-17**		23-Sep-17	
24-Apr-17	P	**24-May-17**		**24-Jun-17**		**24-Jul-17**	P	**24-Aug-17**	P	24-Sep-17	
25-Apr-17	P	**25-May-17**	P	**25-Jun-17**		**25-Jul-17**	P	**25-Aug-17**	P	25-Sep-17	
26-Apr-17	P	**26-May-17**		**26-Jun-17**	P	**26-Jul-17**	P, K	**26-Aug-17**	P, K	26-Sep-17	
27-Apr-17	P	**27-May-17**		**27-Jun-17**		**27-Jul-17**		**27-Aug-17**	K	27-Sep-17	
28-Apr-17		**28-May-17**	P	**28-Jun-17**		**28-Jul-17**	P	**28-Aug-17**		28-Sep-17	
29-Apr-17	P	**29-May-17**	P	**29-Jun-17**		**29-Jul-17**	P	**29-Aug-17**	P	29-Sep-17	
30-Apr-17		**30-May-17**		**30-Jun-17**		**30-Jul-17**	P	**30-Aug-17**	P	30-Sep-17	
		31-May-17				**31-Jul-17**	P, K	**31-Aug-17**	P, K		

Figure 2.5: Same figure as Fig. 2.3. "K" denotes observations with Kanata telescope.

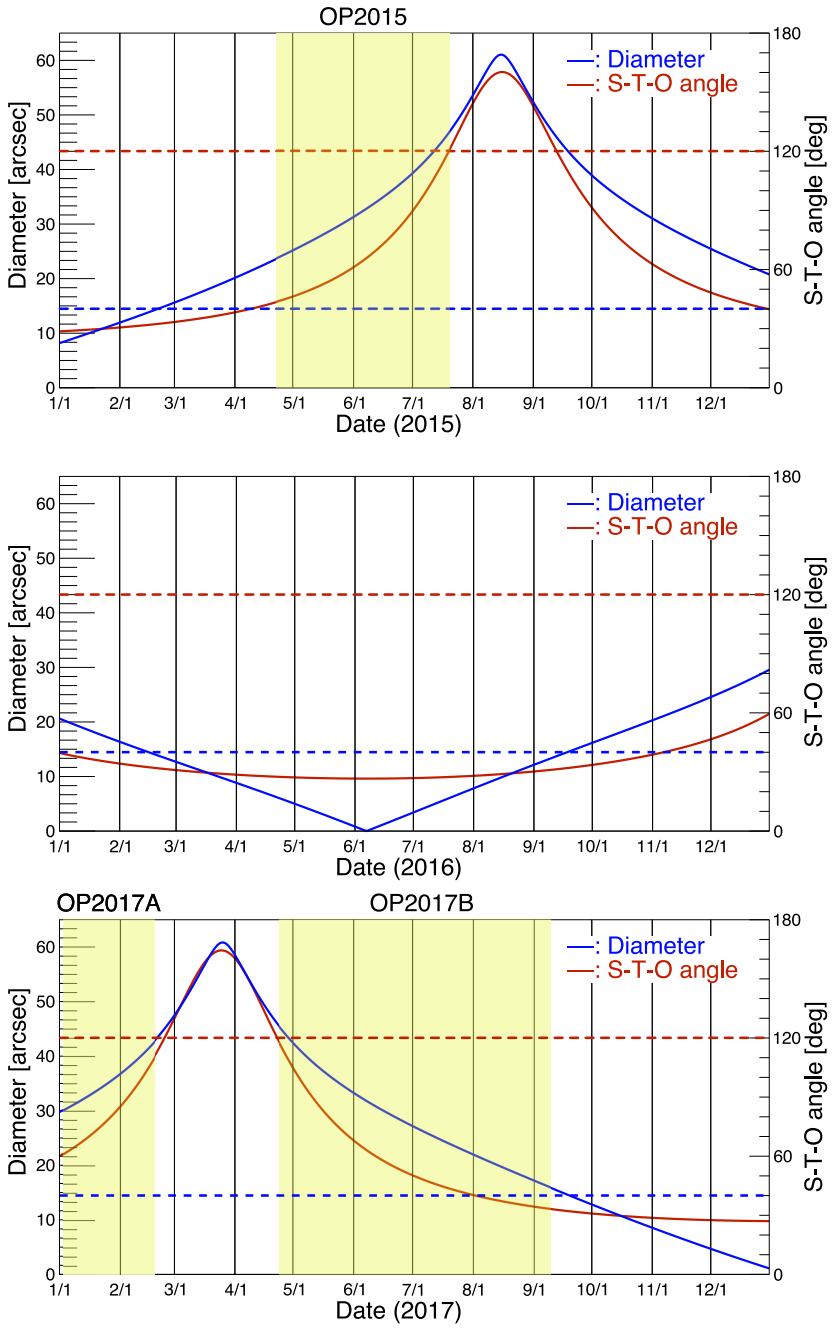

Figure 2.6: The angular diameter and phase angle are plotted from 2015 to 2017. Plotted data was obtained from JPL's HORIZONS system, and each point referred the information at 0:00 UT. The yellow hatched area corresponds to each observational period.

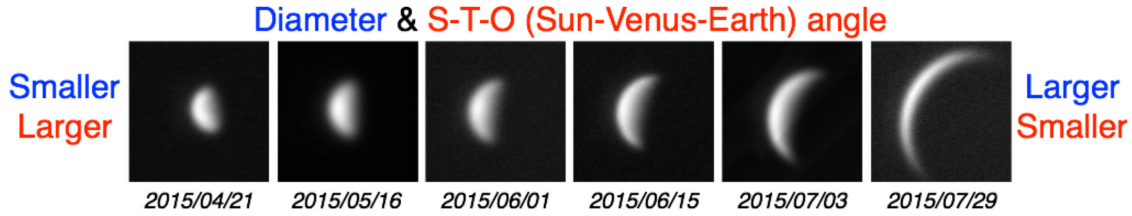

Figure 2.7: Venus images taken with MSI at 365 nm during OP2015. Venus diameter gradually becomes large, and dayside area decreases as Sun–Venus–Earth angle becomes small.

2.3 Image reduction and analysis

The all obtained images from Pirka and Kanata telescopes were proceeded and analyzed in the same way as described below. The idea of image reduction and analysis is already establish as published in Imai et al. [2016]. In this study, the UV brightness variation of Venus was measured at several latitudes and times. The basic image reductions included bias subtraction and flat-fielding (correction for pixel sensitivity variation). The data were reduced with IRAF and the MSI data reduction package (MSIRED), and sky flats were used for flat-fielding. The upper row of Figure 2.8 depicts samples of the reduced images at each observation period. Venus's rotational axis is aligned with the Y-axis (the up and right directions denote north and east, respectively). The image centers correspond to the center of Venus. The longitudes and latitudes on Venus were determined using simulated Venus images based on the Venus–Earth at the observation times, which was obtained from the JPL's HORIZONS system via the telnet interface (`telnet://horizons.jpl.nasa.gov:6775`). The geometric information were acquired every 1 minutes and Venus angular diameter, the target longitudes and latitudes (IAU2009 model) at the sub-observer (Earth) and sub-solar points, the north pole position angle (with respect to the direction of the true-of-date celestial north pole), and the one-way light-time from the target center to observer at the observation time were used for the calculation.

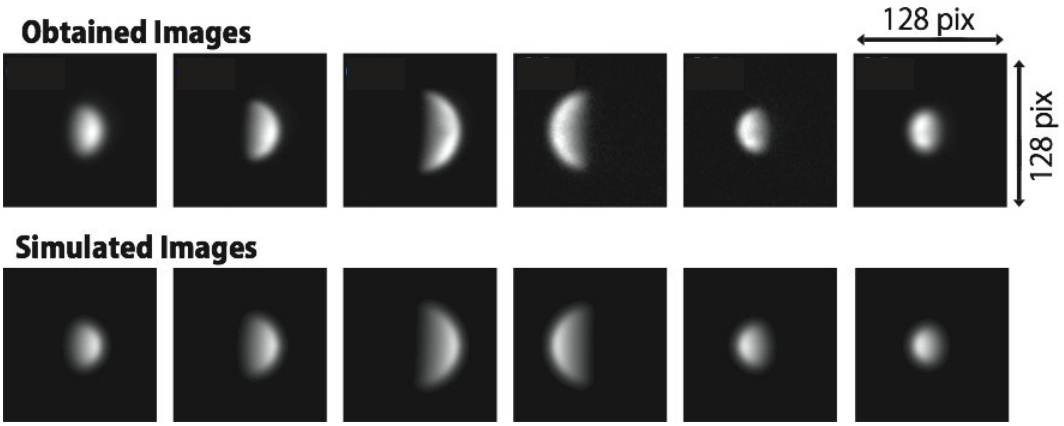

Figure 2.8: Samples of the obtained and simulated images of Venus. The upper images were taken with MSI and the Pirka telescope and were subjected to basic reductions. The observational days were (left to right) 2013/08/28, 2013/10/02, 2013/11/03, 2014/03/23, 2014/05/29, and 2014/06/24 (see Imai et al. [2016]).

Assuming a cloud top altitude of 70 km, the simulated images were calculated by using Belton's empirical function (BELTON et al. [1991]),

$$I(x,y) = \frac{1}{\pi\mu(x,y)}\Big\{\mu(x,y)\mu_s(x,y)\Big\}^k \frac{1-\exp\big\{-\mu_s(x,y)/a\big\}}{1-\exp\big\{\mu(x,y)/b\big\}} \tag{2.2}$$

where, I is the simulated brightness of Venus at each pixel (x, y) and μ_s and μdenote the cosines of the solar incidence angle (measured from vertical) and the emission angle, respectively. Following BELTON et al. [1991], the constants a, b, and c were set to 0.0547, 0.0039, and 0.9, respectively. Next, the simulated images were reprocessed through a Gaussian filter to emulate the seeing size (assuming the worst case scenario; 4.0 arcsec). The reprocessed simulated images are presented in the bottom row of Figure 2.4. The pixel corresponding to Venus' center was determined by finding the maximum of 2D cross-correlation coefficient between the obtained and simulated images. We have tested several assumed seeing-size, and the differences in seeing size were confirmed as negligible in this procedure. The spatial resolution ranges from 1500 km to 4000 km, depending on the angular diameter of Venus, in the equatorial region with 3.0 arcsec seeing.

Figure 2.9 shows the daily obtained images showing the variation in UV contrast. It can be confirmed in these images that latitudinal bright and dark pattern changes.

When we consider measuring the brightness variation, we must calibrate the extinction of the Earth ' s atmosphere. Such calibration is usually accomplished by observing photometric standard stars. However, the simultaneous imaging of Venus and standard stars from the Earth is quite challenging, because there are few available standard stars bright enough to be observed under the condition of backgrounds with strong scattering at 365 nm. Therefore, we develop an alternative method that we retrieve periodical rotation of planetary-scale feature by using normalized the brightness in each latitudinal band by the mean brightness in the 55°N–55°S area of the same image.

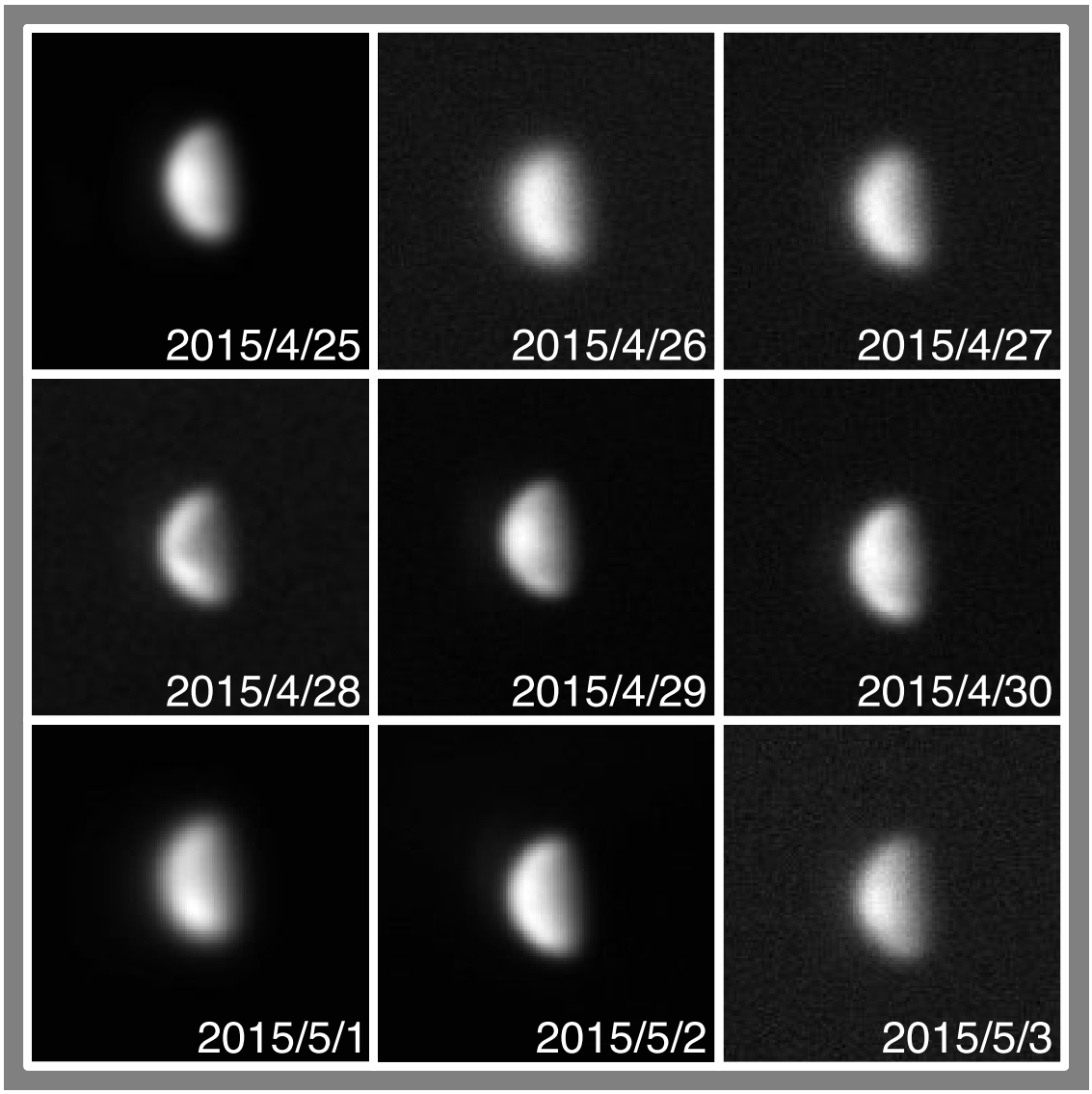

Figure 2.9: Sample of daily obtained Venus images taken with 365 nm.

The normalization formula is given by

$$R(\theta, t) = B(\theta, t)/\Sigma_{\text{latitude}} B(\theta', t) \tag{2.3}$$

where R and B denote the relative brightness and mean brightness (in ADUs), respectively, of the latitudinal band θ at time t. The investigated regions covered 30° × 10° (longitude × latitude), and the center longitudes of the regions were located within 7 hr, 16 hr, or 8 hr of the Venus dayside for each observational period. The latitudinal bands were centered at 0°, ±10°, ±20°, ±30°, ±40°, ±50° and ±60°.

It should be noted that the Venus images observed with the ground-based telescope were blurred by the rather severe seeing conditions. Moreover, this blurring effect cannot be correctly reproduced by PSFs in a simple form of Gaussian or Moffat function. For this reason, we did not correct for geometric scattering in our images. The blurring effect on the final results will argued in Section 4.3. The calculated R is the average of all images taken in one-day observation sequence. During the averaging process, we set the mean observation time as average of observation times t. This assumption is reasonable because the most extended duration of an observation sequence was ∼5 hr, and measured planetary-scale feature does not immigrate enough distance within the 30° × 10° investigated region. The R values also vary over timescales of a few weeks because the observed UV contrast depends on the observation geometry such as the phase angle (see Fig. 11 of Lee et al. [2015]. Since our target periodicity is ranging 3–7 days based on previous observations, these longer variation in relative brightness should be eliminated. Therefore, we first linearly detrended the temporal change in relative brightness for each latitudinal band with respect to time (t). Then, the mean brightness of each latitudinal band proceed to be equals 1. The detrending process enables the construction of contour plots (see Figure 2.11–2.14) and reveals the propagation of the planetary-scale UV feature. The average standard deviations of the relative brightness in the 0° and ±50°latitude are 0.05 and 0.16, respectively.

2.4 Relative brightness variation in data

After the above-described procedures, the differences in the amount of atmospheric extinction among the images can be considered negligible, and the variation of the

latitudinal brightness reflected the propagation of planetary-scale features. Figure 2.5 is the schematic illustration of the image analysis retrieving the relative brightness variation during one cycle of planetary-scale (Y-shaped) feature. In the figure, the bottom of the Y-feature initially faces the Earth (day 1), and the latitudinal profile is relatively dark in the EQ and mid-latitudinal regions. Throughout the following day, the EQ region remains relatively dark while the mid-latitudinal regions brighten. Later in the cycle, the EQ and mid-latitudinal regions become bright and dark, respectively. On day 5, the profile returns to that of day 1.

To evaluate the plausibility of this method for extracting the daily brightness variation, we processed Venus violet images obtained by the solid state imaging (SSI) system aboard the Galileo spacecraft, which reveal the global aspect of the Y-feature. We have confirmed that removing the scattering effect of the observation geometry made a negligible impact on the result. The large Y-feature has a prominent structure with four propagation characteristics; (1) a cyclic bright–dark pattern in the EQ and the north and south mid-latitudinal (SM) regions, (2) inverted phase of the bright–dark pattern in the EQ and mid-latitude regions, (3) brightness inversion at latitudes $\sim 30^{\circ}$, and (4) synchronized brightness in the northern and southern mid-latitudinal areas, leading to a symmetric distribution about the equator. The agreement between the ground-based data on August 2013 and the VEX/VMC data in the same observational period was confirmed in Imai et al. [2016]. In this paper, the periodicities in relative brightness variation measured with Pirka telescope were compared with the periodicities in the variation of absolute brightness. The analyzed VMC images were selected as the observation geometry is nearly same, and it was confirmed that relative brightness variation correctly reflects the periodical variation in absolute brightness. However, here we should note that the measured periodicities in relative brightness variation for each latitudinal band do not always directly correspond to the wave existence in that latitude. It means it should be careful to discuss the measured amplitude of two or more periodic mode could not compare directly. Because we normalize the measured brightness based on the mean brightness in all latitudinal bands to calculate latitudinal relative brightness, the variations even with weak amplitude can be magnified by this normalizing process, and some modes should reflect the periodical variation in other latitudinal regions.

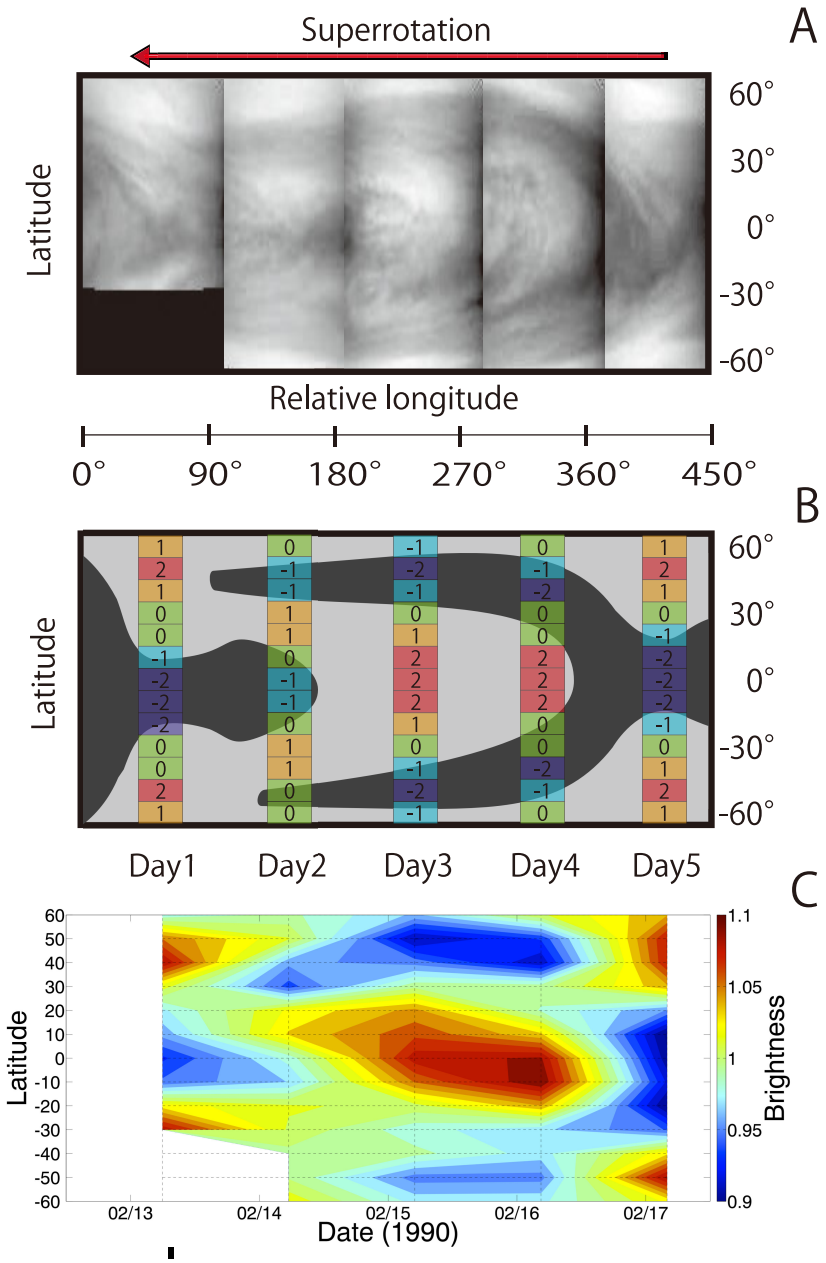

Figure 2.10: Illustration of our analysis method for measuring the relative latitudinal profile of UV brightness. Panel A shows the combined actual violet images taken by the Galileo spacecraft. Panel B shows the scheme for measuring the relative latitudinal brightness variation. In this simplified example, the latitudinal distributions of the UV brightness on each observation day are represented by 5 colors and 5 numbers (-2 to 2). Panel C presents our analysis result of the Galileo obtained images in Panel A. Red and blue areas indicate relatively bright and dark latitudes, respectively. Along the super-rotation, the latitudinal varies over the 5 days, revealing the propagation of the planetary-scale features. The detail of the calibration procedure with Galileo images is described in Section 3.2 of Imai et al. [2016]

The time variations of the relative UV brightness derived from our ground-based observations are presented in Figure 2.11–2.14. Here, the relative brightness (color level) is the mean brightness in the given latitudinal band normalized by that of the 55°N–55°S area. Intervals of each data points were linearly interpolated to draw the color contours. These figures show the UV brightness distributes from 50°N to 50°S on each observation day. Although images were acquired on each day of the observation period, some data were obliterated by bad weather conditions, but the data gaps are left uncolored in these figures to clarify the presumable brightness pattern.

The continuous periodic signatures of the propagating planetary-scale features can be deduced in each observational period. The bright and dark patterns periodically alternate and are symmetric about the equator. In the EQ and the 30°–50° latitudinal regions of both hemispheres, the brightness strongly varies over the ∼5-day period. This brightness variation is approximate anti-phase between the EQ and mid-latitudinal regions, where phase inversion occurs near 30°N and 30°S. Figure 2.15–2.17 shows the time variation of the relative brightness averaged within the equatorial region (from 10°N to 10°S). Further analysis of periodicities in observed brightness variations was described in later Section 4.

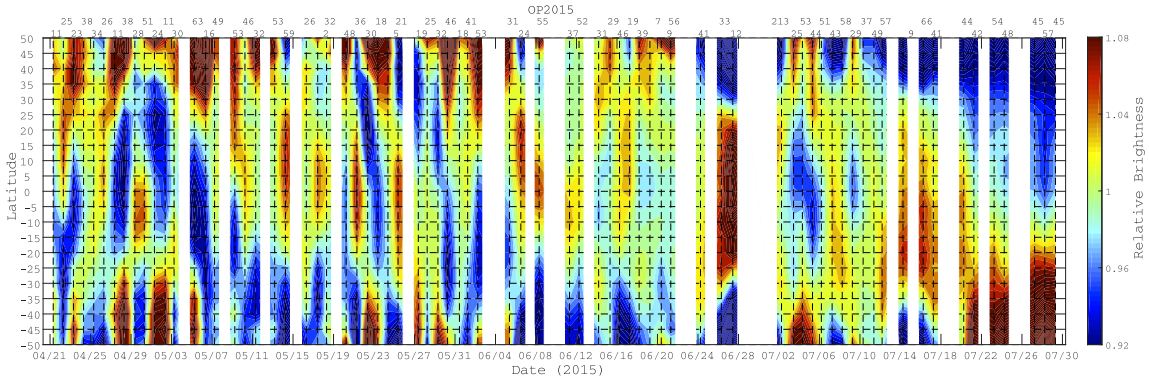

Figure 2.11: Brightness variations as functions of latitude on observation days of OP2015. White regions indicate missing data. The z-axis corresponds to the relative brightness, and the grid lines (dashed lines) depict the temporal/spatial resolution. The colored regions are linearly interpolated between the data points. The numbers along the top of each panel indicate the number of used images.

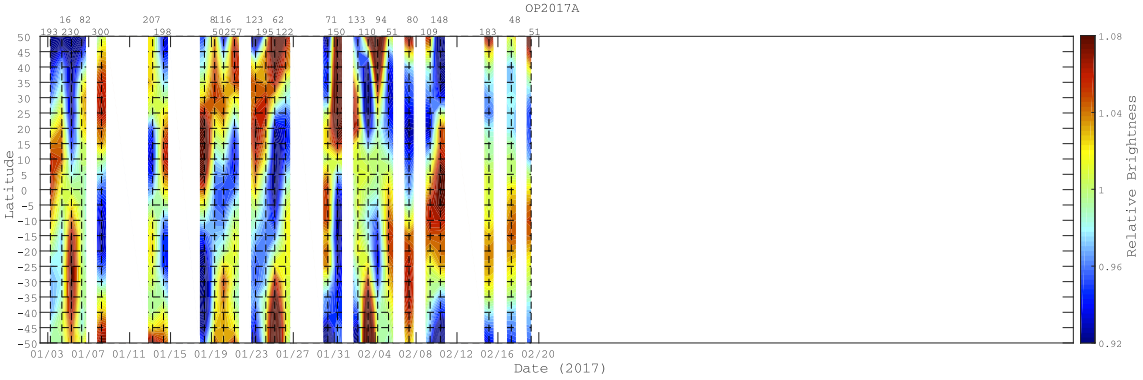

Figure 2.12: Brightness variations as functions of latitude on observation days of OP2017A-1 drawing in the same manner of Fig. 2.11.

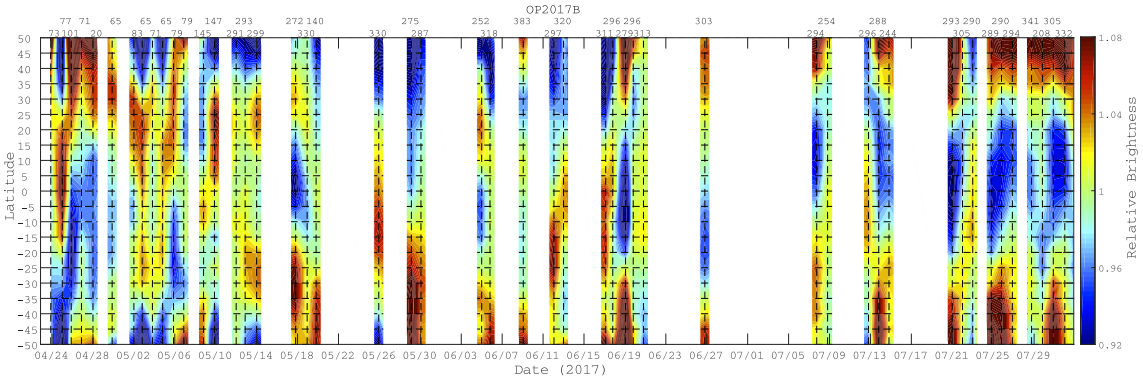

Figure 2.13: Brightness variations as functions of latitude on observation days of OP2017A-2 drawing in the same manner of 2.11.

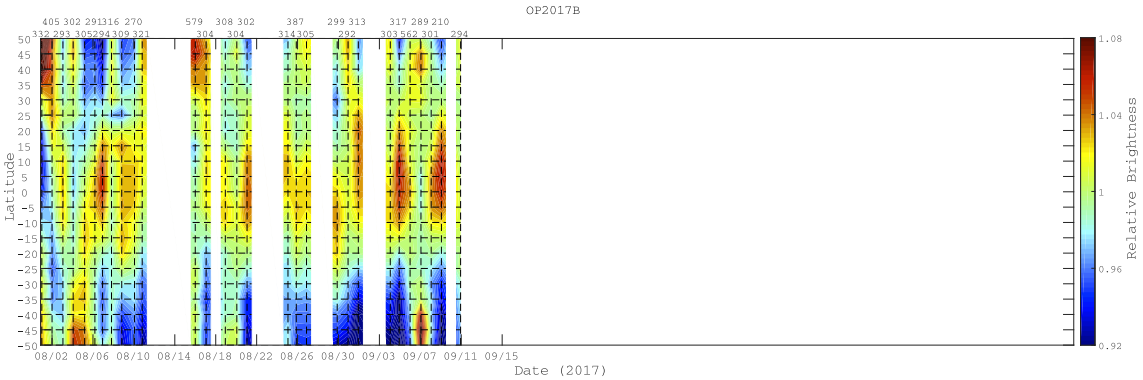

Figure 2.14: Brightness variations as functions of latitude on observation days of OP2017B drawing in the same manner of 2.11.

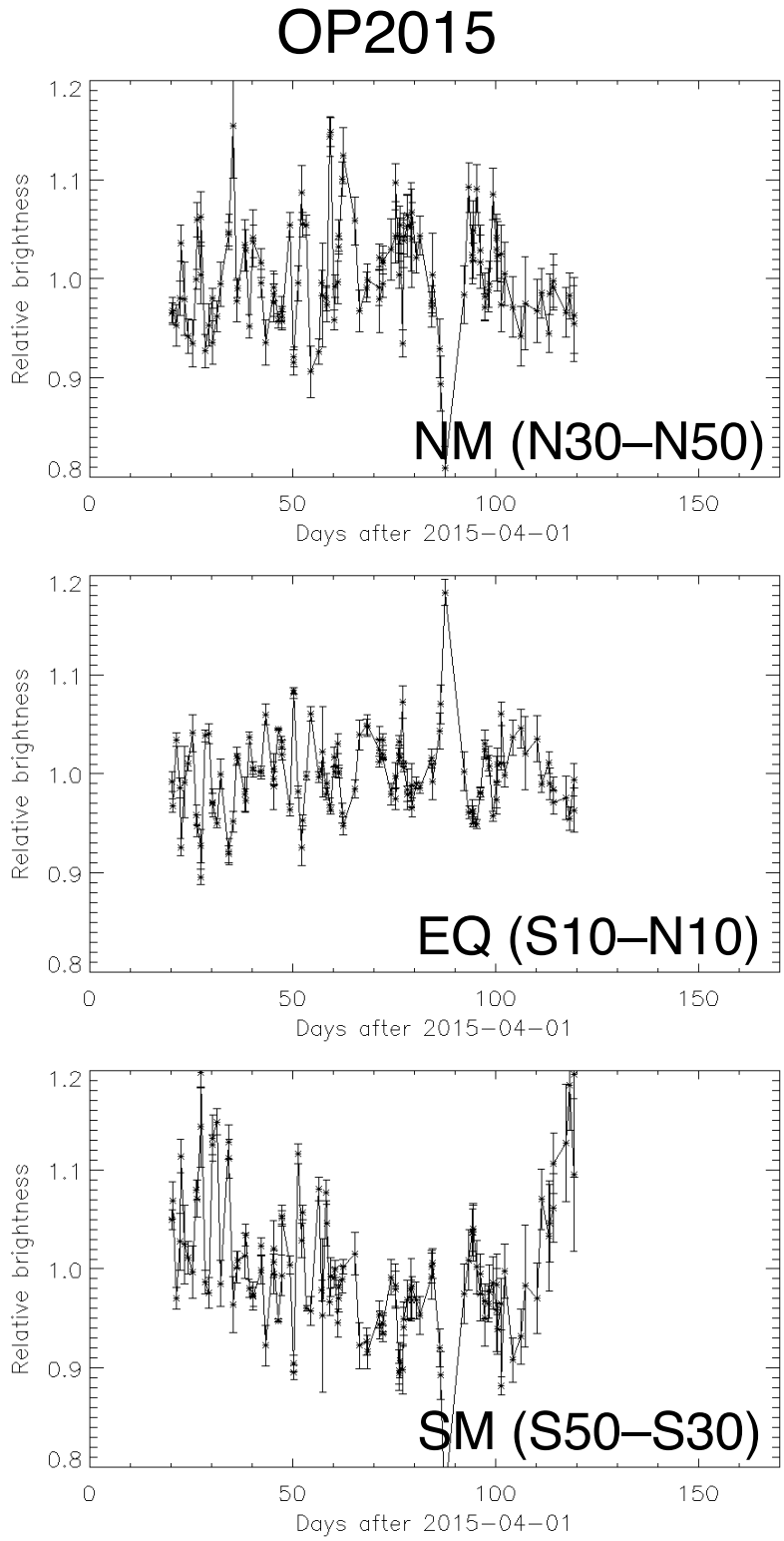

Figure 2.15: Brightness variation in OP2015 at each latitudinal region for SM(50°S–30°S), EQ(10°S–10°N), and NM(30°–50°). Each point is plotted at averaged relative brightness with error bars of the standard deviation in a day.

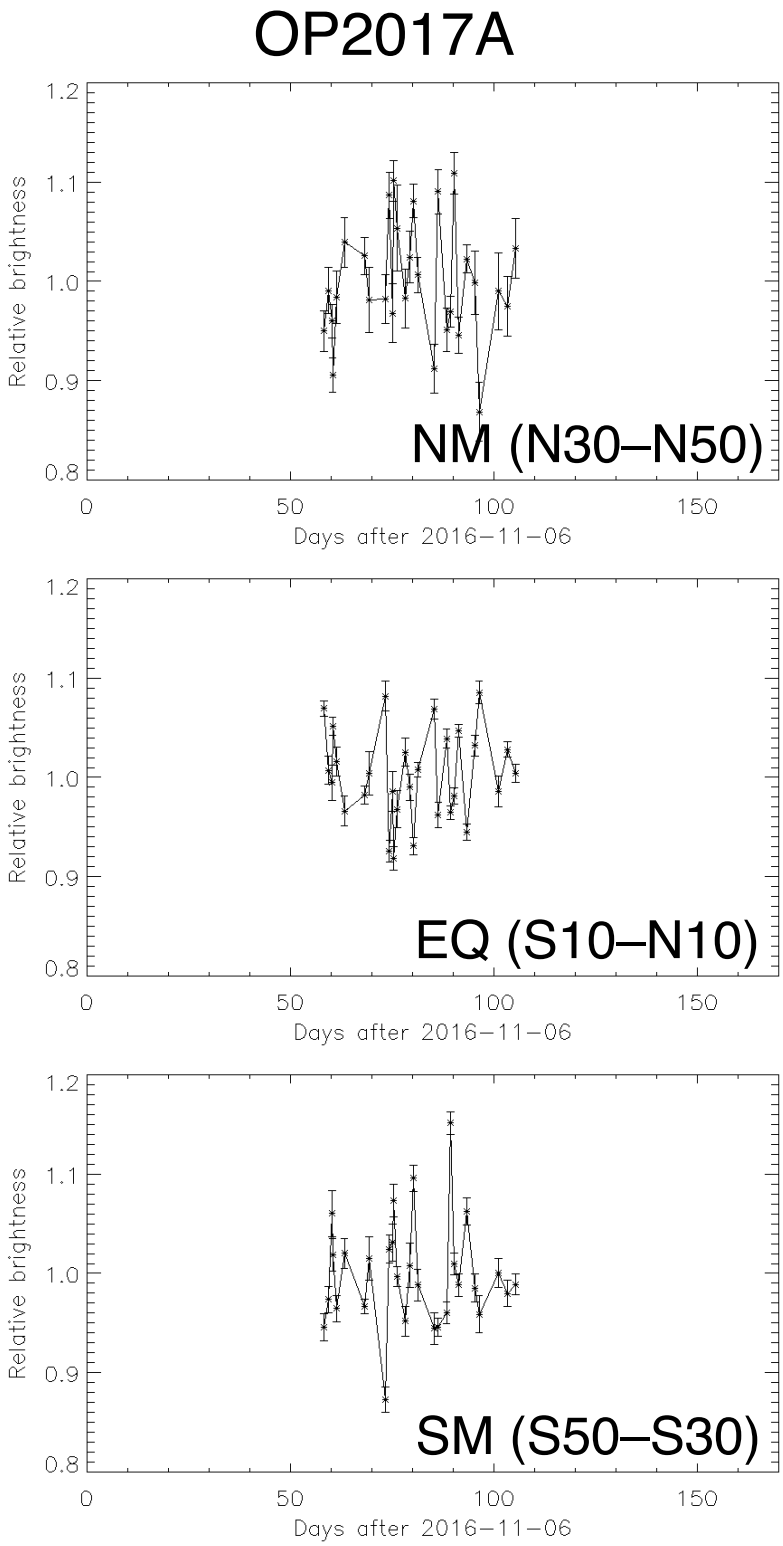

Figure 2.16: Same figure as Fig. 2.15 for OP2017A.

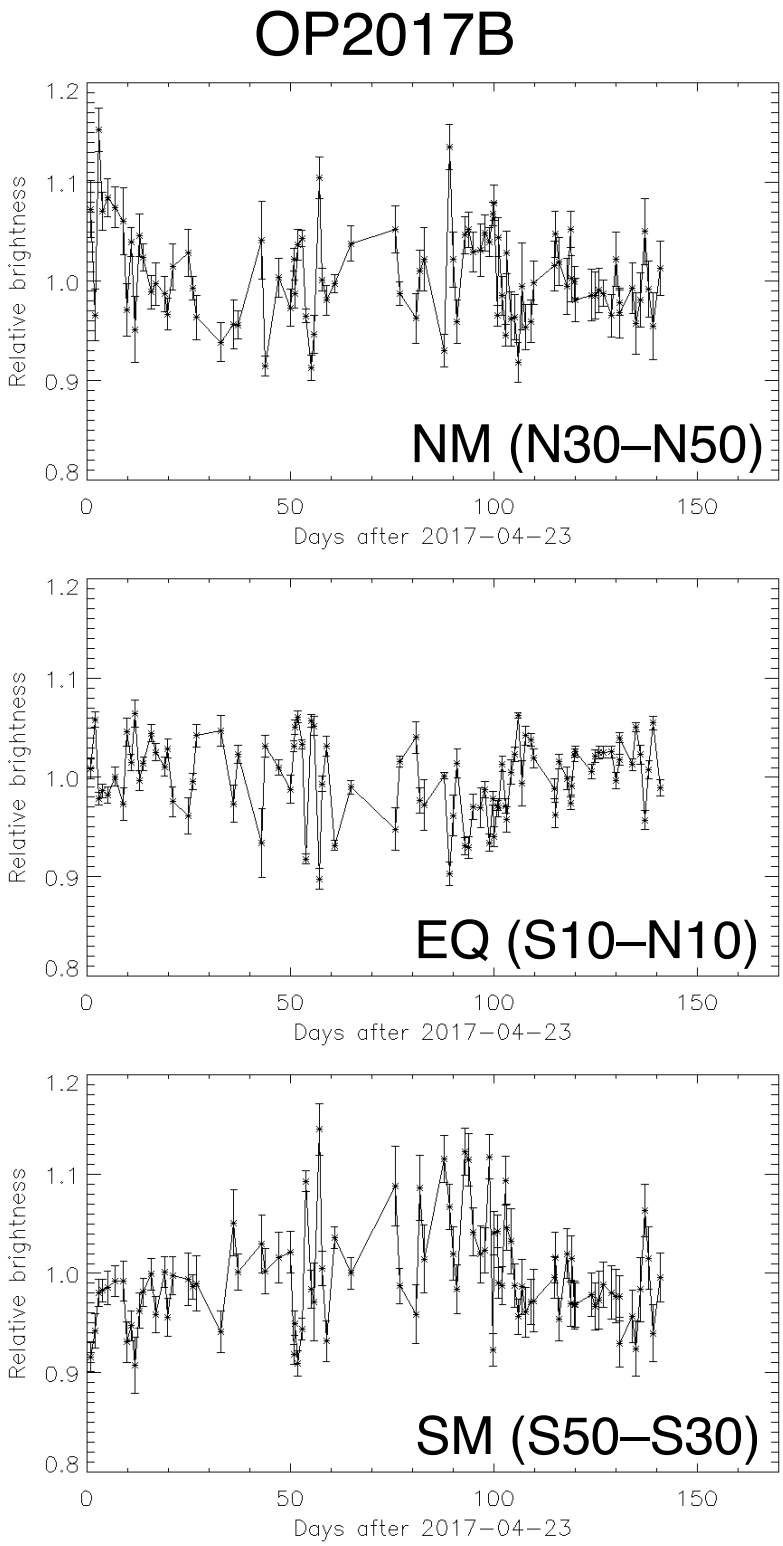

Figure 2.17: Same figure as Fig. 2.15 for OP2017B including data observed with Kanata telescope.

3 Observation and data analysis of Space-based images

In this section, the details observation of AKATSUKI and UVI and analysis of obtained images are described. UVI data is used as the reference of cross-comparison between ground-based and space-based observation data. The complementary information could be provided when the ground-based observation was difficult. Additionally, the high-spatial resolved image allows us to measure the zonal wind velocity by tracking the mesoscale cloud features.

3.1 Dataset in analysis

The orbital plane of AKATSUKI is fixed into the inertial frame of reference, therefore in the same situation of the previous spacecraft, and the sub-spacecraft local time at pericentre (or apocentre) gradually changes, and it can be divided into two observation condition which is appropriate for dayside monitoring or nightside. Figure 3.1 depicts the representative Venus views from several observation geometries during January 14 to February 16, 2017 (orbit number 38 to 40) as a part of OP2017A. In this season, the pericentre located dayside and onboard cameras could capture almost full dayside disc for a longer time. The mission still ongoing and is under planned to be extended for 2020. Analyzed data in this study was selected as the following criteria, that Venus–Spacecraft distance ranging from 70,000 km to 370,000 km and sub-spacecraft local time was in 6 hr to 18 hr to capture the global view and sufficient range of Venus dayside. The corresponding spatial resolution is 15–75 km at the equator.

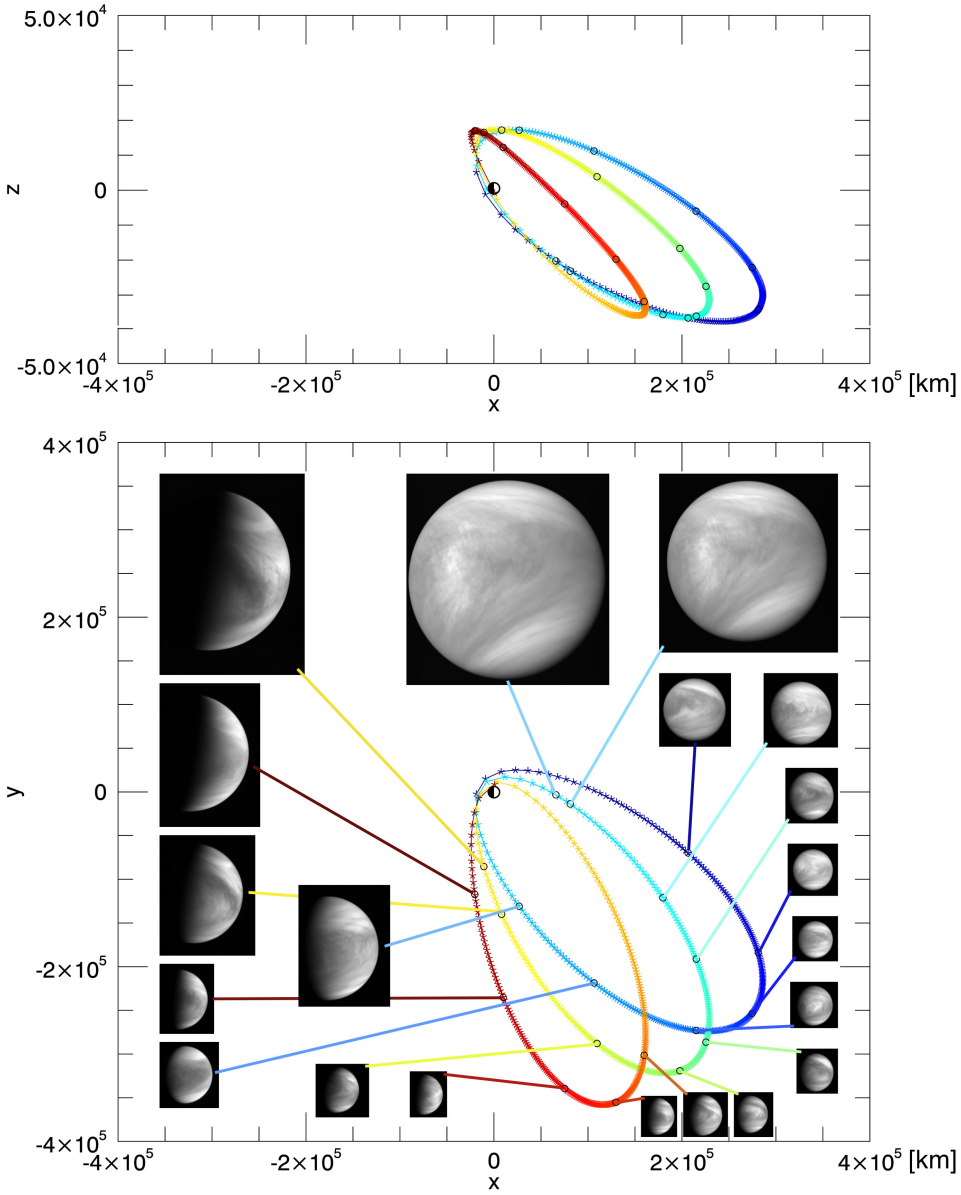

Figure 3.1: Representative global view images of Venus obtained by UVI for each observation geometry during the orbit of #38–40 as the color plots changing from blue to red. XY-plane is a plane of Venus's orbit at the reference epoch of J2000.0 and Z-axis is perpendicular to the XY-plane in the directional sense of Venus's north pole. Upper panel shows the AKATSUKI orbits in the XZ-plane and bottom panel shows in the XY-plane. Sub-spacecraft local time at the apocentre gradually changes from evening side to morning side for each ∼10 days orbit, and the high eccentricity allows to obtain images continuously around the apocentre.

Our first intend analyzing UVI data is to validate the ground-based result by comparing different two types of dataset. Therefore, we selected UVI images which

were taken during the same observation period as the ground-based observation. Additionally, since the UVI can obtain a lot of images in the favorable season for observing Venus dayside when the apoapsis of the spacecraft located in dayside ranging the half of Venus orbital period of 224 days, extending the target period beyond the ground-based observation period is our second object.

UVI images in two different seasons are treated in this thesis as the following date (and orbit No. of AKATSUKI).
· OP2017A: 06/11/2016–11/03/2017 (r0031–r0043)
· OP2017B: 15/06/2017–31/09/2017 (r0051–r0061)

The label corresponds to the observation period of ground-based data, and we selected Venus images with criteria that, sub-spacecraft point exist between 6-hr and 18-hr local time approximately corresponds to the phase angle lower than 90 deg. Observed images with 365 nm filter of UVI are used, and some of them are excluded manually as bad images such as the images suffered losses in the image field, unnaturally flat-fielded or navigated with incorrect geometry information.

There are several levels of products in UVI data as follow,

- Level 1b (l1b) is the raw data after the flat-fielding procedure,
- Level 2b (l2b) is the calibrated data with a physical unit of W/m2/sr/m,
- Geometry (geo) is the geometry information data including latitude, longitude, local time, phase angle, incidence angle, emission angle, and the azimuthal angle at the center of each pixel,
- Level 3 (l3, l3x) is the calibrated data with physical values at equally spaced longitude-latitude grid in NetCDF format derived from l2b data (l3) and pointing corrected geometry information at the center of each pixel (l3x). We mainly use the l2b and l3x data and, here we should note that the version of data in use is v20171201 of internal release (not public open) and they have some possibility to be modified their pixel value or attached geometry information. However, our results could be derived from the relative brightness value or brightness pattern. Therefore the minor change for example in a conversion factor of counts to flux has negligible effects on them. Unnaturally flat-fielding

or incorrect geometry information can cause strange on check figure like Figure 3.2, so it is easy to find and extract such data manually. Most of the hot pixels in images caused by, e.g., cosmic-rays hit are excluded by the onboard median combining process with five flames for Venus and dark respectively In this study, dead or bad pixels cannot be confirmed and treated they are negligible.

3.2 Basic image processing

In this section, the details of image processing are described with the sample products of Figure 3.2. Provided Venus images (A) are scattered data value on a sphere. At first, each image is projected into two-dimensional longitude (0°–360°) and latitude (60°S–60°N) map with 0.25° × 0.25° resolution. In this projection procedure, only the valid longitudinal area, which defines as the differential angle from sub-spacecraft and sub-solar longitude lower than 75°, are calculated. The geometry data of l3x helps to navigate the longitude and latitude of each pixel of the original image. The grid points of the original image are interpolated with quintic polynomials from triangles formed by Delaunay triangulation (a) (see Akima [1996]). The scattering properties of the Venus cloud at 365 nm channel was studied by Lee et al. [2017]. Their disk function D describes the dependence on scattering angle (i.e., angles of emergence (e) and incidence (i) and the phase angle (α)). Based on the empirical formula of Lee et al. [2017], D can be written as the combined Lambert and Lommel-Seeliger law (LLS) (Buratti and Veverka 1983 McEwen 1986),

$$D_{LLS} = k_{LLS}(\alpha)\frac{2\mu_0}{\mu_0 + \mu} + (1 - k_{LLS}(\alpha))\mu_0 \tag{3.4}$$

$$k_{LLS}(\alpha) = 0.257086 + 0.00102739\alpha - 1.45403 \times 10^{-5}\alpha^2 \tag{3.5}$$

where $\mu = \cos(e)$, $\mu_0 = \cos(i)$, and k_{LLS} is the coefficient describing relative contributions of Lambert and Lommel-Seeliger, i.e., 0 is pure Lambert law, and 1 is pure Lommel-Seeliger law. Corresponding simulated Venus disc images (B) are produced to eliminate the eliminate the limb darkening effect as the function of phase angle, cosine of incidence and emission angle. The simulated disc images also projected onto the map as (b). (c) is the brightness distribution map after the correction derived (a) divided by (b). (d) is a longitudinally smoothed image of (c) with a

Gaussian filter whose variance of $\sigma = 9°$. Finally, the mesoscale feature enhanced image is obtained by (c) - (d).

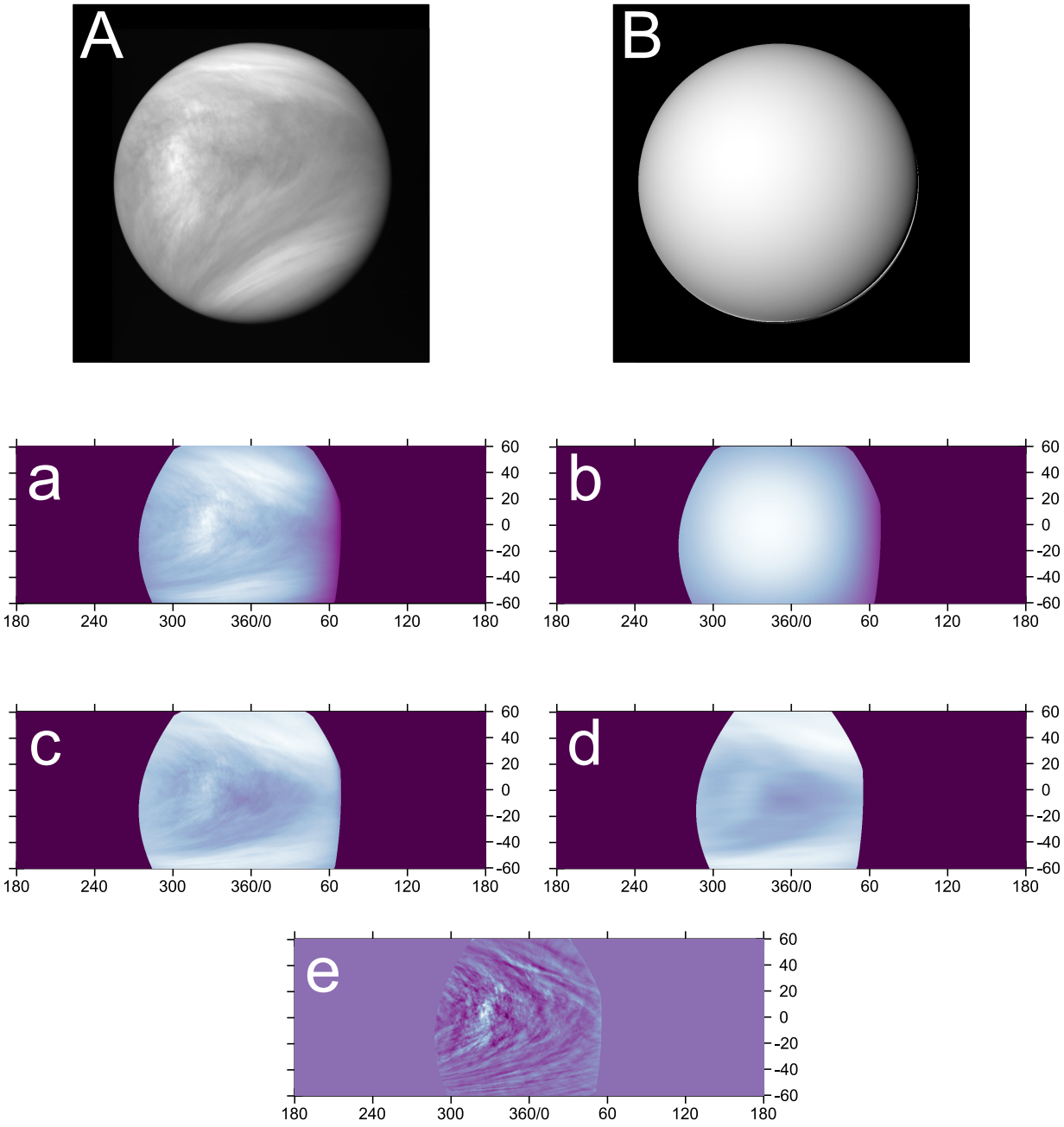

Figure 3.2: Sample images obtained through the basic image processing. A is an original Venus disc image of l2b data, and B is a simulated Venus assuming LLS scattering properties. a and b are projected map images of A and B respectively. c is a map image of after photometric correction, d is a low-pass image, and e is a high-pass image.

3.3 Time series of brightness variation

Brightness variation in UVI images is investigated for retrieving the propagation phase velocity or period of planetary-scale waves. Since some dependence of observation geometry (i.e., incidence, emission, and phase angle) in the observed brightness remain after the correction with LLS formula, we decided to calculate the relative brightness as the same manner of the MSI image analysis. The ratio of each 12 latitudinal bands with the 30° longitude and 10° latitude area size are calculated as the same formula of equation 2.3 used to analyze ground-based images . The 30° latitudinal area were selected to maximize the total acquired area for the all images during each observation period. Figure 3.3–3.8 depict the longitudinal range in the analysis. In the case of observation period 2017A, we make three groups, which could observe LT 9–11 hr for OP2017A-1, LT=11–13 hr for OP2017A-2, and LT=13–15 hr for OP2017A-3. In the same manner, observation period 2017B, we make groups of LT 9–11 hr for OP2017B-1, LT=11–13 hr for OP2017B-2, and LT=13–15 hr for OP2017B-3.

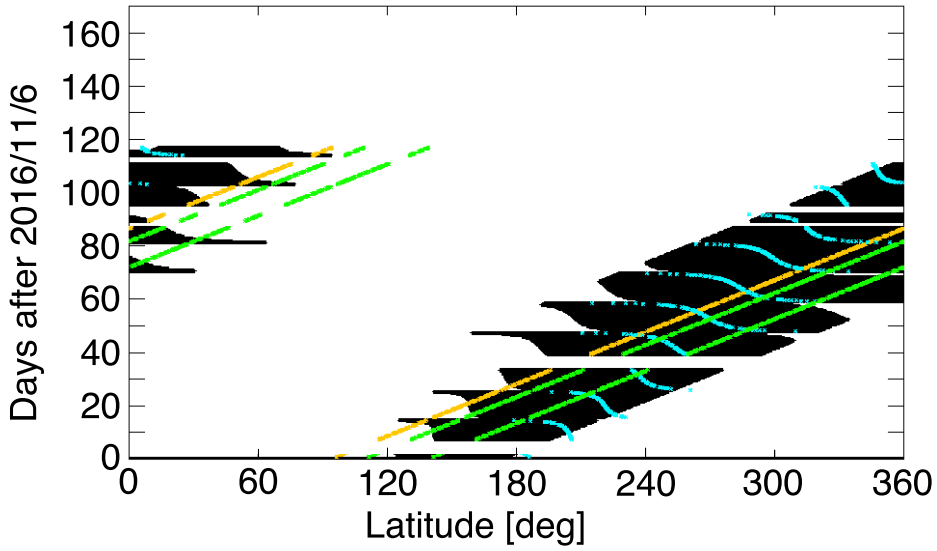

Figure 3.3: Observable longitudinal coverage for each image in the brightness variation analysis for OP2017A-1. Yellow plots indicate the sub-solar point and thus 12-hr local time point. Green plots show the corresponding longitudes of 9-hr and 11-hr local time.

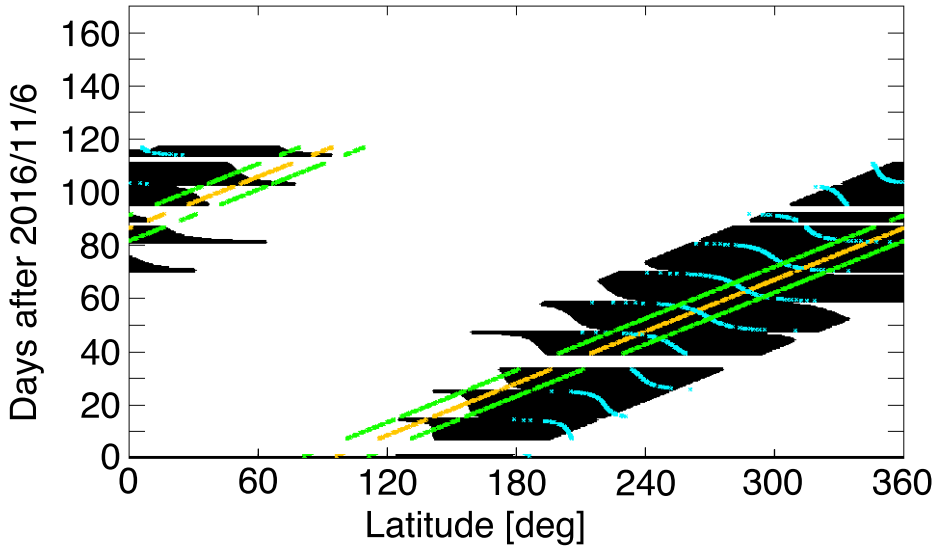

Figure 3.4: Observable longitudinal coverage for each image in the brightness variation analysis for OP2017A-2 as the same manner of figure 3-2. Green plots show the corresponding longitudes of 11-hr and 13-hr local time.

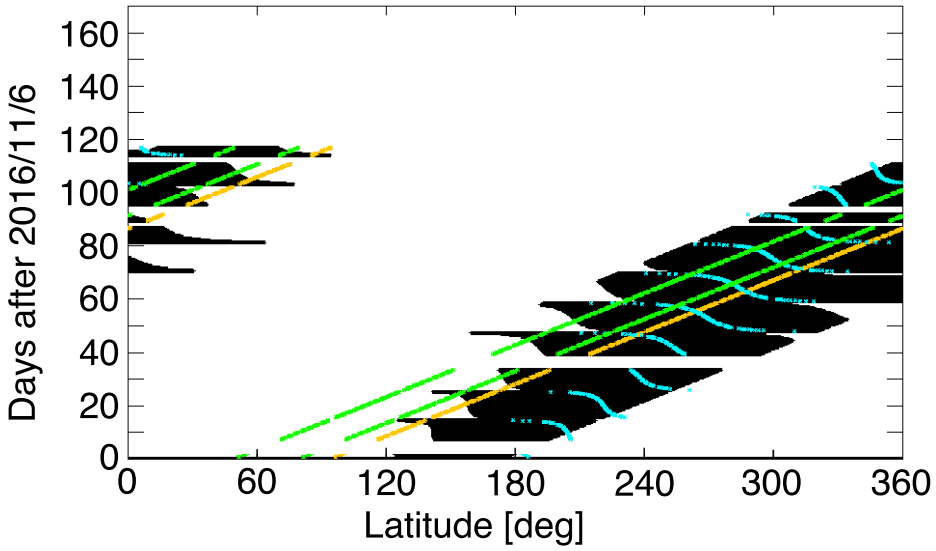

Figure 3.5: Observable longitudinal coverage for each image in the brightness variation analysis for OP2017A-3 as the same manner of figure 3-2. Green plots shows the corresponding longitudes of 13-hr and 15-hr local time.

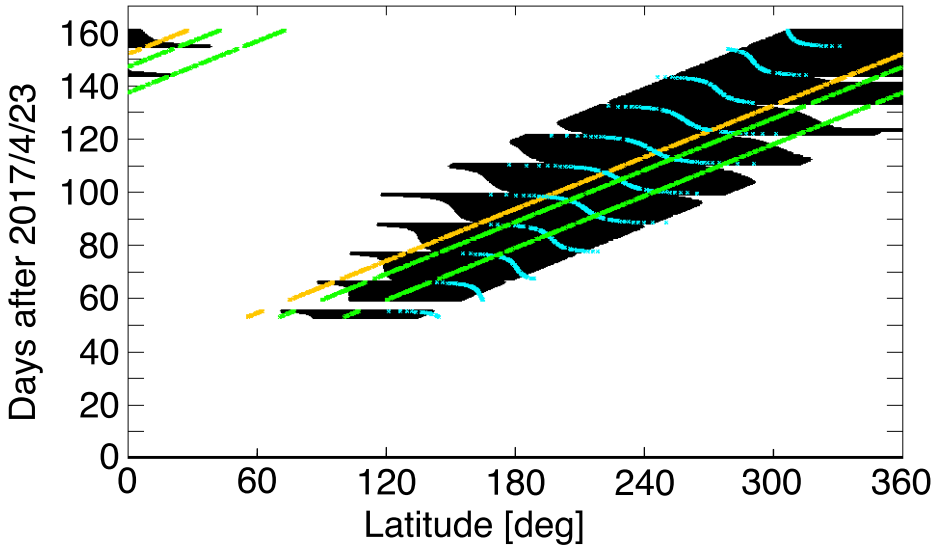

Figure 3.6: Observable longitudinal coverage for each image in the brightness variation analysis for OP2017B-1 as the same manner of figure 3-2. Green plots show the corresponding longitudes of 9-hr and 11-hr local time.

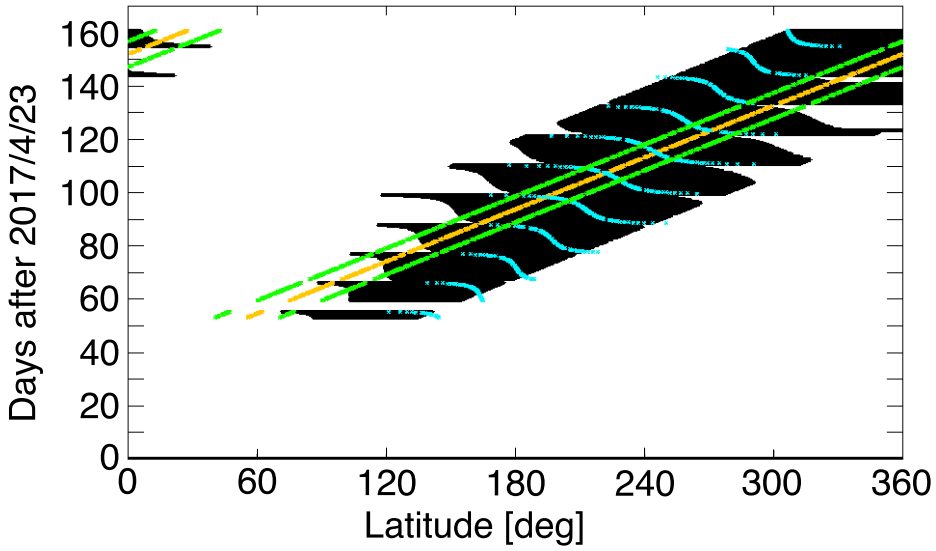

Figure 3.7: Observable longitudinal coverage for each image in the brightness variation analysis for OP2017B-2 as the same manner of figure 3-2. Green plots show the corresponding longitudes of 11-hr and 13-hr local time.

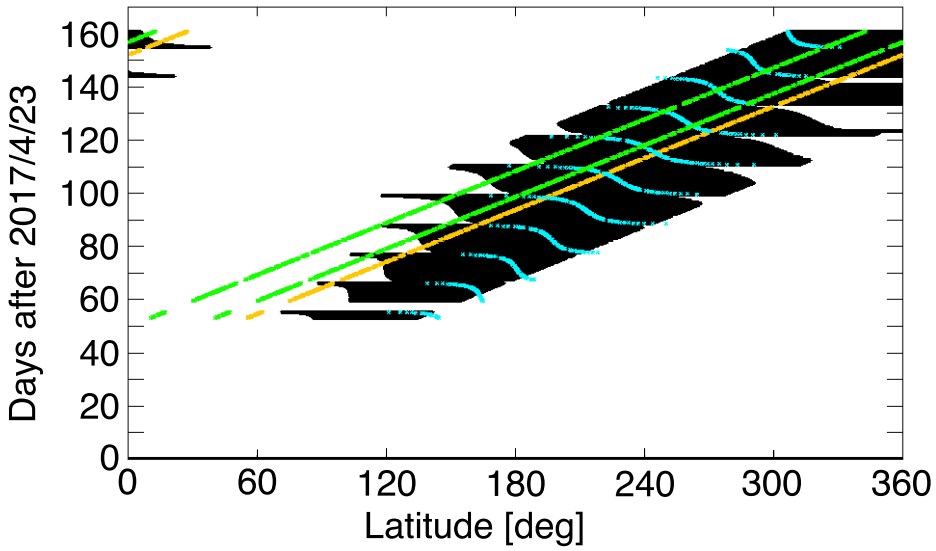

Figure 3.8: Observable longitudinal coverage for each image in the brightness variation analysis for OP2017B-3 as the same manner of figure 3-2. Green plots show the corresponding longitudes of 13-hr and 15-hr local time.

Figure 3.9–3.14 show the time series of the relative brightness variation for the three latitudinal regions of 50°S–30°S, 10°S–10°N, 30°N–50°N and two of observation. Based on these result, the periodicity is investigated as described in Section 4.

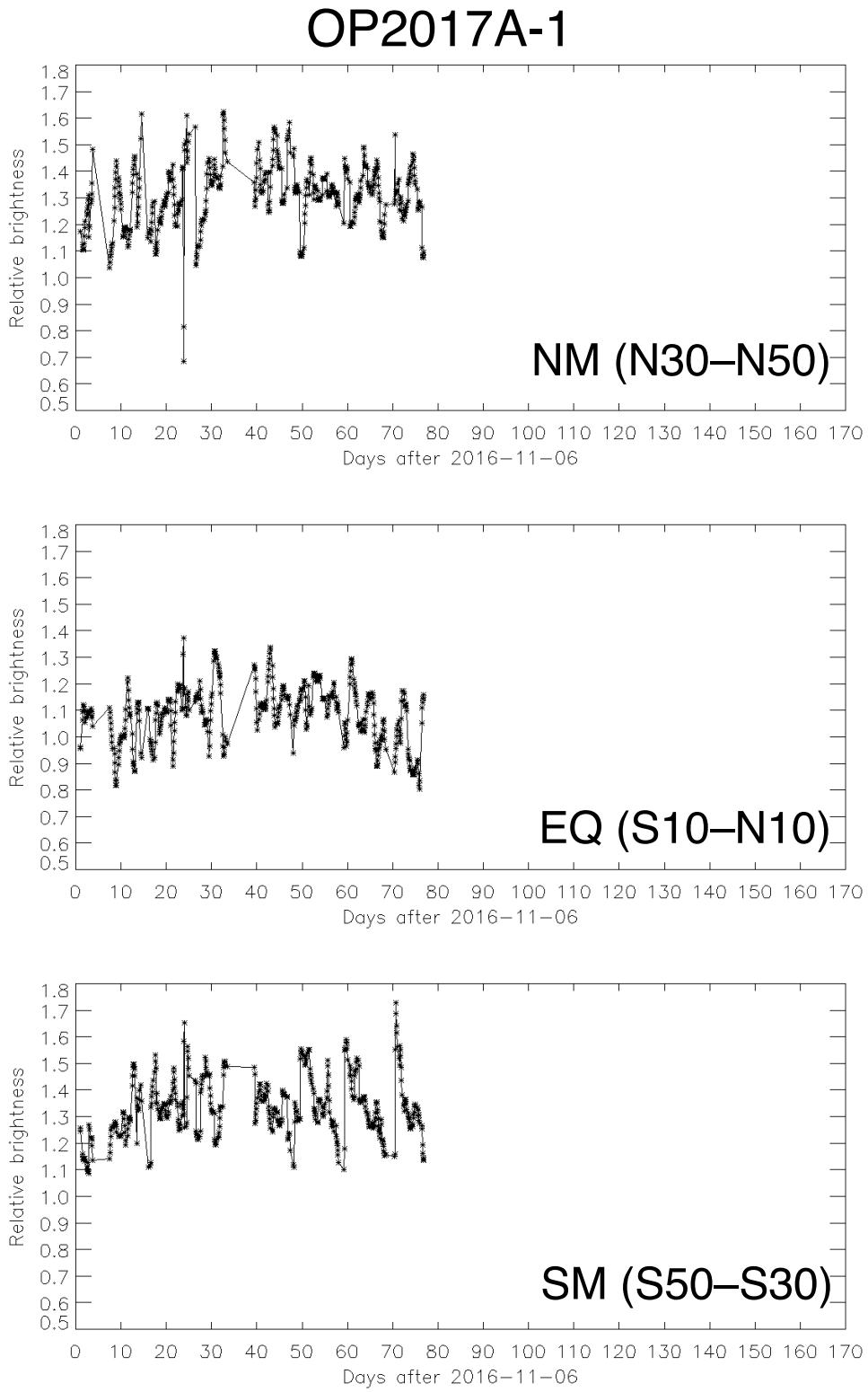

Figure 3.9: Brightness variation in OP2017A-1 in each latitudinal region of SM(50°S–30°S), EQ(10°S–10°N), and NM(30°N–50°N).

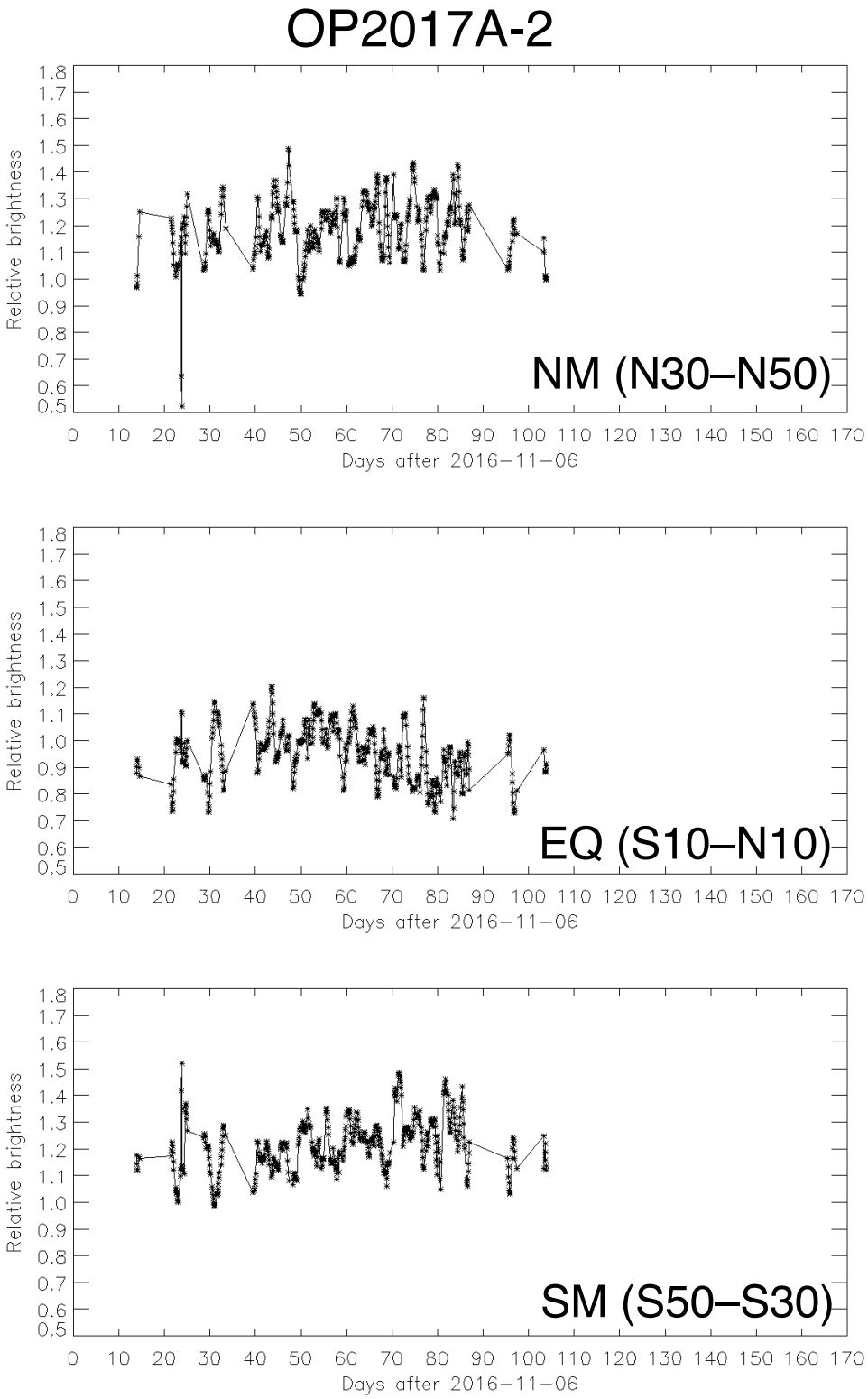

Figure 3.10: Same figure as Fig. 3.9 for OP2017A-2.

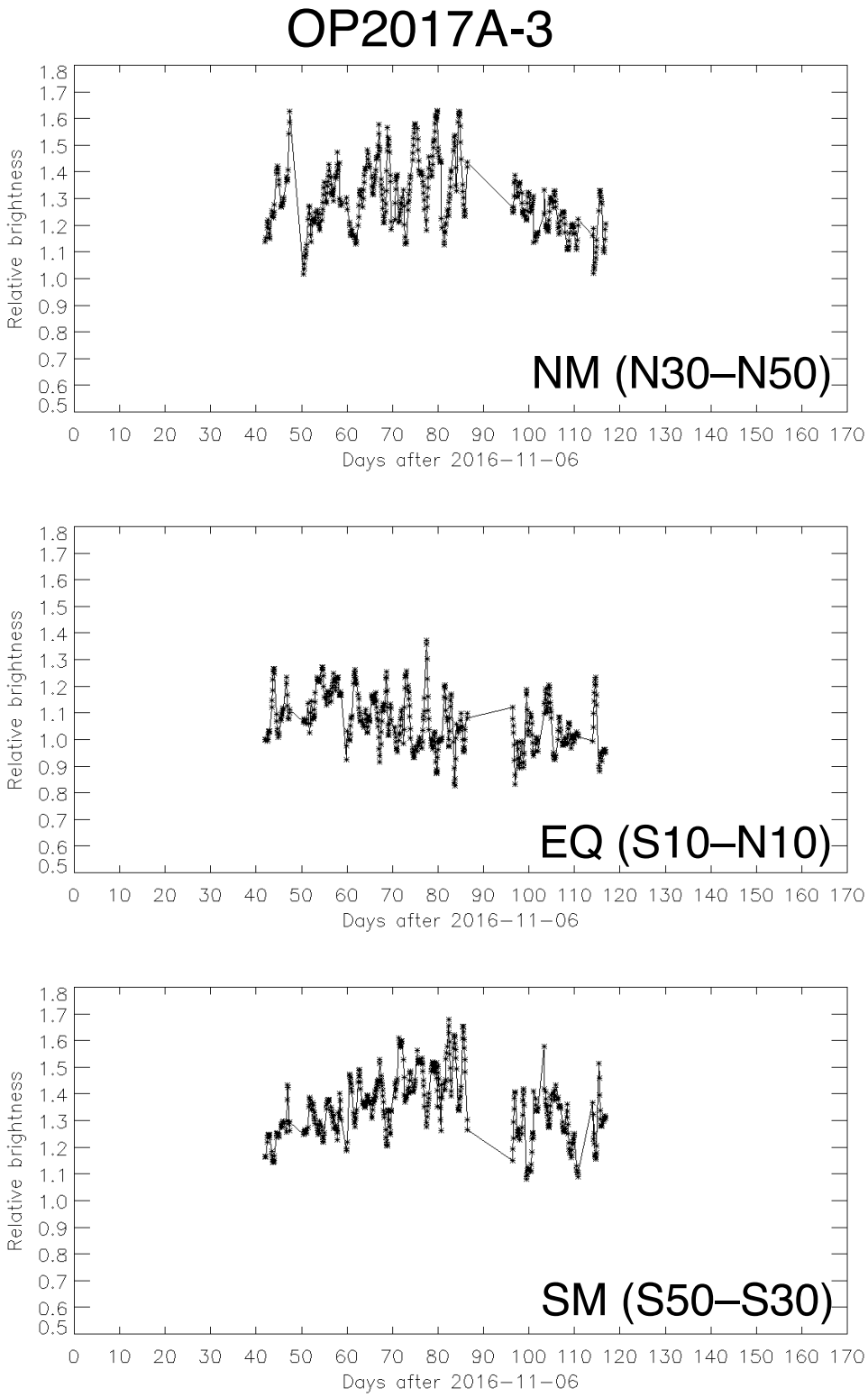

Figure 3.11: Same figure as Fig. 3.9 for OP2017A-3.

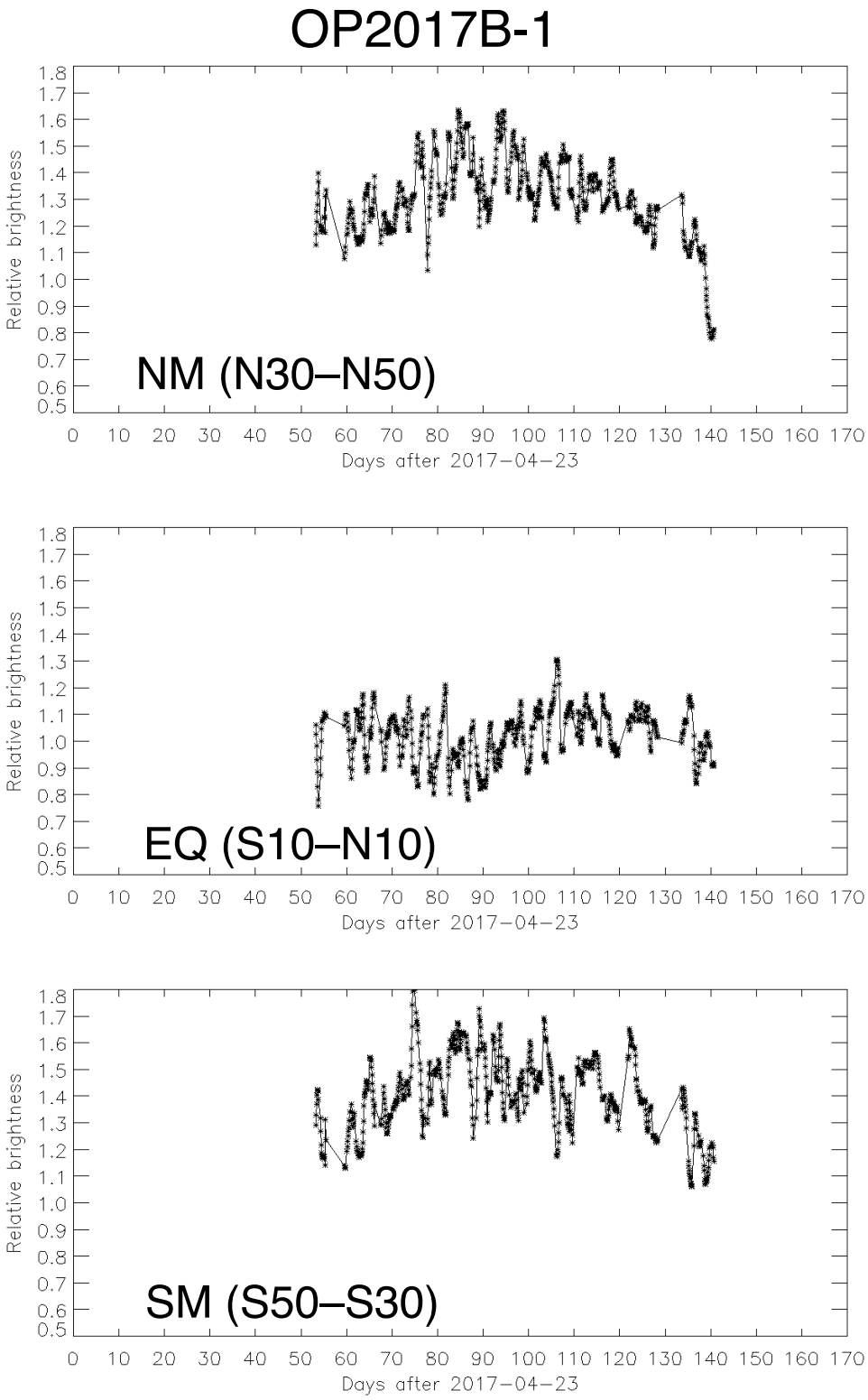

Figure 3.12: Same figure as Fig. 3.9 for OP2017B-1.

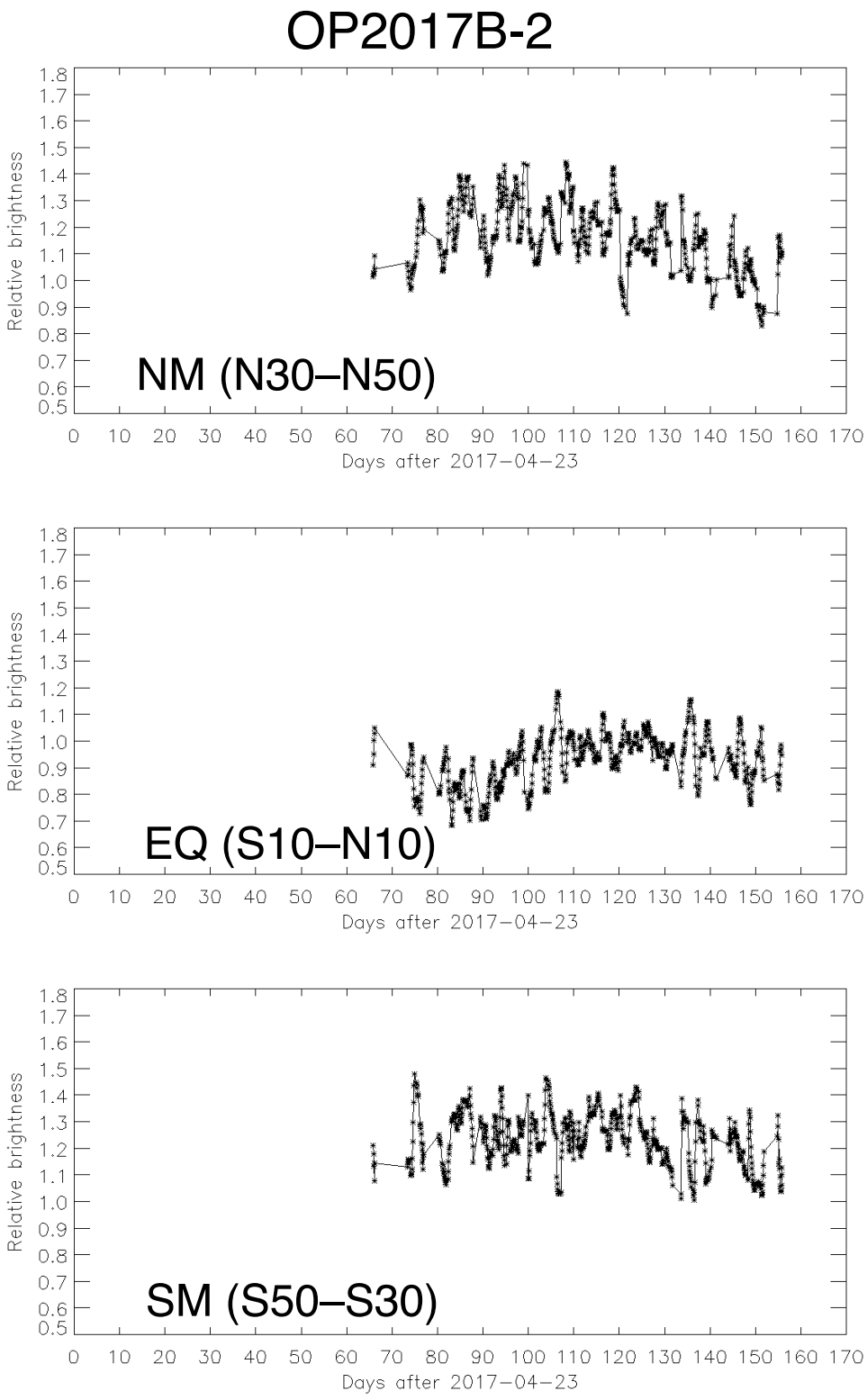

Figure 3.13: Same figure as Fig. 3.9 for OP2017B-2.

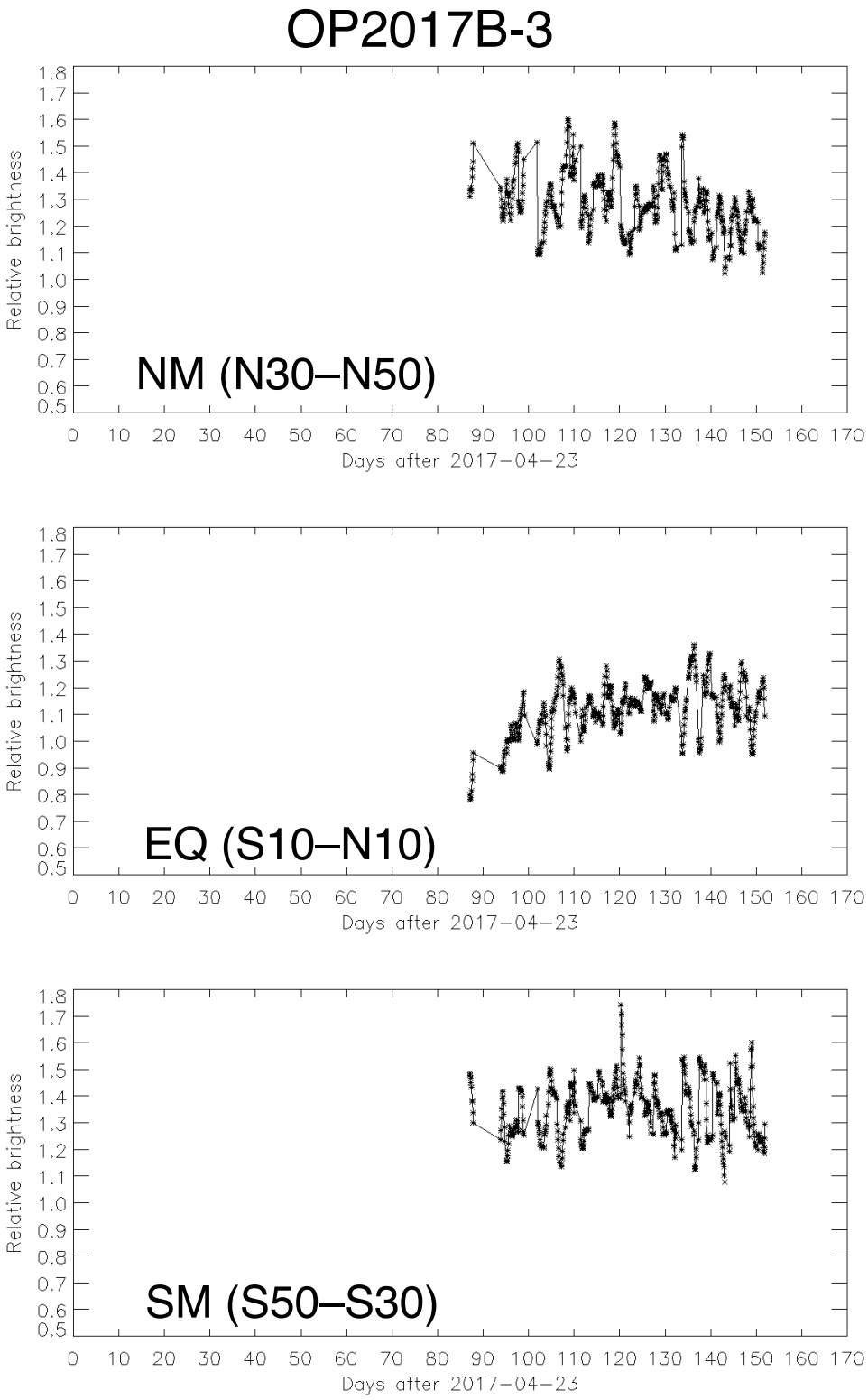

Figure 3.14: Same figure as Fig. 3.9 for OP2017B-3.

3.4 Measuring the zonal moving velocity of mesoscale cloud feature

To retrieve the information of zonal wind velocity, we conducted mesoscale feature (cloud) tracking with crosscorrelation method. This method was used to estimate horizontal wind velocity, assuming clouds are mainly advected horizontally. Using time separate pair images, the displacement of the mesoscale features can be used to estimate the background winds. Here we assumed that mesoscale features exist at the altitude of 65 km above the mean surface level of 6051.8 km from the center of Venus. This altitude value is commonly used, e.g., Horinouchi et al. [2017], the study of automatically analyzed wind velocity from cloud tracking team of the AKATSUKI project.

Two time-consequent images of UVI (nominal interval between the images is ∼2 hour) were used as a pair image to measure one zonal wind velocity for each latitudinal area form 50°S to 50°N. The longitudinal width of the latitudinal area depended on the size of the valid longitudinal area as defined before. Figure 3.15 shows 8 sample pairs of the latitudinal areas of 2.5°N. Using each pair of these latitudinal area, the sub-image area A and B are made for the calculation of the cross-correlation (Figure 3.16). The size of the sub-image is 120 × 20 pixels (30° lon. × 5° lat.), and the maximums of the 2D cross-correlation in the pair of two time-consecutive sub-images for the zonal (longitudinal) direction were searched by stepping the sub-images with 1 pixel.

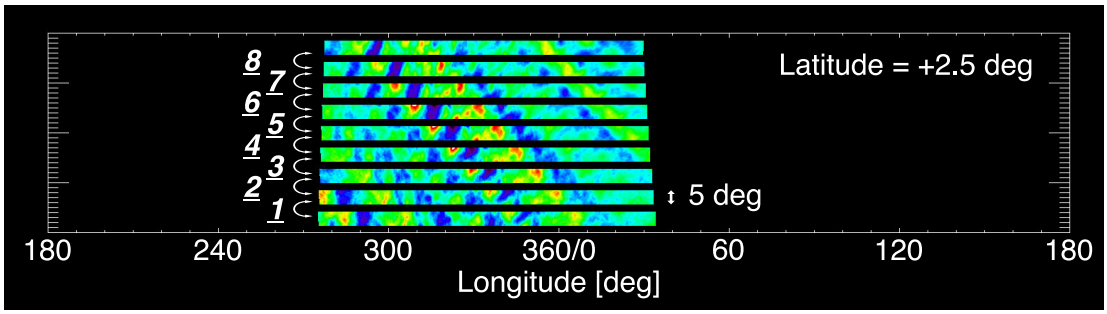

Figure 3.15: An example of color images of mesoscale UV features in a latitudinal band of 2.5°N fixed with geographic longitude. Each images having ∼2 hours interval are arranged vertically from bottom to top of the figure.

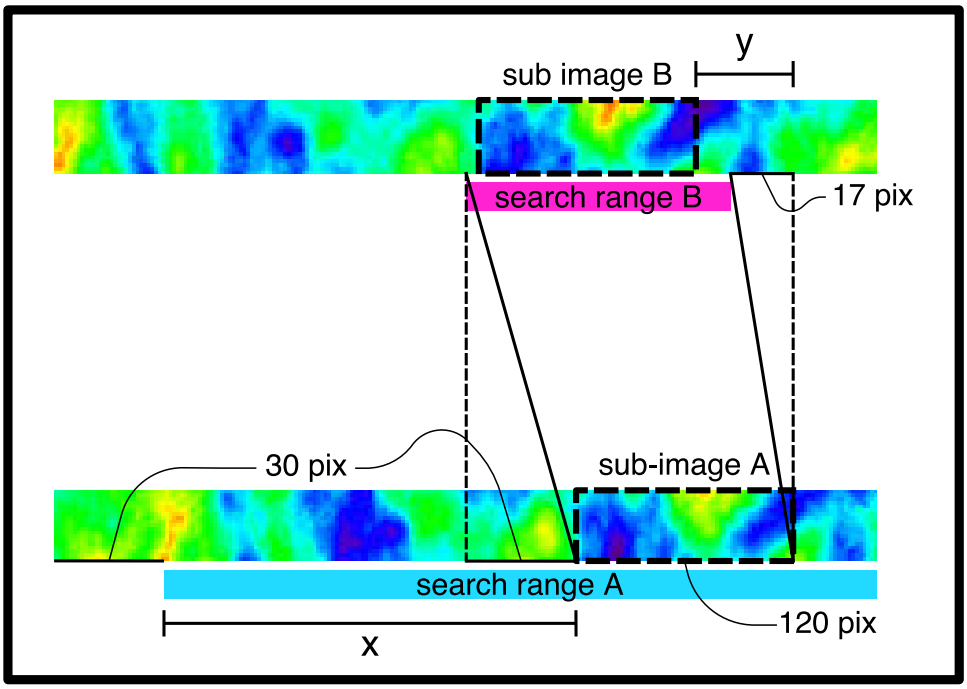

Figure 3.16: Schematic illustration of the zonal moving velocity of mesoscale feature by finding the local maxima of 2D cross correlation. The cross-correlations between the sub-image A and B are calculated every 1-pixel steps in the search range A and B. 30 pix and 17 pix are corresponding pixel numbers assuming the periods of the rotation around the planet with 3.0 days and 7.0 days respectively.

Figure 3.17 shows the results of calculated 2D cross-correlation for each pair of eight latitudinal areas. Each correlation curve (the Y-axial cross-section) was interpolated with 10 times higher resolution (0.025 deg). The amount of longitudinal shift between two images was estimated by finding 2D cross-correlation maximum as denoted with white plots. Here, only top 50% of the correlation value was taken into account of finding the maximum. Total average amount of the shift for the entire longitudinal region was used to estimate the final wind velocity (or rotation period). The standard deviation of estimated shift within the entire longitudinal area was used to calculate the error, and the results for mesoscale features were determined with a small error of $\pm$ 0.2 days period. Also, upper and lower limits of the zonal wind velocity were calculated which are displayed as the white lines in Figure 3.12.

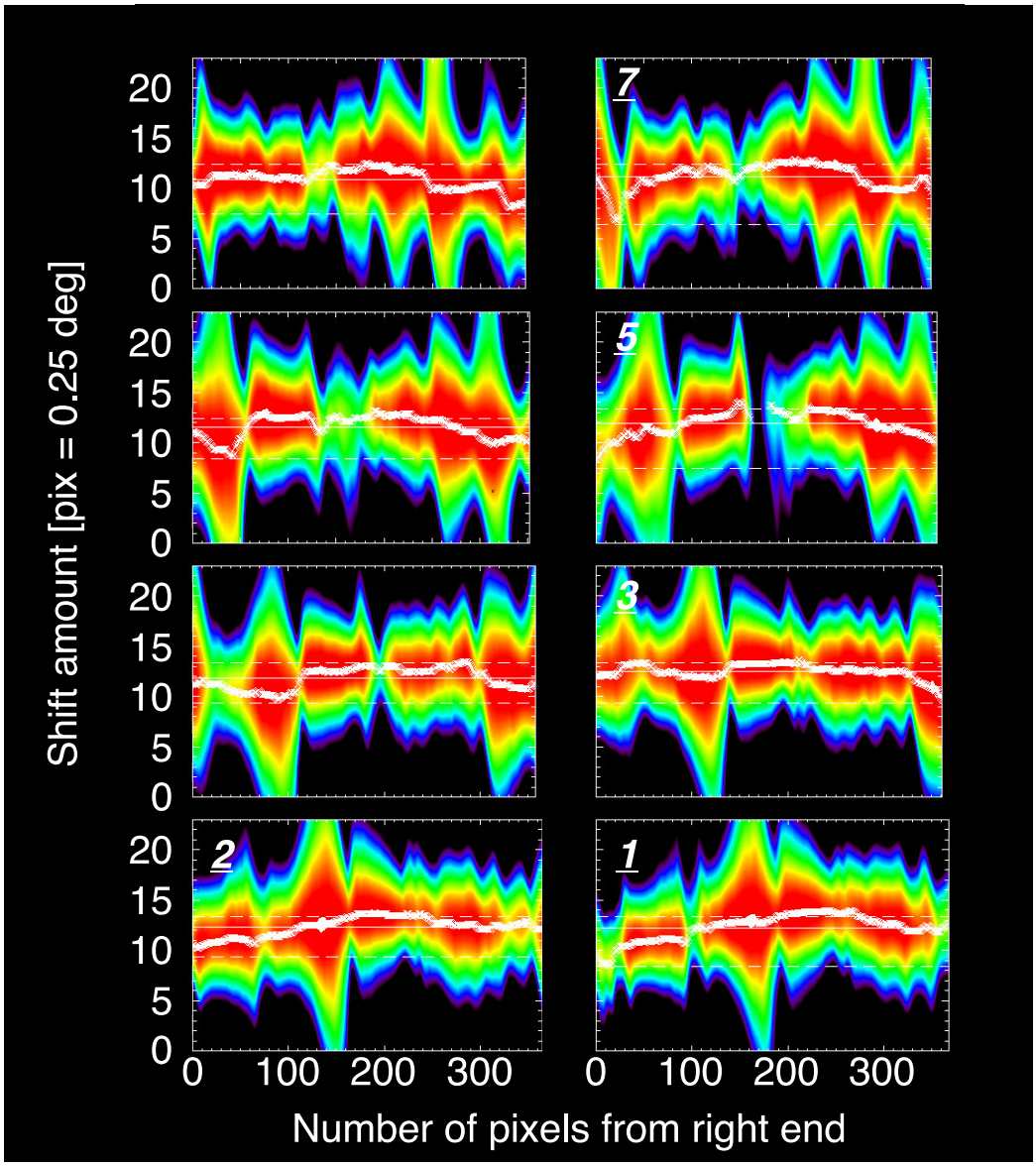

Figure 3.17: The results of the cross-correlation calculation for each image pairs 1–8. One color contour figure consists of the number of pixels of the search range A (horizontal axis) versus and that of search range B (vertical axis) of Fig. 3.16. The vertical axis were spaced by the 1/10 sub-pixel points calculated by cubic spline interpolation.

The top panel of Figure 3.18 and 3.19 shows the retrieved result of zonal winds velocity measurements. Worse estimations with errors larger than 15 m/s are eliminated in these plots. ∼5-day periodical fluctuation can be seen in the smoothed plots in both observational periods. Compared to the previously observed fluctuation of 100±20 m/s in zonal winds velocity, the averaged zonal winds velocities (bottom panel) are almost constant at ∼100 m/s in each observational period.

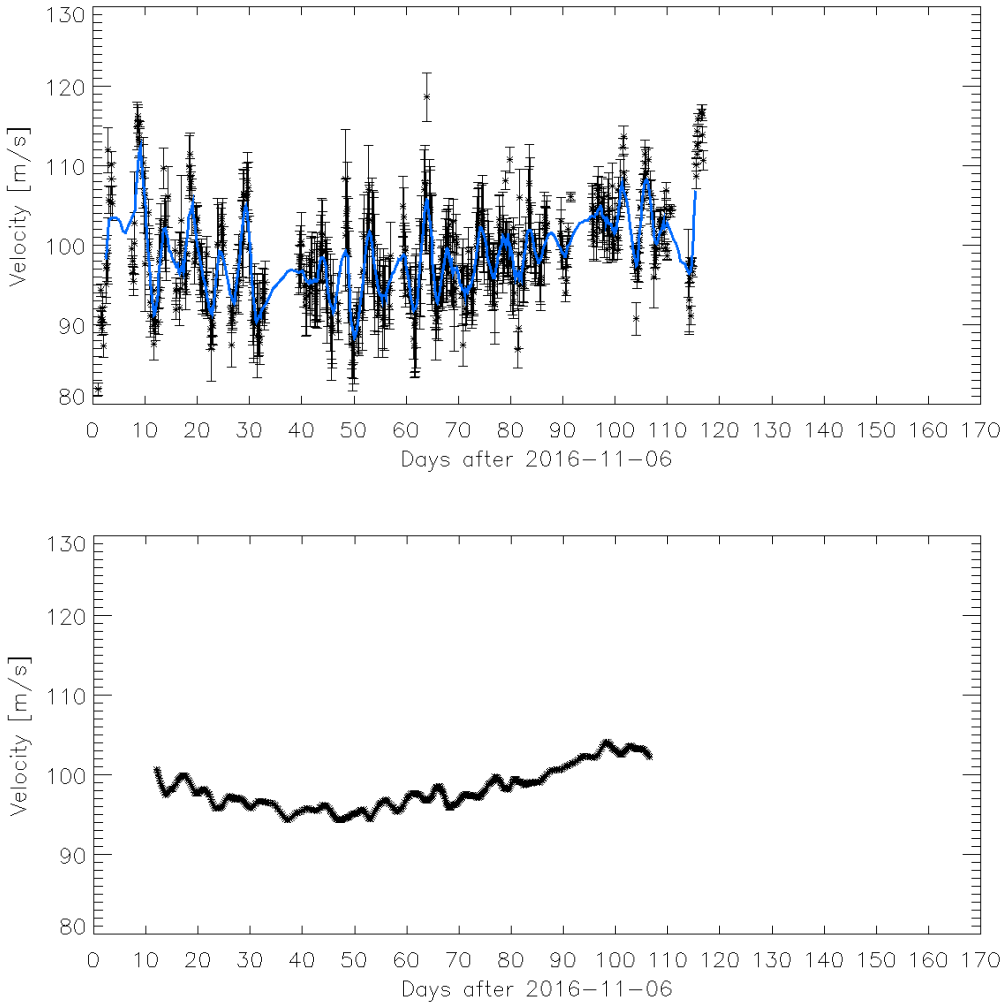

Figure 3.18: Top: Time series of measured zonal wind velocity for OP2017A. Each error bar denotes the standard deviation of the velocity in a search range A including natural phenomena of local winds shear in the range. The blue line shows the running mean proceeded data enhancing the ∼4 days fluctuation. Data values are smoothed with a boxcar average of the specified width of 10. Bottom: Longer trend of zonal smoothed with a boxcar average of the specified width of 50.

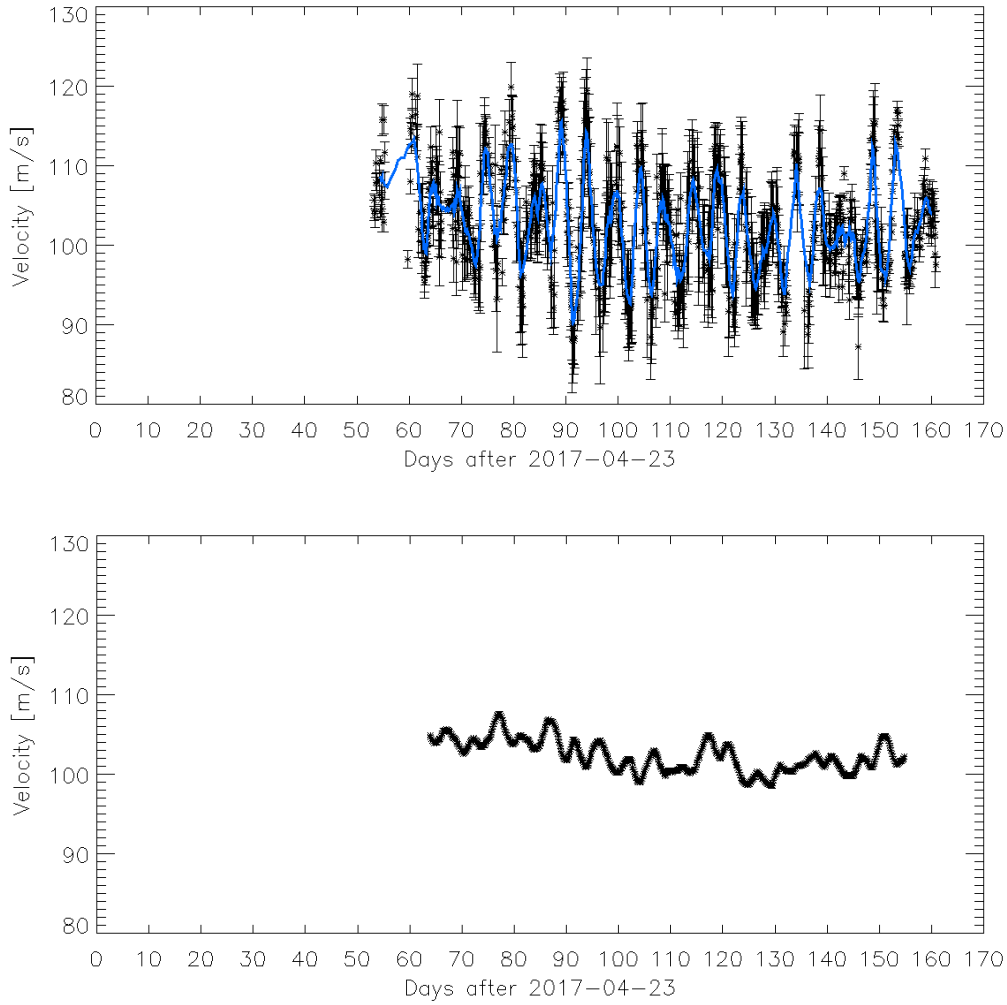

Figure 3.19: Time series of the measured zonal moving velocity of mesoscale features for OP2017B in the same manner of Figure 3.18.

4 Periodical analysis of the observed datasets

4.1 Periodical analysis with Lomb-Scargle periodogram

The periodicities in the obtained data were analyzed using the Lomb-Scargle periodogram Scargle [1982]. This analysis extracts the power spectra from unevenly sampled data, equivalent to fitting sinusoidal waves to the data by the least-squares method. The detail of the calculation of the periodogram and accompanied statistical number is described in Appendix B. Through the calculation, the periodogram, which estimates to the power spectrum, and the false alarm probability (FAP) are obtained to detect the periodical signal in the data.

The main purpose of this study is detecting the time point of the change in the periodicities in our data. We conducted the Time Shifting Lomb-Scargle periodogram analysis (called Seq. TSLS periodogram analysis) with sub-dataset in a finite time range to achieve the porposes. In this analysis, we set the time range N, and use the data $X(t)$ where $t' - N < t < t' + N$ by increasing t' by 1-day steps. When we set longer time range of sub-dataset, then analyzed data number in use for calculating periodogram is increase and allow to distinguish the spectrum peak against the noise level. However, the half of the time ranges in the start and end of the observation period are excluded in the analysis. After several attempts, we choose the time range of $N = \pm 14$ days can be appropriate to detect the periodical signal and total coverage of the observation period.

The capability of detecting the change of the periodicity is demonstrated with three test model data. These models were consisted with two types of periodical signals

having the data value of 10 ± 5 (average base value is 10, and amplitude is 5) with 3.5-day wave and 5.0-day wave periodicity, and these waves are combined as shown in the following formula,

$(Simulated\ wave) = (3.5\text{-}day\ wave) \times \mathrm{WF}_{3.5d} + (5.0\text{-}day\ wave) \times \mathrm{WF}_{5.0d}$.

Here, $WF_{3.5d}$ and $WF_{5.0d}$ mean the weighting function used to modulate the amplitude of both wave A and B respectively, and the time intervals between the data points (the sampling points of the simulated wave) of both waves were set to be $1 \pm 1.5/24$ [day], where 1.5-hour random variation was applied.

Figure 4.1 shows three weighing function (WF) for 3.5- and 5.0-day waves. Model A demonstrates the switching of the wave periodicity immediately from 3.5 days to 5.0 days at $t = 56$. Model B simulate the gradual change in the amplitude of both waves. Both waves have constant mean value of 10, and for wave A, the relative amplitude (the weighting value in Figure 4.1 $\times$ 5.0) decreases from 5.0 to 0 monotonically, where $42 \geq t \leq 70$, while the amplitude of wave B increase from 0 to 5.0 in an opposite fashion. Model C includes a monotonic increase or decrease as the Model B, but there are two waves co-existing time lasting for 28 days in the middle of the simulated time range.

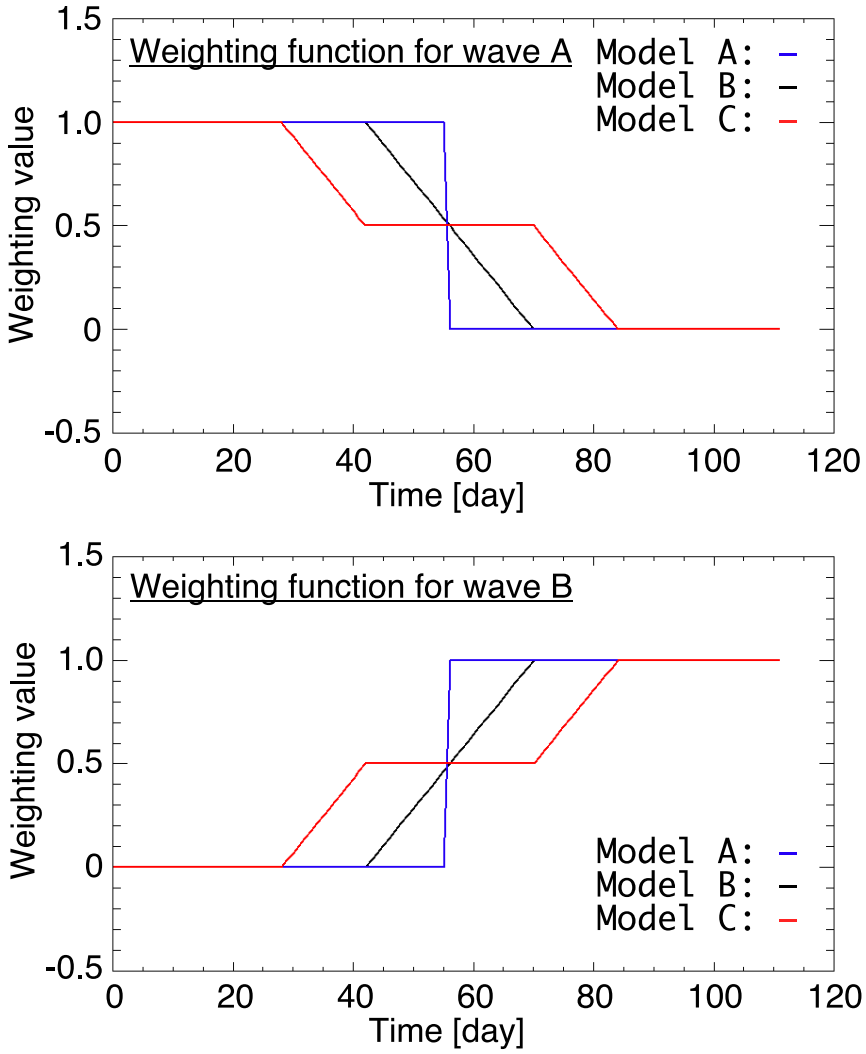

Figure 4.1: Weighting functions for demonstrating the detection of wave switching based on TSLS analysis. Time series of weighting value for 3.5-day period wave (top) and 5.0-day period wave (bottom) were prepared for Model A–C respectively.

Figure 4.2 (A–C) are the combined waves with three models respectively. Assuming the scattered data sampling, the used data points do not have even time interval of 1 day but adding the pure random fluctuation of observation time ± 1.5-hr as shown in the figures with asterisks.

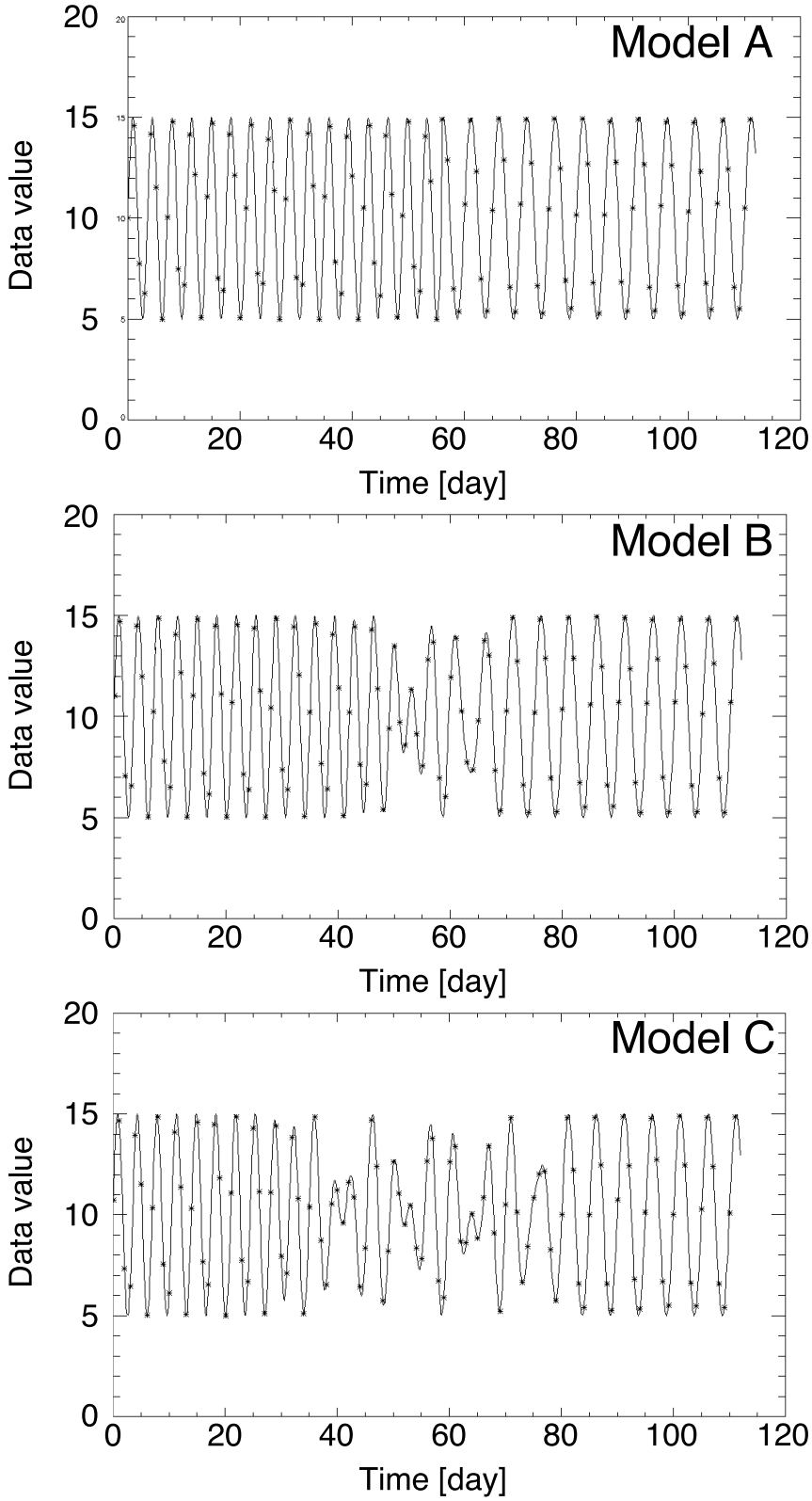

Figure 4.2: Imitation data for demonstrating the detection of wave switching based on TSLS analysis for Model A (top), Model B (middle), and Model C (bottom).

Figure 4.3 (A–C) are results of each model. The horizontal axis is the day of the period from 3.0 to 7.0, and the vertical axis is the day of the (observation) time. Since we choose the time range of sub-dataset is ± 14 days, at the start and end of 14 days is filled with the black color in the figure.. The color of contour indicates the periodogram of Lomb-Scargle analysis with linear scale and another contour with white dashed lines indicates the significance level of 90%, where the significance was calculated by 1−FAP. The difference between these three figures helps to interrupt our results in the following section. Model A shows clear disappear of 3.5-day mode and appearance of 5.0-day mode. The boundary point around $t = 56$ is obscured because of the ± 14 days time range. Therefore we should take into account for the effect of the finite time range. Comparing Model A, the periodogram of 3.5-day mode gradually decrease but it still above the significance level of 90%. In contrast, the periodogram of 5.0-day mode slowly increases from $t = 56$. Model C depicts the co-existing state approximately from $t = 44 - -70$, though the value of the periodogram relatively low. Additionally, we could notice that the determination of the absolute period has the uncertainty of ± ∼0.2 days for 3.5-day mode and ± ∼0.4 days for 5.0-day mode even if the input signal has pure periodical variation. However, it is enough to distinguish two different modes.

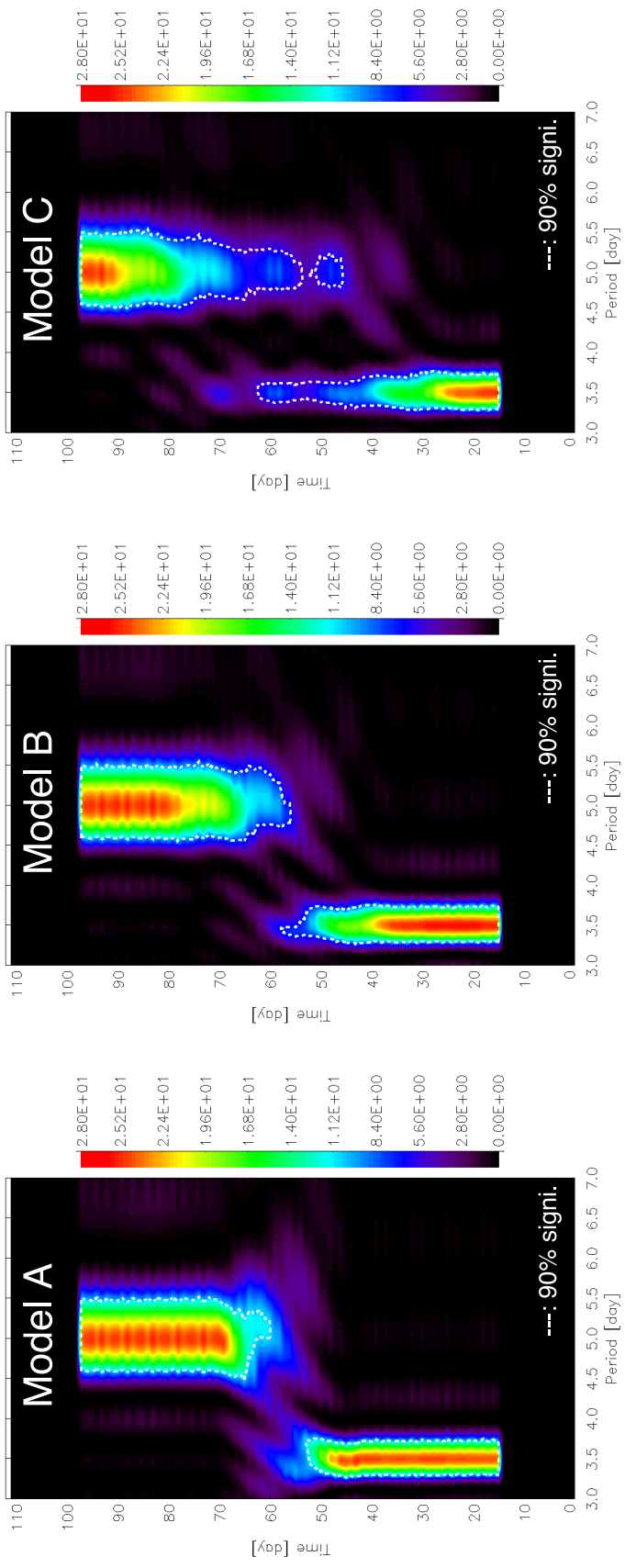

Figure 4.3: TSLS analysis results for each model. The square of displayed powers, which corresponds to estimated amplitude, were consistent with the amplitude of 5.0 in input data. These results demonstrated that the switching of waves having different periodicity could distinguish with TSLS analysis.

4.2 Periodical analysis result

In this section, the results of TSLS periodogram analysis are shown in the order of ground-based brightness data, space-based brightness data, and space-based zonal winds data. Analyzed latitudinal regions are equatorial (EQ: S10°–N10°), and north and south mid-latitudinal (SM: S50°–S30°, NM: N30°–N50°) ones. All the vertical axis are scaled in the same length from 0 to 170 days to compare with other observation periods and datasets. As shown in bottom panels of Figure 3.18 and 3.19 the measured zonal mean-winds velocity was ∼100 m/s in both observational periods. This velocity corresponds to 4.4-day circulation at the equator, and this period is helpful to know whether the measured period is shorter or longer than mean-winds rotation period. Therefore, in the following result figures, the 4.4-day period is used as the reference period as denoted with a white vertical dashed line.

4.2.1 Periodicities in brightness variation of ground-based data

Periodicities in the Pirka/MSI observation data, which measure the relative brightness variation and capture the rotation of planetary-scale features, are shown in this section. Figure 4.4–4.6 depict the result of OP2015, 2017A, 2017B respectively.

Figure 4.4 shows the result of TSLS periodogram analysis of OP2015 data for three latitudinal regions. Since AKATSUKI orbit re-insertion was conducted end of this year, there is only our ground-based data in this observation period. However, it can help to understand the repeated phenomena. As we can see in Figure 2.11 or 2.15, the amplitude of the fluctuation in the later half of the observation period was smaller than the former half. In the equatorial region (middle panel of Figure 4.4 shows the change in the periodicity around $t = 70$ (2015/6/10). After the $t = 65$, ∼3.5-day mode was never seen in all latitudinal area, in contrast, 5.2-day mode appears in northern mid-latitudinal and equatorial region.

Figure 4.5 is the same results for OP2017A. The total length of observation period is short because of the low data acquisition rate in this season, but we can find the peak period exist ∼4.7-day. During this observation period, UVI data covers more wide time range, and these results are used for the validation by comparing different datasets.

Figure 4.6 is for last ground-based observation period of OP2017B. Though the nonuniform data acquisition rate causes the scatter in the displayed color contour, over four months continuous observation enables us to know the dynamical change in the periodicity. At the start and end of this observation period shows less periodical variation, and we should note this as the same effect of OP2015. The interpretation of this is described in section XX based on the comparison between ground-based and AKATSUKI data. From $t = 25$ (2017/5/18) to $t = 80$ (2017/7/12), the 3.5-day modes can be seen in all latitudinal area, and after $t = 80$ ∼5.0-day mode become prominent relative to the 3.5-day mode. Around $t = 70$ (2017/7/2) slightly shorter period of 4.5-day mode was confirmed in several days.

Figure 4.7 is the same results of Figure 4.6, but it includes data obtained by Kanata telescopes. There is large data missing period around t=75 in the data of Pirka telescope in OP2017B because of the long spell of severe weather. However, the co-operative observation with Kanata telescope helps to compensate the data missing.

The observed characteristics in ground-based brightness data are summarized as follows,

in OP2015

· The first observed ∼3.5-day period discontinuously transit to ∼5-day.

· There is a time interval less than 20 days during the transit.

· Sporadical modes transient occurred sub-Venusian year time-scale.

in OP2017B

· 3.5-day period was dominant over the observational period in the equatorial region.

· Equatorial and south mid-latitudinal region has continuous periodicity change again.

· Double modes were observed in Equatorial and north mid-latitudinal region simultaneously.

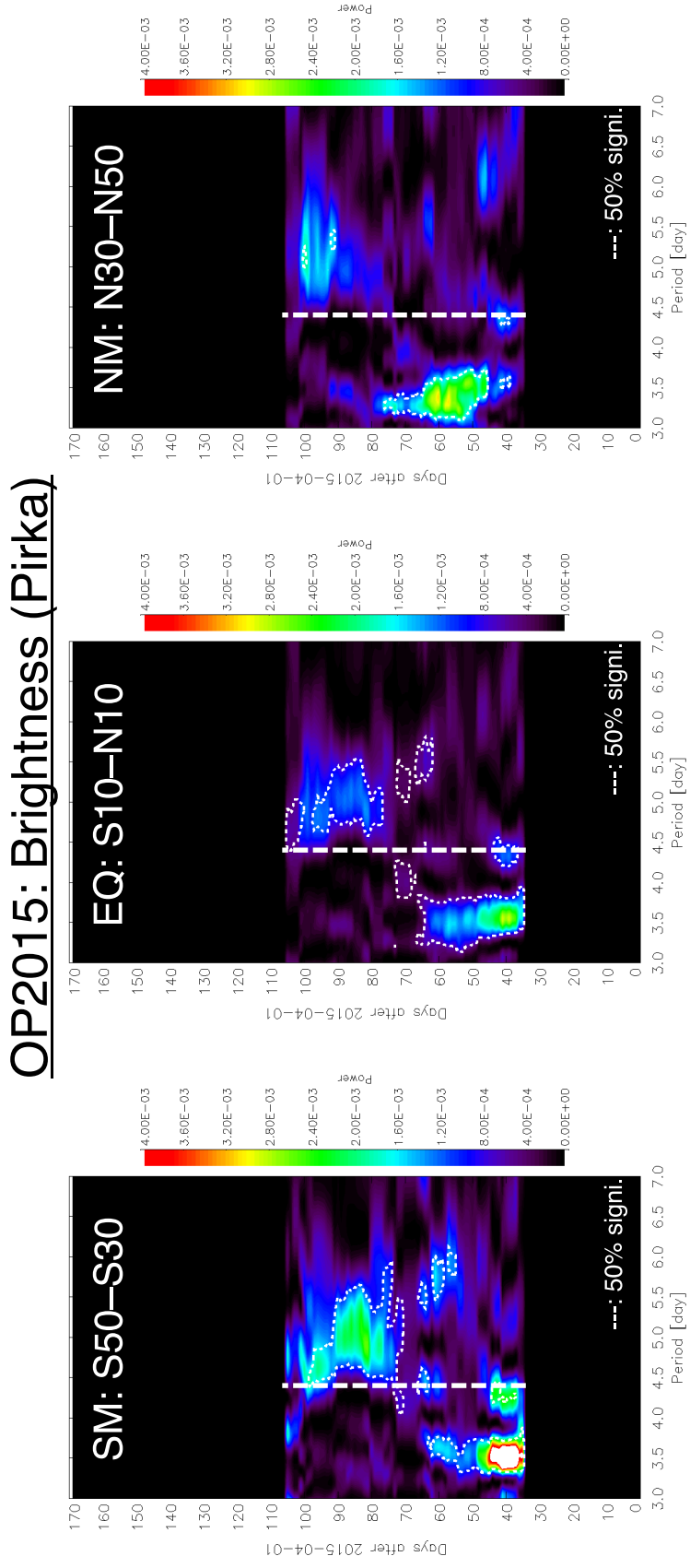

Figure 4.4: Time series of periodicities in brightness variation of OP2015 observed with ground-based telescopes. Three latitudinal regions of SM (50°S–30°S), EQ (10°S–10°N), and NM (30°N–50°N) were analyzed with TSLS analysis, and 50% significance level is depicted with the white dashed line.

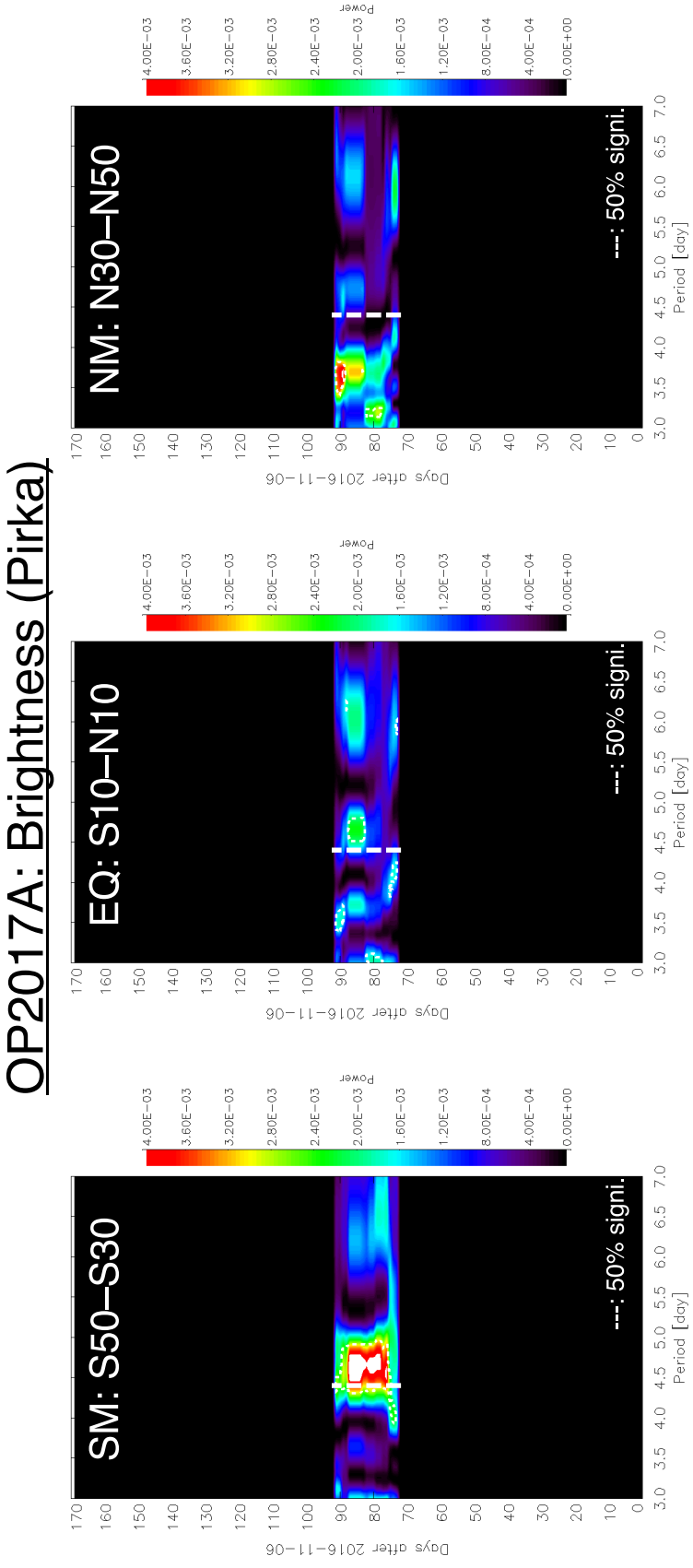

Figure 4.5: Time series of periodicities in brightness variation of OP2017A same as Figure 4.4.

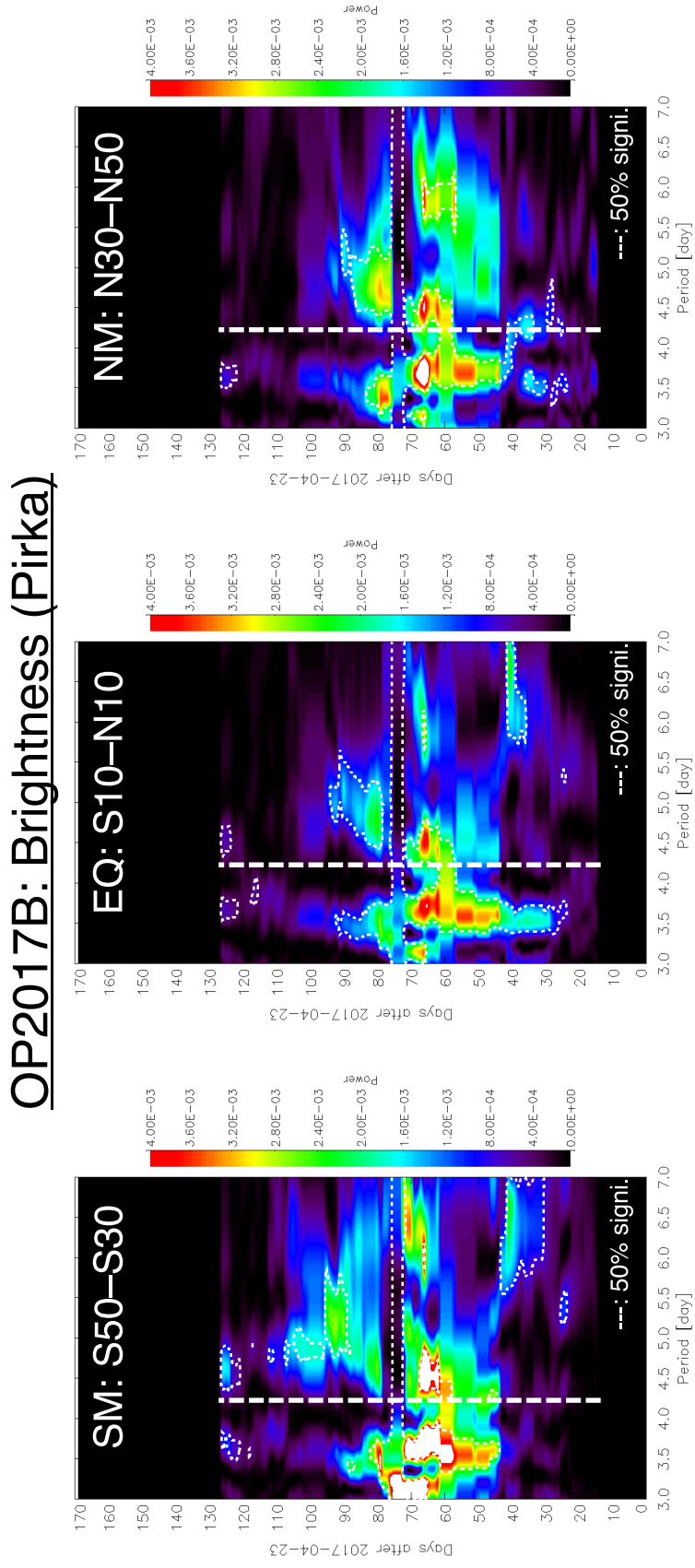

Figure 4.6: Time series of periodicities in brightness variation of OP2017B same as Figure 4.4.

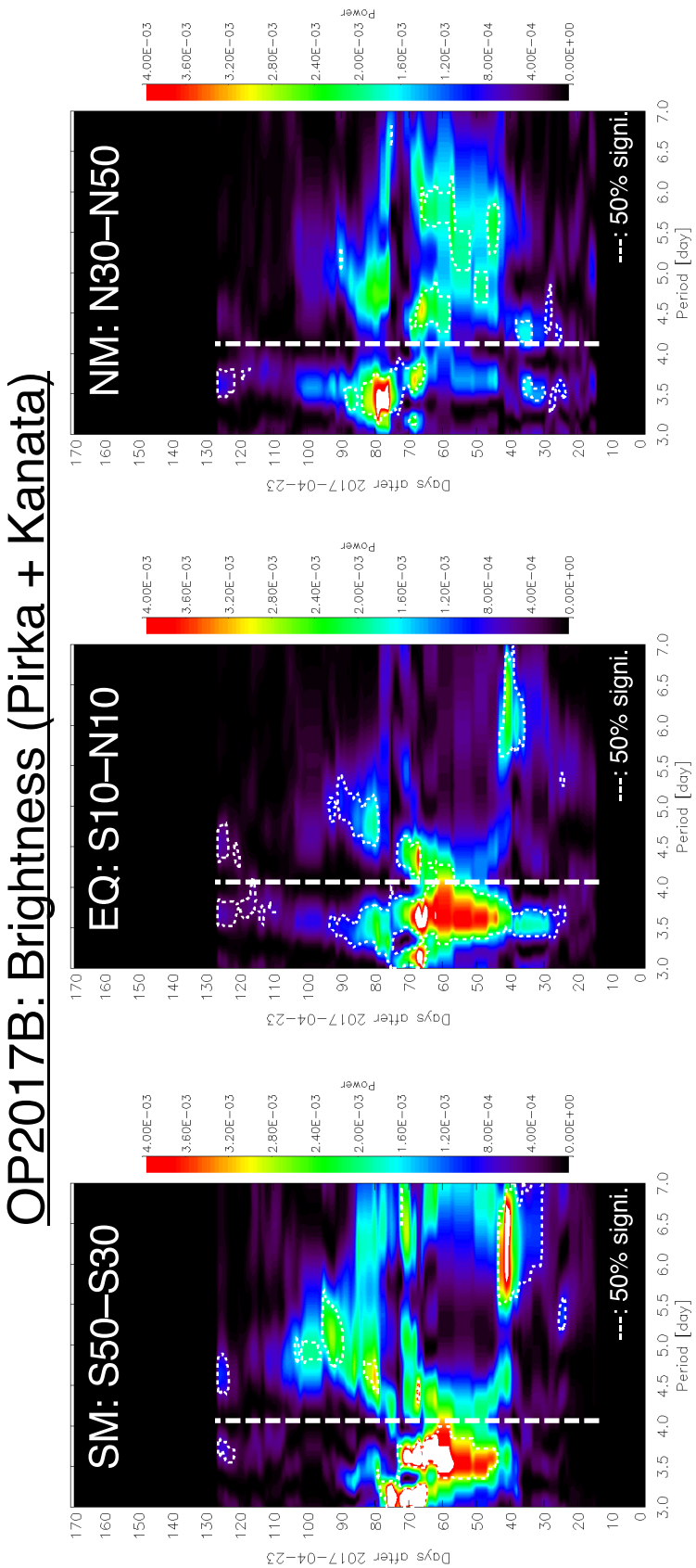

Figure 4.7: Time series of periodicities in brightness variation of OP2017B same as Figure 4.4, but including Kanata observed data.

4.2.2 Periodicities in brightness variation of space-based data

Periodicities in the AKATSUKI /UVI observation data, which measure the relative brightness variation and capture the rotation of planetary-scale features, are shown in this section. Figure 4.8 and 4.9 depict the result of OP2017A and 2017B respectively. Because of the observation limit of monitoring same local time area, we divided it into three observation period. These combined figures were made with trimming figures shown in Appendix C, where horizontal dashed lines denote the boundary dividing each sub observational periods. For determining the rotation period of planetary scale UV feature, the local time dependence is considered negligible (see Appendix C).

Figure 4.8 is the combined the results figure of OP2017A-1–A-3. The main mode in this observation period is 3.5–4.0-day mode, and in the beginning $t < 30$ (2016/12/6) 5.0-day mode co-exists. Around $t = 75$, 5.0-day mode reappears, and soon after $t = 75$ (2017/1/20), they seem combined as the 4.5-day mode. Ground-based results at the same observation time support the existence of ∼4.5-day mode at t ∼75.

For OP2017B, 3.5-day mode dominates in the equatorial region from the start date of UVI observation $t = 67$ (2017/6/29) as shown in Figure 4.9. Soon after $t = 80$ (2017/7/12), ∼5.0-day mode appeared simultaneously and this occurrence time is quite consistent with the ground-based result. The 3.5-day mode did not disappear through the observation period, and the mode might cause some asymmetric effects for northern and southern hemisphere against the equator. The observed characteristics in space-based brightness data are summarized as follows,

in OP2017A

· first 40 days has 4.0-day mode + 5.3-day mode in north (south) mid-latitudinal region.

· South mid-latitudinal region only has continuous periodicity change from 4.0 to 5.0-day.

· After day 80, ∼4.4 day + multi-mode condition was confirmed.

in OP2017B

· 3.5–4.0-day wave observed predominantly in equatorial and mid-latitudinal regions.

· After day 80, 5-day mode could be seen in mid-latitudes same as Pirka data.

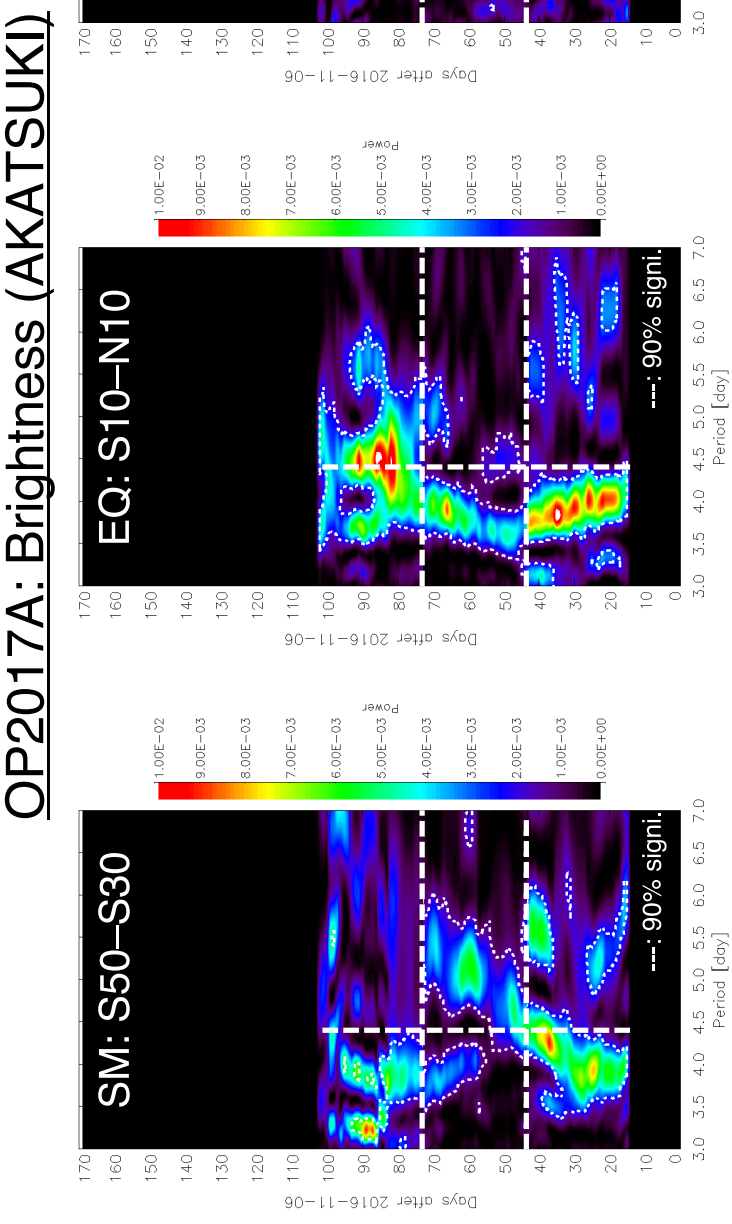

Figure 4.8: Time series of periodicities in brightness variation of OP2017A observed with AKATSUKI/UVI. Three latitudinal regions of SM (50°S–30°S), EQ (10°S–10°N), and NM (30°N–50°N) were analyzed with TSLS analysis, and 90% significance level is depicted with the white dashed line. The results of sub-observational periods of OP2017A-1, A-2, and A-3 were combined with same color scale, where horizontal dashed lines denote the boundary. The local time dependence on the periodicities are described in Appendix C, and here we neglect that dependence, and just trimming and paste the figure for the convenience.

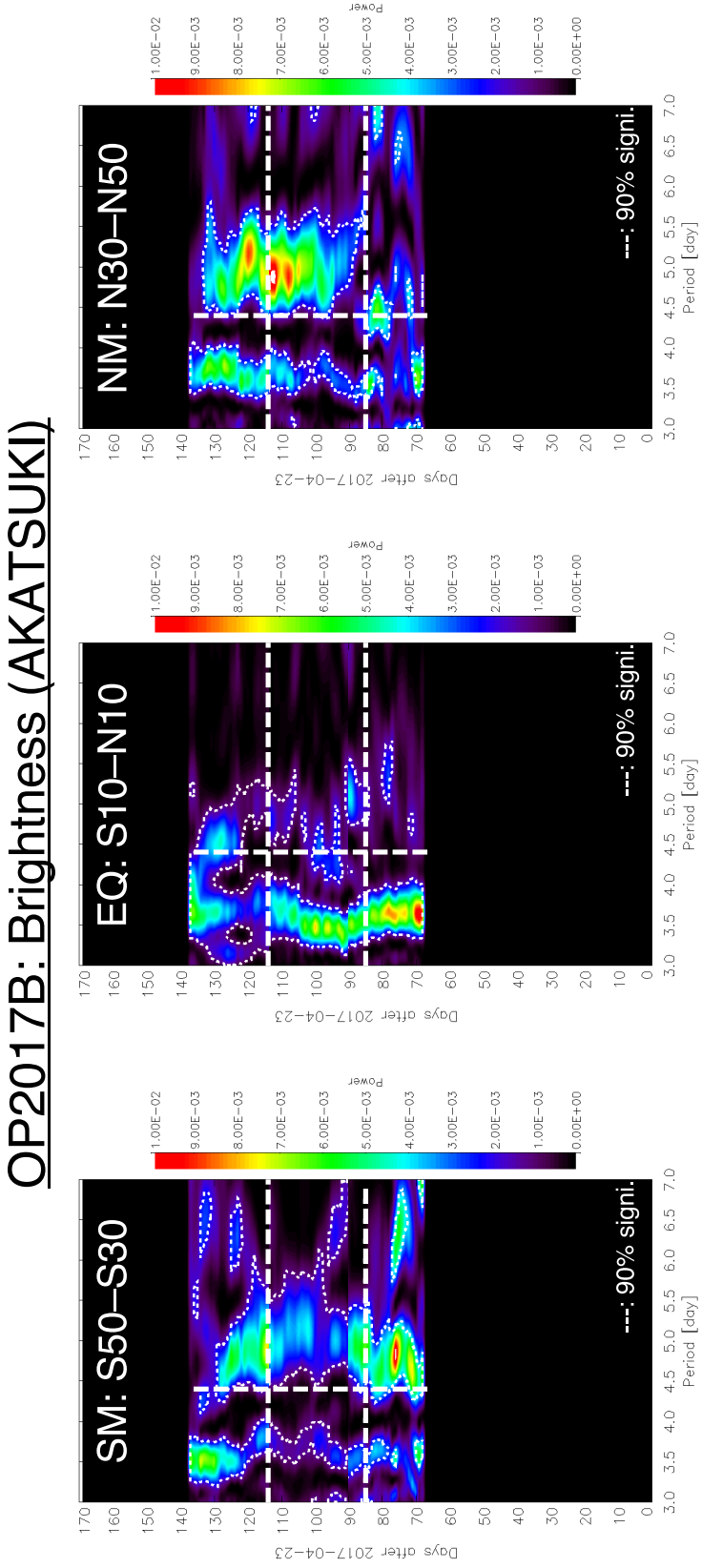

Figure 4.9: Time series of periodicities in brightness variation of OP2017B made in the same manner of Figure 4.8.

4.2.3 Periodicities in zonal winds fluctuation of space-based data

The periodicity in the zonal propagation velocity (zonal winds velocity) was studied in the final section. The periodical fluctuation in zonal winds helps to interrupt the existence of vertical wave propagation at cloud top altitude. Figure 4-9 the TSLS periodogram analysis results with 99% significance level. For OP2017A, zonal winds fluctuate with 5.0–5.5 days period, which gradually loses the amplitude, and 4.5-day fluctuation after $t = 80$ are consistent with the brightness variation. At t ∼40 (2016/12/16), three multiple periodicities of 4.0-, 4.7-, 6.0-day are also confirmed in three of all ground-based, AKATSUKI and zonal winds data. However, the zonal wind fluctuation with 5.2 days from $t = 50$ (2016/12/26) to $t = 80$ (2017/1/26) is not consistent with the brightness variation of AKATSUKI data.

For OP2017B, the single 5.0-day fluctuation is prominent in the zonal wind of equatorial region, and there is a peak of amplitude at $t = 97$ (2017/7/29). We should note that 5.0-day fluctuation is consistent with the brightness variation in the same dates. However, 3.5-day mode could not be confirmed simultaneously.

4.3 Comparison among ground and space based results

Here, we briefly summarize the validity of comparing the results between ground-based and space-based data. The observed local time from the ground and AKATSUKI were not always same, however, as already stated, the local time dependence in the periodicity of brightness variation is thought to be negligible (see also Appendix C). The mean zonal wind velocity is known to have local time dependence as studied in, e.g., Hueso et al. [2015]; Khatuntsev et al. [2013], and the velocity increases by ∼5–15 m/s from LT = 7 hr to 17 hr, accelerating towards the local afternoon. This represents a signature of the action of the solar thermal tide on the wind field. If planetary-scale UV features could be moved by the advection of background zonal winds of constant ∼100 m/s in the observational periods, then the local time dependence should be expected. However, most of observed periodicity is 3.5–4.0-day or ∼5-day modes, which indicates the features traveling faster and slower respectively, it could be interpreted that the planetary-scale features are

formed by planetary-scale waves as observed previously, and then there is less local time dependence.

We applied the same analysis methodology for measuring relative brightness from the ground- and space-based observation images. Except to the local time difference, there are no other major differences between them, and it could be concluded that the results of TSLS periodogram analysis from ground-based images are directly comparable with these from space-based images as confirmed the agreements between Figure 4.7 and Figure 4.9. Especially, the moment when ∼5-day mode appeared is consistent between them. Here, it should be noted that ground-based images suffered from blurring effects, and therefore, the measured brightness variation in each latitudinal band contained some information of next latitudinal areas. As a result, it could be hard to discuss latitudinal differences from the ground-based results. For example, it means that the observed double mode at $t = 80$ of OP2017B in equatorial region (middle panel of Figure 4.7) can be true. However, the amplitudes (power) of both modes are not directly comparable, and could not discuss which mode is dominant.

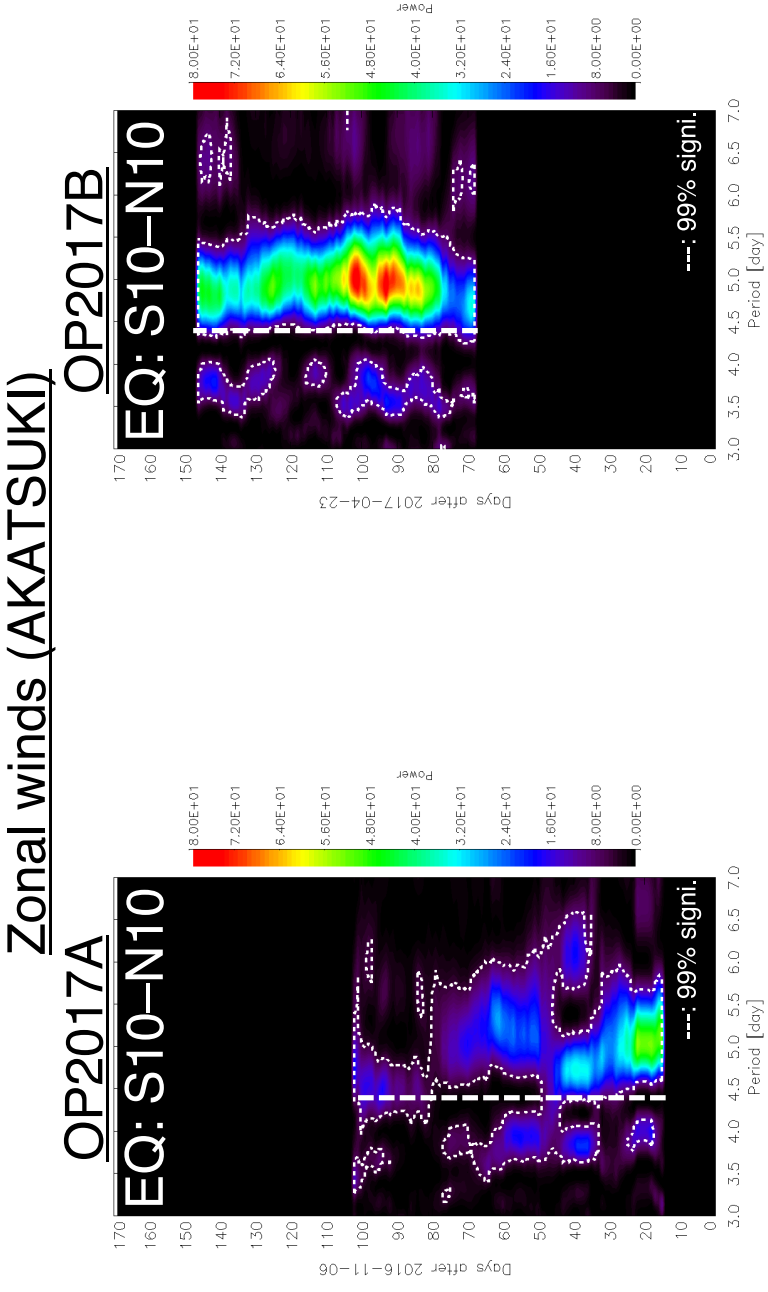

Figure 4.10: Time series of periodicities in zonal wind fluctuation of OP2017A (Left) and OP2017B (Right) observed with AKATSUKI/UVI. Equatorial regions (10°S–10°N) was analyzed with TSLS analysis, and 99% significance level is depicted with the white dashed line.

5 Periodical UV brightness variation and planetary-scale waves

5.1 Capability of ground-based observation for monitoring Venus

For monitoring Venus, both space-based and ground-based observations are important. This study develops the methodology for monitoring the rotation period of planetary-scale UV feature on Venus from the ground and realize the long-term continuous observation as long as possible. In general, space-based observation in Venus orbit, which fixed inertial frame of reference, Venus dayside observation was mainly limited in half of the Venusian year. On the other hands, ground-based observation has different time opportunity for monitoring Venus as already shown in Figure 1.1.

Figure 5.1 illustrates the observation opportunity of space-based and ground-based instruments. This configuration is the ideal case, but it can be said that the corroborative observation is very obviously important to reveal the long-term phenomenon. Figure 5.2 illustrates our actual achievement for observing Venus, and we succeed to demonstrate,

· Ground-based observation can cover more than a half of Venusian year
· Over 10.8 months (1.4 Venusian years) monitoring realized by combining ground-based and AKATSUKI data with only 1.5 months data missing this time.

The most important point of this achievement is that the obtained long-term continuous data allow investigating the transient behavior of periodicity. As shown in Figure 1.17, the transient behavior could not investigated based on the previous

limited observation data.

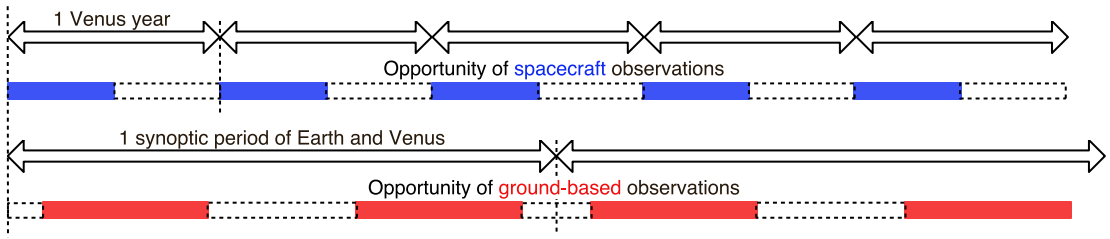

Figure 5.1: The ideal opportunities of Venus observation by using ground-based telescopes and spacecraft onboard cameras. Venus dayside is observable in half every one Venusian year as shown in the blue area, and it is visible from the ground independently as red areas.

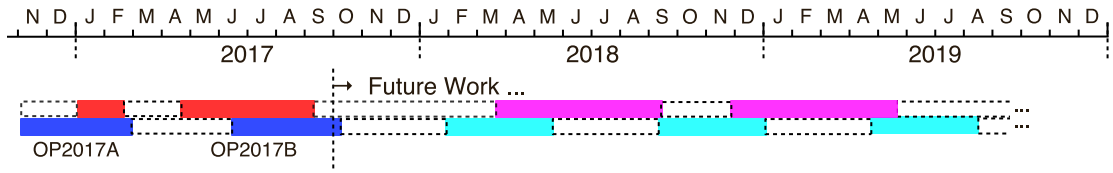

Figure 5.2: Observation periods of this study and our next future observation opportunities. From 2018 to 2019, we have observation opportunities from the ground and space alternately.

5.2 Waves observed in this study

The observed periodical UV brightness variation could be a manifestation of planetary-scale waves. Del Genio and Rossow [1990] found the difference in the period between the equatorial rotation of planetary-scale feature and that of background atmosphere (zonal winds) derived from the cloud tracking of small-scale cloud features. Since the PVO observed ∼4 days brightness variation could be interpreted as a prograde propagating and equatorial confined wave, and the accompanying meridional wind fluctuations were absent, they identified it as a Kelvin wave. The ∼5 days variation of the mid-latitude mode is considered as a symmetric Rossby wave having the meridional oscillation in the mid-latitude, the zonal oscillation in the high latitude and the equatorial region, and the retrograde propagation. The same consideration is taken as the criteria that, 1) waves propagating faster than the background wind with oscillations mainly in the zonal wind in low latitudes are Kelvin waves, and 2) waves propagating slower than the background wind with fluctuations in both

zonal and meridional winds in the mid-latitudes are Rossby waves. These criteria were used in the study of Kouyama et al. [2015] as observed periodicity in zonal winds fluctuation compared with corresponding average zonal winds velocity shown in Figure 1.15 with the white line.

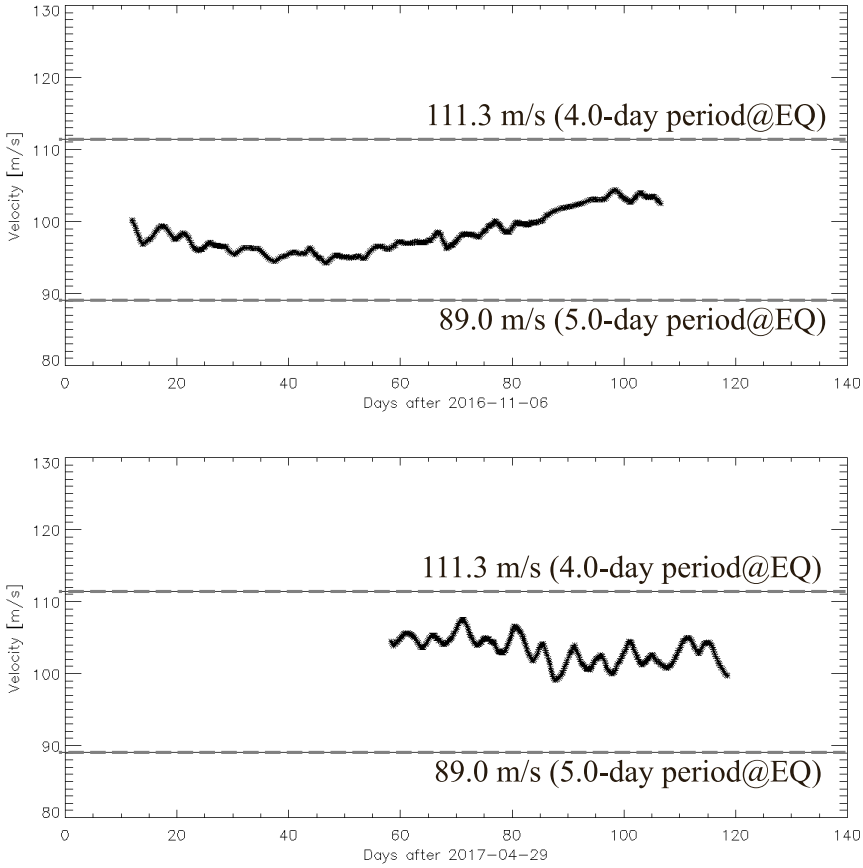

Figure 5.3: Time variation of mean zonal wind for OP2017A (top) and OP2017B (bottom) calculated as the average of obtained total zonal winds velocity with ±50 bins. Corresponds velocity of 4.0-day and 5.0-day rotating velocity at the equator also displayed in figures.

Figure 5.3, shows the mean zonal winds of OP2017A and OP2017B respectively (the same data of Figure 3.18 and 3.19). The mean zonal winds velocity slightly varied during each observation period, but it kept between the velocity of 127.2–111.3 m/s and 89.0 m/s corresponding to observed 3.5–4.0 days and ∼5.0 days wave modes. Since there are no other suggestive candidates of the prograde and retrograde propagating waves, observed 3.5–4.0 days and ∼5.0 days wave could be considered as Kelvin wave and Rossby wave respectively.

5.3 Periodicities in brightness variation and zonal wind fluctuation

Since Kelvin wave is accompanied by vertical upwelling transport of unknown absorber, which should concentrate lower cloud layer, the planetary-scale features could rotate as the same period of the Kelvin wave. This consideration is supported by the reason why the rotation period of planetary-scale features is shorter than that of zonal mean-winds. On the other hand, the horizontal vortices caused by Rossby wave can transport the absorbers in the latitudinal direction and mixes the dark equatorial band and bright polar band. So, the longer rotation period of planetary-scale features than the background flow could be explained by the existence of Rossby wave.

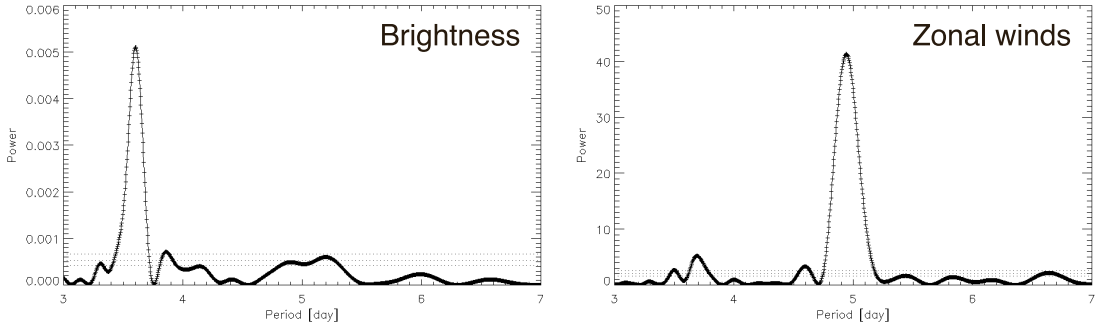

Figure 5.4: Results of the Lomb-Scargle analysis for brightness data of OP2017B-1 (Left) and the zonal wind data of OP2017B (Right). Three horizontal dashed lines represent significance levels of 99%, 90%, and 50% from upper to lower.

As described in Appendix A, planetary-scale waves shake the atmosphere and cause the fluctuation in the wind fields. Therefore, in the situation of single planetary-scale waves (Kelvin wave or Rossby wave) contributing to alter the global distribution of unknown absorber and determine wind fields, the periodicities between brightness and zonal winds should be same. However, It can be seen the difference of periodicities between brightness variation and zonal winds fluctuation in the equatorial region (10°S–10°N). This situation was prominent especially in OP2017B, and Figure 5.4 shows the periodicity observed in the brightness and zonal wind data of OP2017B. All the data point were used as a single data set without the shifting window of TSLS analysis, and the brightness data shows only ∼3.5-day variation, while the zonal winds have 5.0-day fluctuation. It should be noted that the zonal winds fluctuation has weak 3.5-day signal and is same period as the strong period

in brightness variation.

One of the possible explanation is that the composite of two different planetary-scale waves occurred in that observation period, and 5-day (Rossby) wave in mid-latitudes has a larger amplitude of fluctuating winds than that of ∼4-day (Kelvin) wave in the equatorial region. If the vertical transportation of UV absorber by Kelvin wave has stronger contribution to form planetary-scale features than latitudinal transporting by Rossby wave, this scenario can be acceptable. Since our measurements of winds velocity are limited only in zonal direction and within the equatorial region because of our simple cloud tracking methodology, it was hard to discuss whether the amplitude of observed Rossby wave is larger than that of Kelvin wave or not. Investigating the horizontal structure of winds field and the intensity of the vortices based on more advanced cloud tracking methods as already established by, e.g., Horinouchi et al. [2017] will help to deepen our discussions, and that will be our future work.

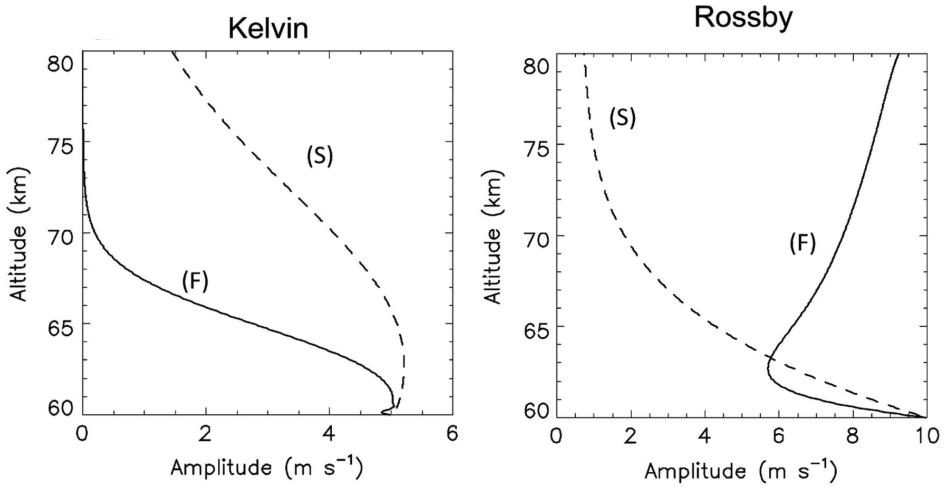

Figure 5.5: Vertical profiles of the zonal wind amplitude on the equator calculated by Kouyama et al. [2015]. (F: solid lines) and (S: dashed lines) denotes the case of background zonal winds is faster (>100 m/s) and slower (< 90 m/s) at 70 km respectively.

On the other hand, when we can make another consideration that planetary-scale features and mesoscale features exist at different altitudes, then the condition of a significant amplitude difference between two waves might be explained. Considering the situation that two layers of global cloud contrasts and patchy mesoscale clouds exist at different altitudes and observing them from the top, it might be more natural

that mesoscale clouds located higher level than that of the global contrasts. The possibility of altitude difference between different types of features was previously mentioned by Covey and Schubert [1981].

Figure 5.5 depicts the amplitudes of Kelvin and Rossby wave during their vertical propagation calculated with linearized primitive equation model by Kouyama et al. [2015]. They showed Kelvin wave is sensitive to the background zonal winds velocity, and the amplitude of Kelvin wave is easy to decay. Therefore, the observed difference of periodicities between brightness variation and zonal winds fluctuation could be explained as planetary-scale features exist lower altitudes than the altitudes where Kelvin wave dominate and the higher altitudes of mesoscale features locate (or cloud top altitudes) are considerably influenced by Rossby wave (see Figure 5.6).

Assuming the above discussion is true, it is suggested that the information of periodicities in zonal wind fluctuation could not always reflect that of planetary-scale waves at the altitude where planetary-scale features exist. It means that the representative study done by Del Genio and Rossow [1990] using the brightness data of PVO and another work by Kouyama et al. [2015] based on zonal winds data of VEX cannot directly compare. Kelvin wave was confirmed once in total ten observation epoch of VEX seems reasonable, because Kelvin waves easy to decay during the vertical propagation from the altitude where planetary-scale feature exists to that of mesoscale features do.

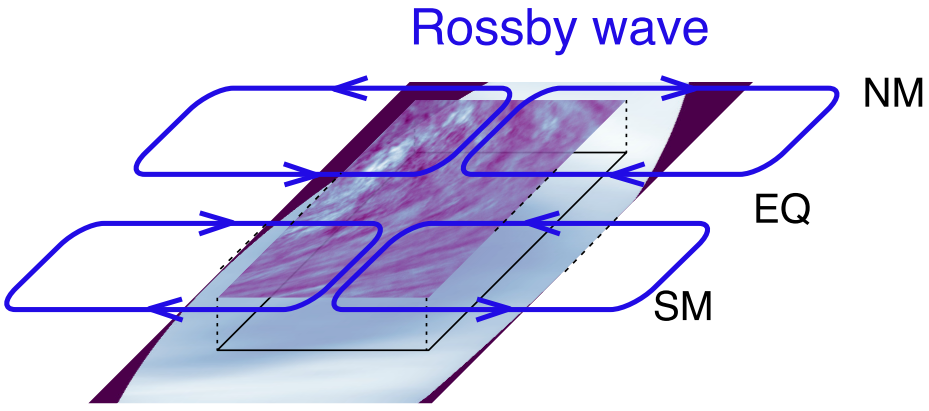

Figure 5.6: Our proposed schematic illustration explaining the observed difference of periodicities between brightness variation and zonal winds fluctuation. Mesoscale features locate higher altitudes than the planetary-scale features exits and influenced mainly by Rossby wave.

Further investigation will be done by calculating the phase difference between the brightness variation and zonal winds fluctuation. Figure 5.7 depicts the plot of brightness variation in OP2017B-1 at equatorial region (top) and zonal winds fluctuation in OP2017B at the same region (bottom). The calculated single sinusoidal curve is well fitted to brightness variation, but zonal winds fluctuation requires superposition of two modes of sinusoidal curves. Table 5.1 shows the calculated peak period ($2\pi/\omega$) and phase ($\tan^{-1}(a/b)$) at 29 April 2017, where $\tau = 0$ as following equations in Appendix B. The phase difference of 3.6-day variation in brightness and zonal wind can be estimated as $(1 - 0.59\pi)$. However, it is difficult to interpret the estimated phase difference at the current point, because (1) the measured zonal winds velocity includes local time difference, and (2) the phase relation between brightness and zonal winds are not clear. Especially, later problem requires some assumption of chemical properties of unknown UV absorber. The detail of the relation between the chemical properties of the absorber and the phase difference is described in Appendix A, and we leave the further investigation for our future work.

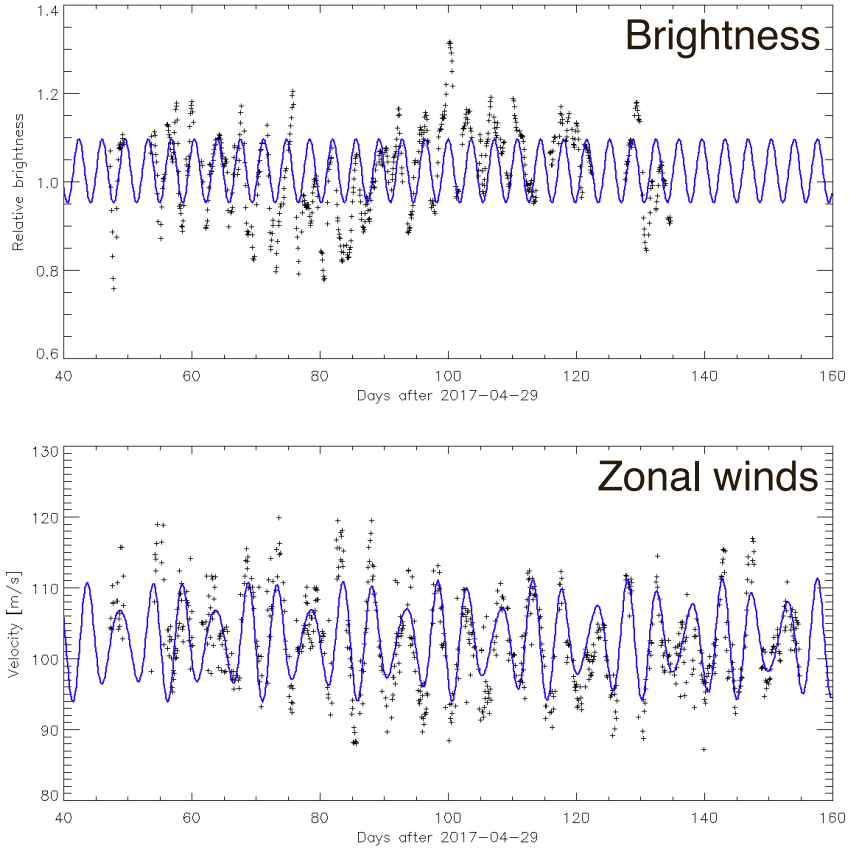

Figure 5.7: Black dots show time variations of brightness in OP2017B-1 (top) and the zonal wind in OP2017B (Right). These data were used to obtain the periodicities displayed in Figure 5.4. Blue solid lines are the fitted sinusoidal curve determined through the Lomb-Scargle periodogram analysis. The fitted curves are a single 3.6-day sinusoidal curve for brightness data and supposed 3.6- and 4.8- day sinusoidal curve for zonal wind data.

Table 5.1: Estimated peak period and phase in the brightness data of OP2017B-1 and zonal wind data of OP2017B. Phase was calculated at the time of April 29, 2017, 00:00:00 (UT).

	Peak period	Phase at τ=0
Brightness variation	3.6-day	-0.59π ($-106.2°$)
Zonal wind fluctuation	3.6-day	-0.19π ($-34.2°$)
	4.8-day	-0.12π ($-21.6°$)

5.4 Transient behavior in observed waves

Combining ground-based and AKATSUKI space-based observation, we succeeded to obtain the continuous behavior of the appearance and disappearance of planetary-scale waves in the Venus cloud top layer. The prominent wave modes were continuously monitored with 14 days time resolution (half size of the shifting window for TSLS), and it helps to renew our understanding of the waves on Venus cloud top. From November 6, 2016, to the end of September 30, 2017, two types of waves were found in this study.

First one is ∼4.0-day prograde wave (Kelvin wave) appeared most of the observational periods. Since the wave source of Kelvin wave is still unclear, it is difficult discussing whether the disappearance of the prograde wave reflects the changes in the source. However Kelvin wave is one of the free waves (one of the principal eigenmodes of the shallow water equations), and Kelvin wave is the main mode on Venus cloud top and considered to survive for a longer time.

The second one is ∼5-day retrograde wave (Rossby wave), and since this mode sporadically appeared and sometimes last > 30 days and, it might be unstable or transient waves.Sugimoto et al. [2014] investigated waves in the Venus atmosphere with their linear three-dimensional numerical model. In their work, baroclinic waves developed continuously with a life cycle of ∼25 Earth days at mid-latitudes, using available potential energy derived from a baroclinically unstable basic state. Rossby waves observed at the cloud top are generated by the baroclinic waves and spatial and temporal variation of the fast zonal winds. When the retrograde wave appeared, both of brightness variation in mid-latitudes and zonal wind fluctuation in the equatorial region have ∼5-day periodicity at the approximately same time.

During the period without any prominent waves, planetary-scale features could rotate around the planets as floating remnant with the same velocity of background zonal winds, and it was observed in brightness variation with an intermediate and broaden peak period of ∼4.5-day as observed in OP2017A.

Since zonal mean-wind velocity was almost constant of ∼100 m/s at the cloud top during the observational periods, filtering effect of zonal mean-wind at the cloud top proposed by Kouyama et al. [2015] might not be the main reason of wave transient from prograde wave to retrograde wave. But, the filtering idea should be still valid to

alter the vertical propagation of Kelvin wave. Because critical level, where the wave breakup, sensitively determined by background zonal winds velocity, and that could be one of the explanations of the appearance and disappearance of the prograde wave.

As observed in OP2015 of ground-based data, the wave transient behavior can occur as a sporadical type of change. In contrast, the continuous periodicity changes also observed as ∼4-day period gradually change to ∼5-day period, and this could be classified as a continuous type of change. In latter case, 4-day wave still survives and double wave modes could be distinguishable. It is still an open discussion, however, based on our new observational evidence, the author proposes a possible schematic view of Venus dynamical state. Namely, since Kelvin wave might be the main mode and if the wave assumed to propagate from the lower level, generation source of Kelvin wave could be a key clue to control the energy balance. And once unstable mode grows (such as baroclinic waves), then the dynamical state altered sporadically and Rossby wave generated temporary as shown in Figure 5.8.

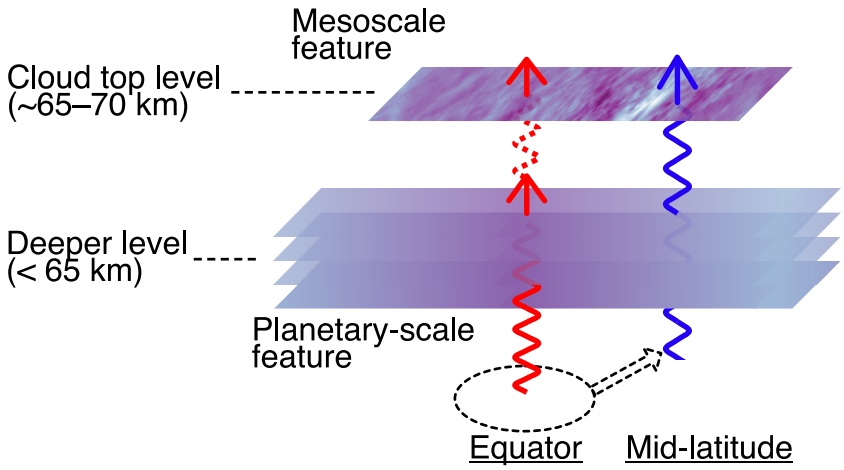

Figure 5.8: The proposed schematic view of the planetary-scale wave generation and their vertical propagation. Kelvin wave might be a primary mode and control the balance of atmospheric dynamics near the cloud top.

6 Conclusion

Long-term observation of the planetary-scale waves is essential to understand the nature of the atmospheric dynamics on planets. In this study, we succeeded to conduct Venus continuous long-term monitoring over 300 days with only 50 days data missing interval. Venus images at the 365 nm unknown absorption band was obtained from the ground- and space-based instruments. Ground-based telescopes are indispensable to achieve our long-term monitoring, and this study realized the Venus observation over the half Venusian year (> 120 days) mainly with 1.6-m Pirka telescope at 365 nm wavelength.

We newly developed the image analysis method for measuring the rotation period of planetary-scale UV feature from the ground. This method measures the distributions of the relative brightness from the equatorial to mid-latitudinal regions in both hemispheres, and we deduced the rotation periods of the UV features from the cyclical variations of these distributions. This method is critical to analyze the ground-based images suffering the effect of extinction of the Earth's atmosphere, the high variability of the sky opacity, limited observable time without daytime and variability in phase angle. Additionally, it has worth for analyzing the satellite observed image to cancel out the brightness variation caused by the different observation geometry.

The observational periods were divided into three observational periods of OP2015 (21/04/2015–07/17), OP2017A (03/01/2017–02/19), and OP2017B (23/04/2017–10/09). Venus images obtained by Ultraviolet Imager (UVI) onboard AKATSUKI were also analyzed, which covers partially the same period of the ground-based as OP2017A (2016/11/06–2017/03/02) and OP2017B (15/06/2017–31/09). It was confirmed that ground-based and spacecraft data has the consistent result and directly comparable.

Periodical analysis of the observed unevenly sampled data were conducted with Lomb-Scargle periodogram (Scargle [1982]) by using sub-dataset with ±14 days shifting window and stepped it with the 1-day interval. The continuous variability of periodicity through the observational period was captured, and most of our observational period, two prominent modes with 3.5–4.0-day and 5-day were confirmed. The 3.5–4.0-day wave were commonly observed and tended to survive for a longer time. In contrast, 5-day mode sporadically appeared and sometimes last longer than 30 days. We estimated zonal wind velocity at the cloud top by simple zonal tracking of mesoscale cloud feature, which finds the local displacements between ∼2 hour temporary separate images maximize 2D cross-correlation for each latitudinal bands with 1° width. This method tracks the zonal displacement of mesoscale cloud features maximizing 2D cross-correlation between two images separating by ∼2 hours. The estimated zonal mean-wind velocity was ∼100 m/s, which corresponds to the 4.4-day period rotation around the planet at the equator, and observed modes could be classified as faster (westward) propagating wave against mean-winds with 3.5–4.0-day period or slower (eastward) propagating wave with a 5-day period. Following the analysis of the previous study (e.g., Del Genio and Rossow [1990]; Kouyama et al. [2015]), the faster mode should be equatorial Kelvin wave, and the slower mode was considered as Rossby-wave in mid-latitudes.

Observed wave transient in this study could be classified into two types. One is complete mode transient from 3.5-day to 5.0-day with ∼20 days interval. The other one is continuous periodicity change from 3.5–4.0-day to 5.0-day where 3.5–4.0-day mode was continuing, and double-mode were observed at the moment. Since the zonal mean-wind during the observational periods were almost constant of ∼100 m/s at the cloud top filtering of zonal mean-wind proposed by Kouyama et al. [2015] might not work near the cloud top. It was also found that the periodicities in the fluctuation of equatorial zonal winds were different from that in the brightness variation in the equatorial region. One of our interpretation is that these difference caused the altitude difference between planetary-scale and mesoscale features. The source of waves and mechanisms of transient still unclear, however, our observations suggest the process of the vertical propagation of the wave is important. This fact possibly indicates the energy flow from shorter to longer period wave occurs at lower altitudes.

Appendix

A: Kelvin wave and Rossby wave

The planetary scale-waves Kelvin wave and Rossby wave has been detected by Del Genio and Rossow [1990] in the Venusian atmosphere. Both waves have zonal wave number 1, and one of the possible sources of these waves is baroclinic instability in the middle cloud region at 50–60 km altitudes. For studying these waves numerically, following equations of the horizontal momentum, the thermodynamic energy, the continuity, and the hydrodynamic are solved in a nonlinear primitive equation model of Imamura [2006].

$$\begin{aligned}
\frac{\partial u}{\partial t} &= -\frac{1}{a\cos\phi}\frac{\partial u^2}{\partial \lambda} - \frac{1}{a\cos\phi}\frac{\partial (uv\cos\phi)}{\partial \phi} - \frac{\partial(\dot{\sigma}u)}{\partial \sigma} \\
&\quad + \left(f + \frac{u\tan\phi}{a}\right)v - \frac{1}{a\cos\phi}\frac{\partial \Phi}{\partial \lambda} + X, \\
\frac{\partial v}{\partial t} &= -\frac{1}{a\cos\phi}\frac{\partial (vu)}{\partial \lambda} - \frac{1}{a\cos\phi}\frac{\partial (v^2\cos\phi)}{\partial \phi} - \frac{\partial(\dot{\sigma}v)}{\partial \sigma} \\
&\quad - \left(f + \frac{u\tan\phi}{a}\right)u - \frac{1}{a}\frac{\partial \Phi}{\partial \phi} + Y,
\end{aligned}$$

$$\begin{aligned}
\frac{\partial T}{\partial t} &= -\frac{1}{a\cos\phi}\frac{\partial (uT)}{\partial \lambda} - \frac{1}{a\cos\phi}\frac{\partial (vT\cos\phi)}{\partial \phi} - \sigma^{\kappa}\frac{\partial(\dot{\sigma}\theta)}{\partial \sigma} \\
&\quad + \sigma^{\kappa}Q, \\
&\quad \frac{1}{a\cos\phi}\frac{\partial u}{\partial \lambda} + \frac{1}{a\cos\phi}\frac{\partial (v\cos\phi)}{\partial \phi} + \frac{\partial \dot{\sigma}}{\partial \sigma} = 0, \\
\text{and} \quad & \frac{\partial \Phi}{\partial \sigma} + \frac{p_s}{\rho} = 0,
\end{aligned}$$

where, ϕ is the latitude; a is the planetary radius; u, v is the zonal and meridional winds velocity; f, β is the Coriolis parameter at the equator and that of meridional derivative; $\sigma \equiv p/p_s$ is the vertical coordinate, and p is the pressure and p_s is the lower reference pressure; $\dot{\sigma} \equiv d\sigma/dt$ is the vertical velocity in the σ coordinate; λ is the longitude; Φ is the geopotential; T is the temperature; X and Y are eddy viscosities, and mechanical damping; and Q includes eddy diffusivity, Newtonian cooling and thermal dumping.

The details of the model is skipped here, but, when the lower boundary condition is given by

$$\frac{\partial u'}{\partial \sigma} = \frac{\partial v'}{\partial \sigma} = \frac{\partial T'}{\partial \sigma} = 0, \qquad \text{and}$$

$$\Phi' = \hat{\Phi} \exp\left(-\frac{y^2}{2l_E^2}\right) \qquad \text{for Kelvin wave,}$$

$$\Phi' = \hat{\Phi}\left[\frac{\omega^*}{\beta\lambda^2 k}\left(1 - \frac{y^2}{l_E^2}\right) - \frac{y^2}{l_E^2}\right] \exp\left(-\frac{y^2}{2l_E^2}\right) \qquad \text{for Rossby wave,}$$

then the horizontal structures of the waves at 65 km cloud top level could be calculated. Here, $\omega^* = \omega - k\bar{u}$ is intrinsic frequency, k, m is zonal and vertical wavenumber (=1) and $\bar{u}$ is zonal mean wind velocity, and $l_E^2 \equiv N/\beta(m^2 + 1/4H^2)^{1/2}$ is equatorial deformation radius, which represents the latitudinal scale of an equatorially trapped wave (H is the basic scale height).

Figure A.1 shows the results of horizontal structure of Kelvin and Rossby wave, in the case of assuming rigid-body rotation at each altitude and identical to the nominal wind profile at the equator (see Fig. 4(a) of Imamura [2006]). These results show the representative structure of both waves on Venus.

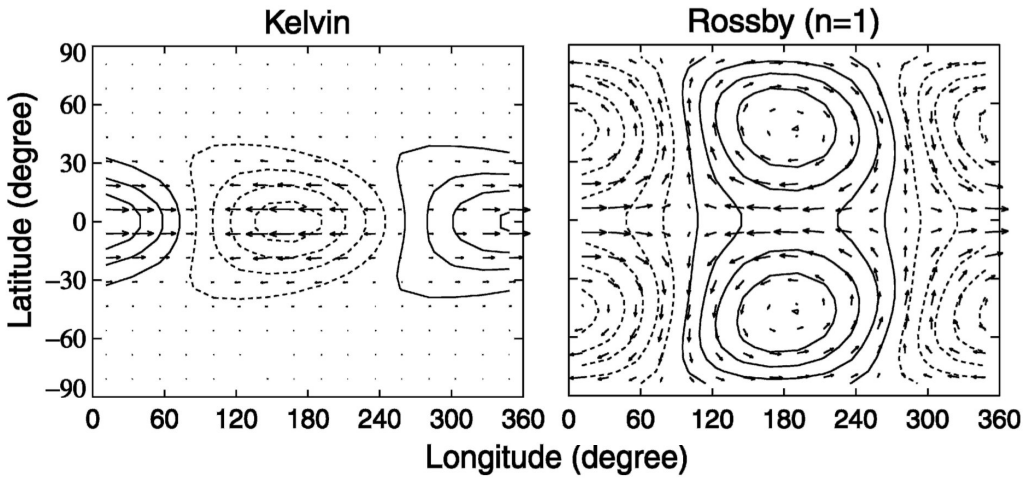

Figure A.1: Horizontal structures of Kelvin and Rossby wave at 65 km altitude in the nonlinear primitive equation model of Imamura [2006] (modified from his Fig. 6). Contours represent the disturbance geopotential with solid (dashed) contours for positive (negative) values and the contour intervals of 40, and 120 m^2/s^2 for Kelvin, and Rossby waves, respectively. Arrows represent the disturbance in the horizontal wind, which is scaled so that the distance occupied by 10° represents 3.1, 2.8 m/s for the respective waves. The direction of planetary rotation is from left to right.

Kelvin wave is the equatorially trapped wave with the latitudinal decay scale of $\theta_{\mathrm{e-fold}} = 27^\circ \pm 4^\circ$ estimated by Kouyama et al. [2012] and accompanied by winds fluctuation in zonal direction and vertically upward and downward flow as shown in Figure A.2. It was suggested that the unknown UV absorber is abundant in he lower cloud layer. Therefore, Kelvin wave is considered to form the global scale bright and dark pattern. However, It should be noted that the phase relationship between the brightness and zonal winds (or vertical wind) velocity is not clear. The reason is that the photochemical propertie of unknown UV absorber is not understood, and we can consider two possible cases.

Case 1 assumes the absorber is stable and having longer lifetime against the wave propagation period, and in this case, the darkest region should be shifted by $1/2\pi$ (90°) from the maximum point of westward zonal wind velocity or vertical upward wind as depicted in the upper panel of Figure A.1. On the other hand, Case 2 suppose the absorber is unstable and easy to photodissociate, then the darkest point and the maximum point of zonal winds should be same (in phase) like the downer panel of the figure.

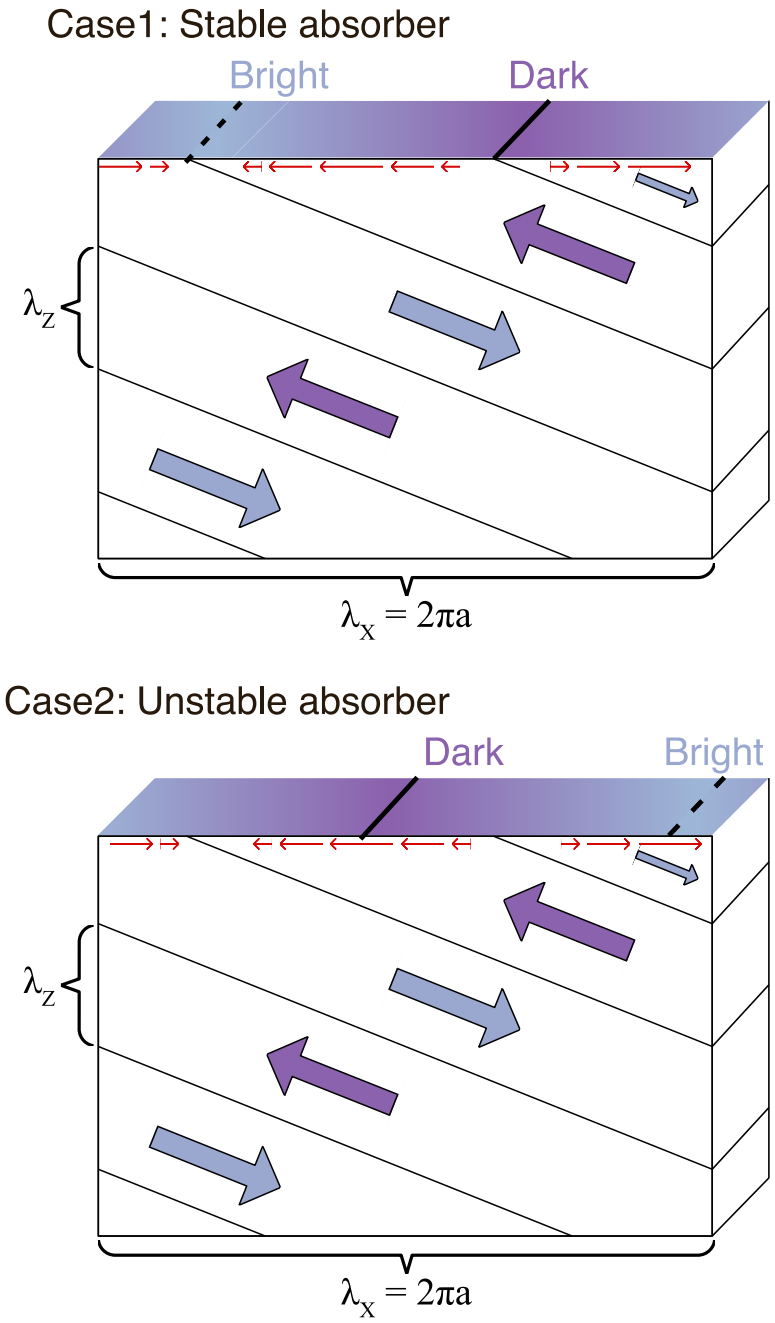

Figure A.2: Schematic illustrations showing the possible relation of transportation of unknown UV absorber by Kelvin wave and global brightness pattern in the longitude–altitude plane. Large arrows indicate the wind direction, and small red arrows denote the corresponding horizontal winds perturbations. The top figure shows "out phase" relation between zonal wind fluctuation and brightness variation if the absorber is stable (not easily decompose). The bottom figure indicates "in phase" relation between zonal wind fluctuation and brightness variation if the absorber is unstable.

Rossby wave has horizontal vortices type of winds field accompanied by zonal and meridional flow as shown in the right panel of Figure A.1. Since the winds fiels ranging from the equatorial to polar region Rossby wave could be confirmed by the horizontal wind fields measurements. Del Genio and Rossow [1990] observed this wave as the retrograde wave of 5.0–6.0 day period in 40°–60° latitudes in both hemispheres.

B: Lomb-Scargle periodgram analysis

The Lomb-Scargle periodogram is a well-known algorithm for detecting periodical signals in unevenly-sampled time-series data. This periodogram is categorized as the methodology that is equivalent to the Least Squares Methods involve fitting a model to the data at each candidate frequency and selecting the frequency which maximizes the likelihood. Lomb-Scargle method calculates the spectral power P at an angular frequency ω from evenly or non-evenly spaced data points $X_j = X(t_j), j = 1, ..., N$ as (Scargle, 1982).

$$P(\omega) = \frac{1}{2}\left\{ \frac{\left[\sum_j X_j \cos\omega(t_j - \tau)\right]^2}{\sum_j \cos^2\omega(t_j - \tau)} + \frac{\left[\sum_j X_j \sin\omega(t_j - \tau)\right]^2}{\sum_j \sin^2\omega(t_j - \tau)} \right\}$$

Here X is subtracted values by its arithmetic average $(1/N \cdot \sum X_i)$, and t_j is time. τ is defined by the relation

$$\tan(2\omega\tau) = \frac{\sum_j \sin 2\omega t_j}{\sum_j \cos 2\omega t_j}.$$

This procedure is equivalent to a linear least-squares fitting of the function

$$X(t) = a\cos\{\omega(t - \tau)\} + b\sin\{\omega(t - \tau)\}$$

to the analyzed data (Scargle, 1982), where a and b are obtained by equations below respectively.

$$a = \frac{\sum_j X_j \cos\omega(t_j - \tau)}{\left\{\sum_j \cos^2\omega(t_j - \tau)\right\}^{1/2}}$$

$$b = \frac{\sum_j X_j \sin\omega(t_j - \tau)}{\sum_j \sin^2\omega(t_j - \tau)\}^{1/2}}$$

Then, the amplitude A is obtained by the following equation.

$$A = \sqrt{a^2 + b^2},$$

and the phase at $t = 0$ is calculated by

$$X(t) = A\sin\left\{\omega(t - \tau) + \tan^{-1}\left(\frac{a}{b}\right)\right\}.$$

In this analysis, since the power at a given frequency is exponentially distributes, we can have the probability distribution as,

$$p_Z(z)dz = \Pr(z < Z < z + dz) = \exp(-z)dz,$$

where $Z = P_X(\omega)$. When we assume the noise variance well be taken to be unity, then the cumulative distribution function is

$$\begin{aligned} F_Z(z) = Pr\{Z < z\} &= \int_0^z p_Z(z')dz' \\ &= 1 - \exp(-z) \end{aligned}$$

Here, the useful quantity of $\Pr\{Z > z\} = \exp(-z)$, which gives the statistical significance of a large observation power at a preselected frequency is obtained, and it means as the observed power becomes larger, it becomes exponentially unlikely that such a power level can be due to a chance noise fluctuation. Based on this idea, and introducing the empirically generated value of $N_i = -6.362 + 1.193N_0 + 0.00098N_0^2$ (number of independent frequencies) instead of N_0 (number of data points) from Horne and Baliunas [1986], and then, the False Alarm Probability (FAP) can be calculated as below.

$$\text{FAP} = 1 - [1 - \exp -z]^{N_i}$$

This FAP tells us the probability that a peak of height z or higher will occur, assuming that the data are pure noise, and consequently, the quantity of 1 - FAP is the probability that the data contain a signal. In this paper, we convert that value into the percentage and call as the significance level.

C: Local time difference in the periodicities of brightness variation

Since the angular velocity of AKATSUKI spacecraft becomes slow near the apocentre, it is the best opportunity for taking the global viewing image of Venus disc continuously. However, as shown in Figure 3.1, the sub-spacecraft local time at the apocenter is gradually change from evening side to morning side. That means it is hard to observe a same local time region for a long time.

In this study, we have divided each observational period (OP2017A, OP2017B) into three as the local time region of 9–11 hr, 11–13 hr, and 13–15 hr are observable. The TSLS periodogram analysis was conducted for all of these sub observational periods, and the results are shown in Figure C.3–C.8 with the same color bar scale.

By comparing results of different local time region, it can be easily found that the retrieved periodicities are quite similar between the sub observational periods. Therefore, the moving velocity of planetary-scale features is not significantly changed during one rotation around the planet, and it can be concluded that the local time dependence of the periodicity in brightness variation is negligible. This conclusion is also important for comparing the periodicity measured by ground-based and space-based observation. In the main text of this thesis, the figures of each three sub observational periods were combined, and the boundary is denoted with white dashed lines.

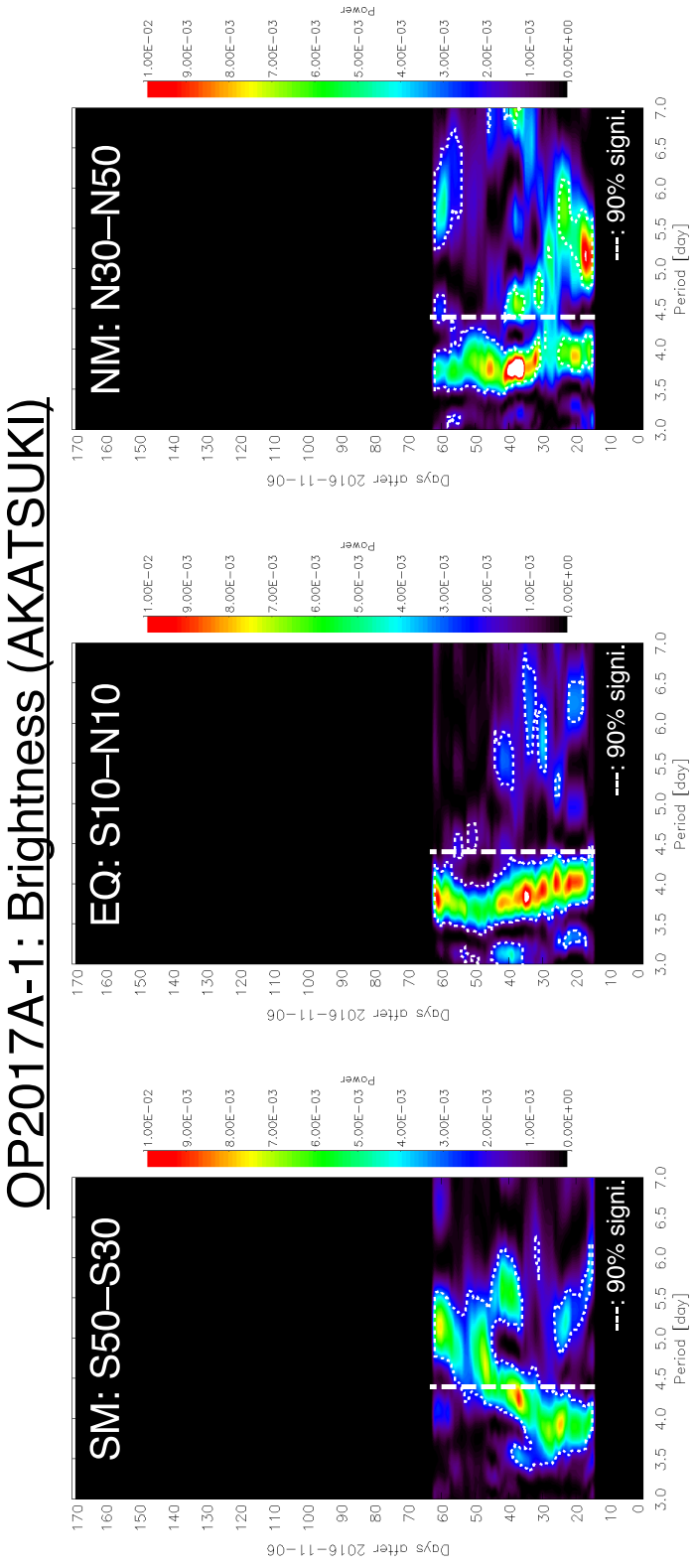

Figure C.3: Time series of periodicities in brightness variation of OP2017A-1 observed with AKATSUKI/UVI. Three latitudinal regions of SM (50°S–30°S), EQ (10°S–10°N), and NM (30°N–50°N) were analyzed with TSLS analysis, and 90% significance level is depicted with the white dashed line.

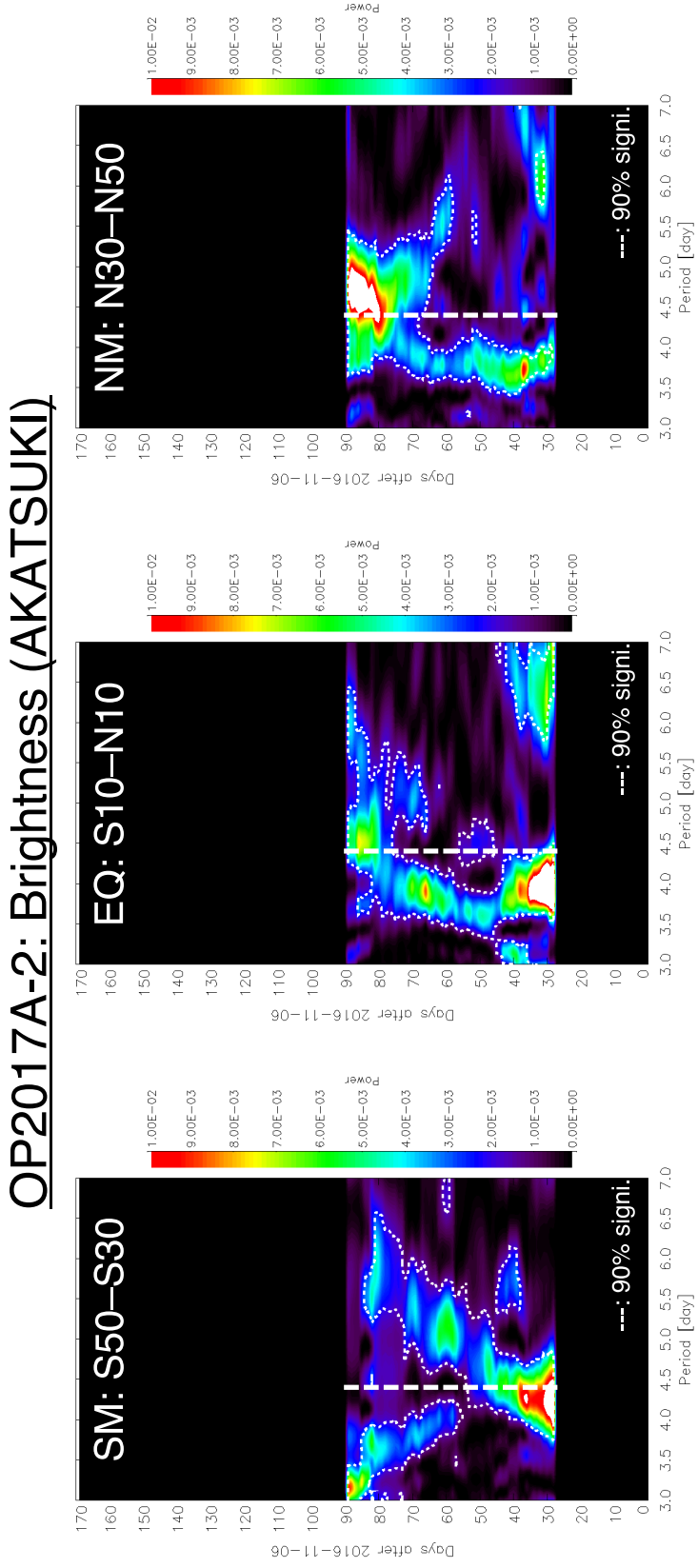

Figure C.4: Time series of periodicities in brightness variation of OP2017A-2 same as Figure C.3.

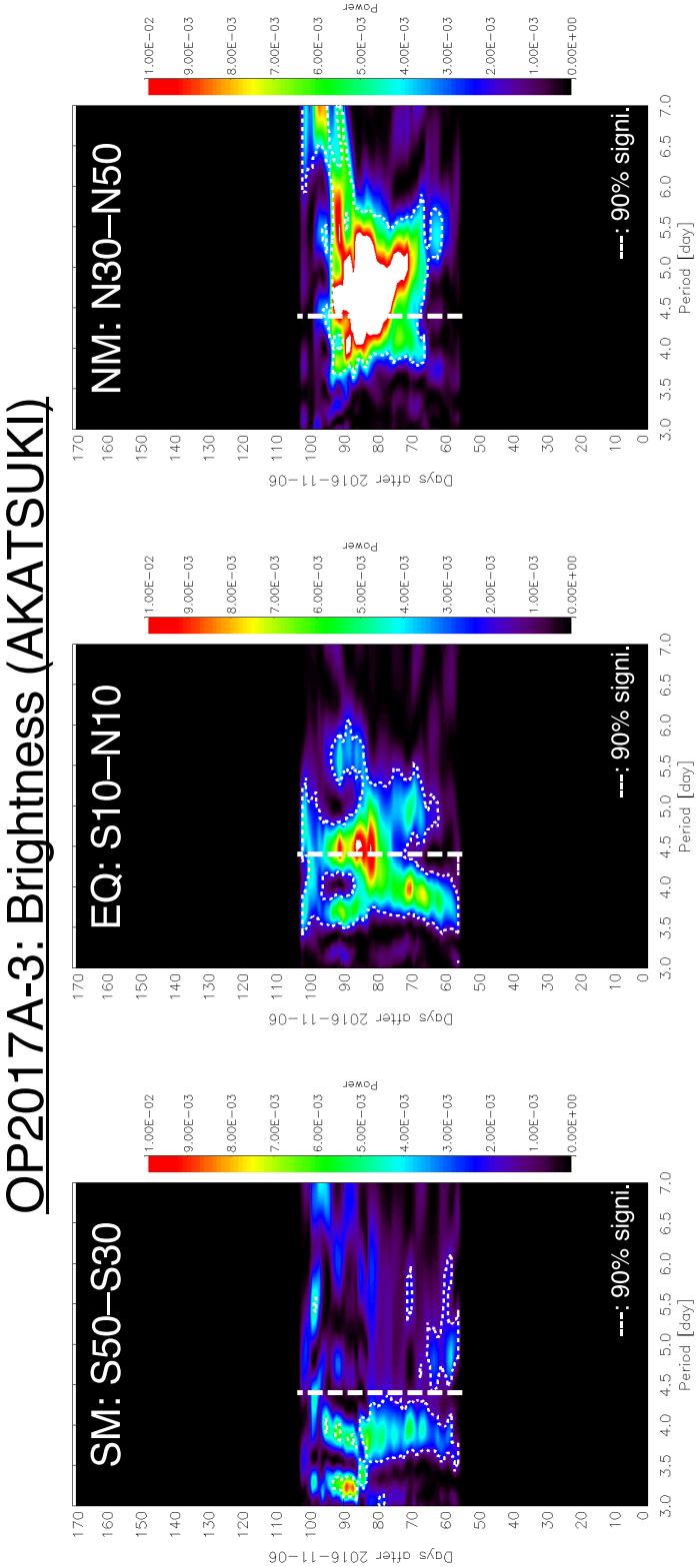

Figure C.5: Time series of periodicities in brightness variation of OP2017A-3 same as Figure C.3.

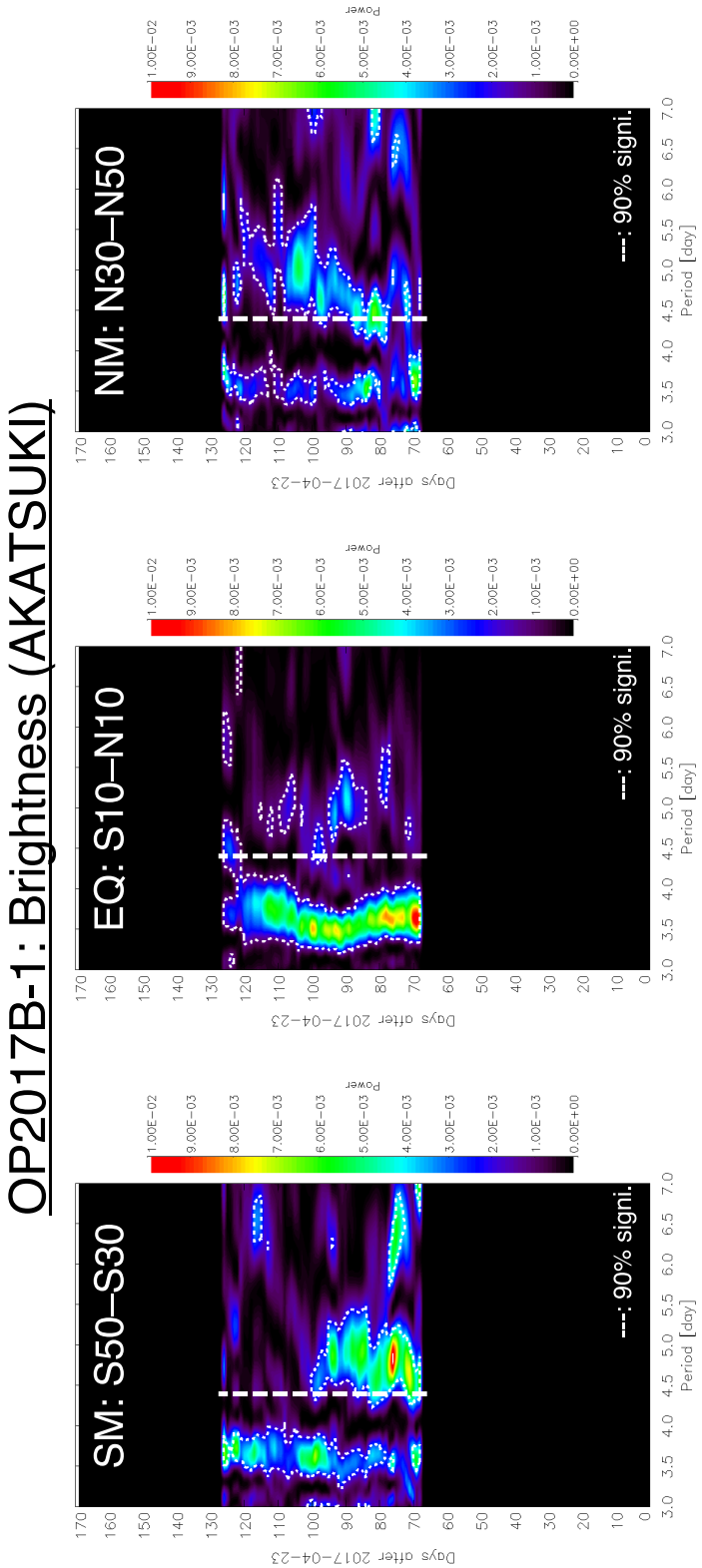

Figure C.6: Time series of periodicities in brightness variation of OP2017B-1 same as Figure C.3.

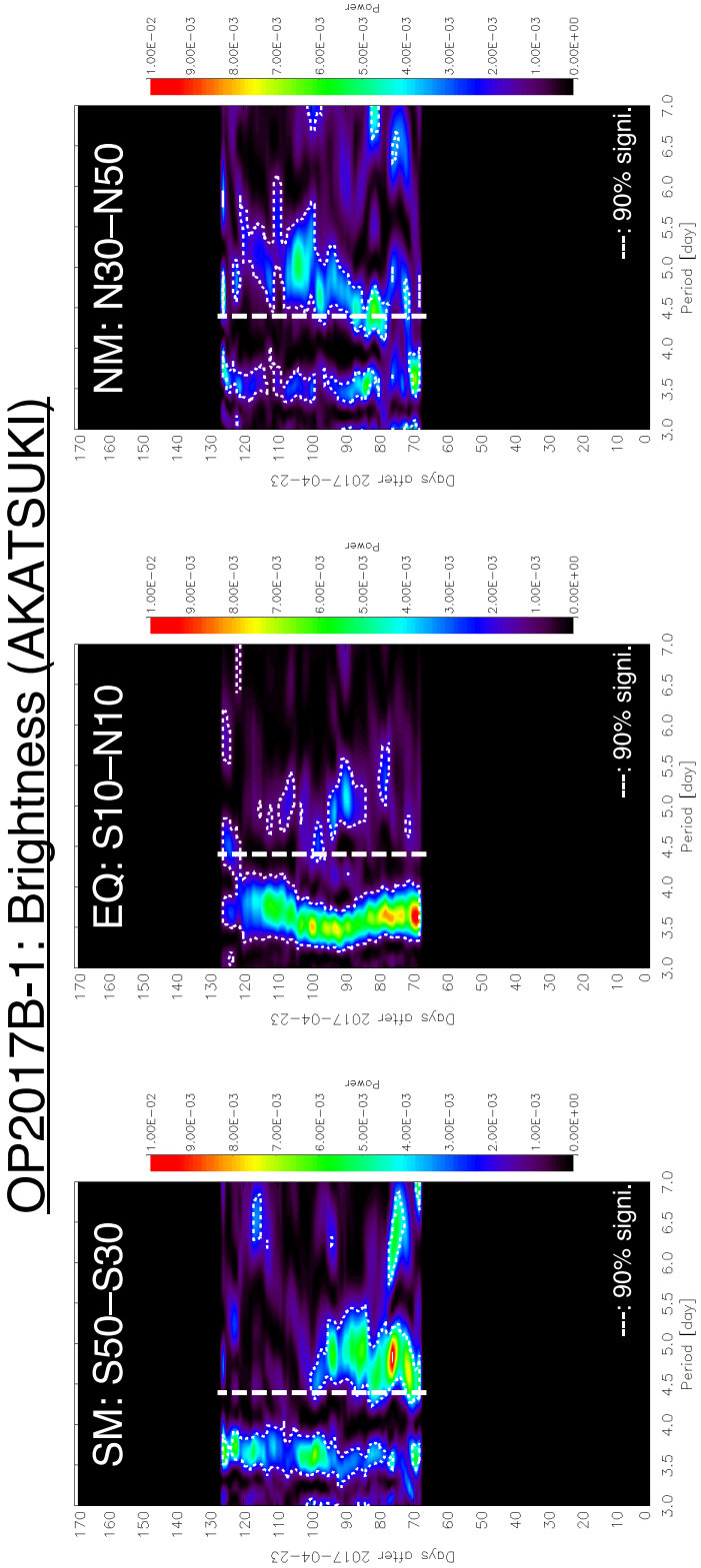

Figure C.7: Time series of periodicities in brightness variation of OP2017B-2 same as Figure C.3

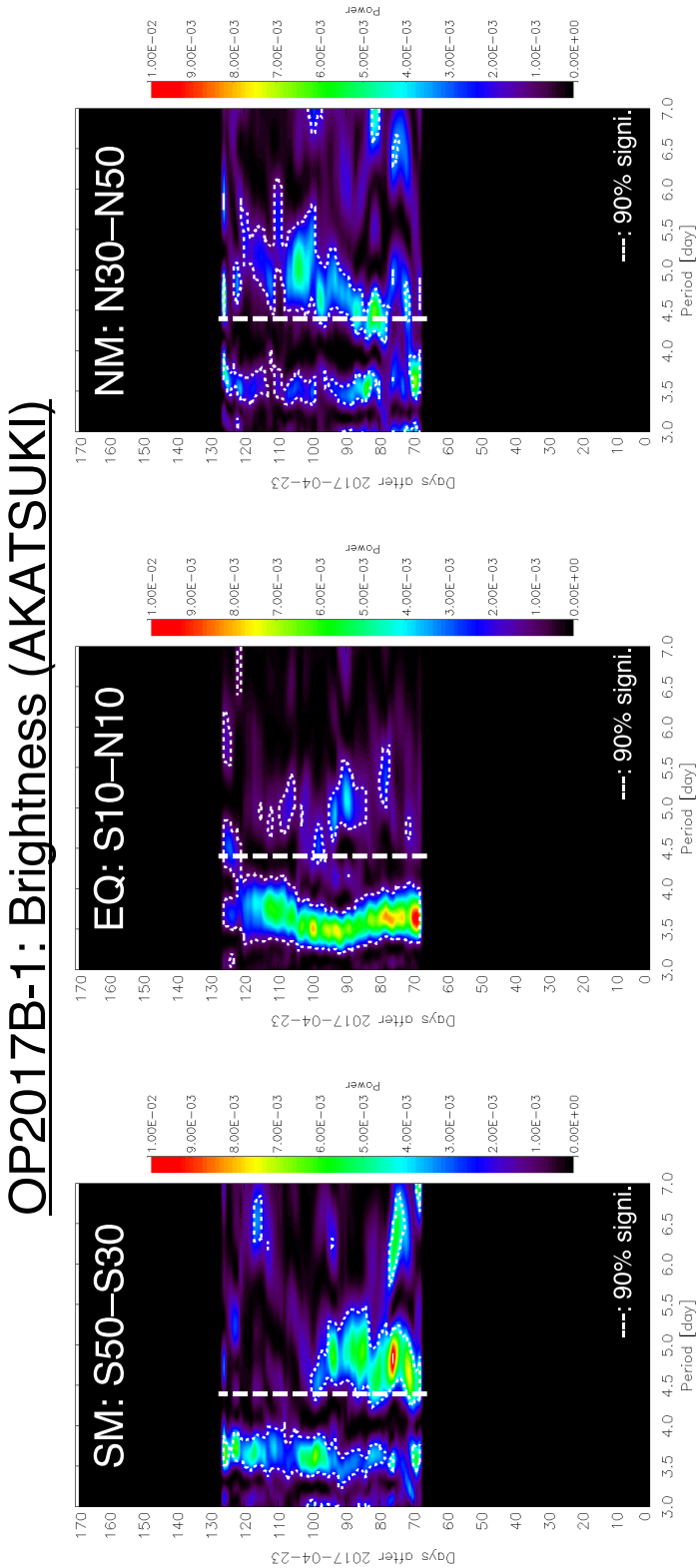

Figure C.8: Time series of periodicities in brightness variation of OP2017B-3 same as Figure C.3

Bibliography

Baldwin, M. P., L. J. Gray, T. J. Dunkerton, K. Hamilton, P. H. Haynes, W. J. Randel, J. R. Holton, M. J. Alexander, I. Hirota, T. Horinouchi, D. B. A. Jones, J. S. Kinnersley, C. Marquardt, K. Sato, and M. Takahashi (2001), The quasi-biennial oscillation, Reviews of Geophysics, 39(2), 179–229, doi:10.1029/1999RG000073.

Barker, E. S., J. H. Woodman, M. A. Perry, B. A. Hapke, and R. Nelson (1975), Relative Spectrophotometry of Venus from 3067 to 5960 Å, Journal of the Atmospheric Sciences, 32(6), 1205–1211, doi:10.1175/1520-0469(1975)032⟨1205:RSOVFT⟩2.0.CO;2.

BELTON, M. J. S., P. J. GIERASCH, M. D. SMITH, P. HELFENSTEIN, P. J. SCHINDER, J. B. POLLACK, K. A. RAGES, A. P. INGERSOLL, K. P. KLAASEN, J. VEVERKA, C. D. ANGER, M. H. CARR, C. R. CHAPMAN, M. E. DAVIES, F. P. FANALE, R. GREELEY, R. GREENBERG, J. W. HEAD, D. MORRISON, G. NEUKUM, and C. B. PILCHER (1991), Images from Galileo of the Venus Cloud Deck, Science, 253(5027), 1531–1536, doi:10.1126/science.253.5027.1531.

Bertaux, J.-L., T. Widemann, A. Hauchecorne, V. I. Moroz, and A. P. Ekonomov (1996), VEGA 1 and VEGA 2 entry probes: An investigation of local UV absorption (220-400 nm) in the atmosphere of Venus (SO 2 aerosols, cloud structure), Journal of Geophysical Research: Planets, 101(E5), 12,709–12,745, doi:10.1029/96JE00466.

Colin, L. (1980), The Pioneer Venus Program, Journal of Geophysical Research, 85(A13), 7575, doi:10.1029/JA085iA13p07575.

Covey, C., and G. Schubert (1981), 4-Day waves in the Venus atmosphere, Icarus, 47(1), 130–138, doi:10.1016/0019-1035(81)90097-X.

Davies, M. E., T. R. Colvin, P. G. Rogers, P. W. Chodas, W. L. Sjogren, E. L. Akim, V. A. Stepanyantz, Z. P. Vlasova, and A. I. Zakharov (1992), The rotation

period, direction of the North Pole, and geodetic control network of Venus, Journal of Geophysical Research, 97(E8), 13,141, doi:10.1029/92JE01166.

Del Genio, A. D., and W. B. Rossow (1990), Planetary-Scale Waves and the Cyclic Nature of Cloud Top Dynamics on Venus, Journal of the Atmospheric Sciences, 47(3), 293–318, doi:10.1175/1520-0469(1990)047⟨0293:PSWATC⟩2.0.CO;2.

Dollfus, A. (1975), Venus: Evolution of the Upper Atmospheric Clouds, Journal of the Atmospheric Sciences, 32(6), 1060–1070, doi:10.1175/1520-0469(1975)032⟨1060:VEOTUA⟩2.0.CO;2.

Ekonomov, A. P., V. I. Moroz, B. E. Moshkin, V. I. Gnedykh, Y. M. Golovin, and A. V. Crigoryev (1984), Scattered UV solar radiation within the clouds of Venus, Nature, 307(5949), 345–347, doi:10.1038/307345a0.

Esposito, L. W. (1980), Ultraviolet contrasts and the absorbers near the Venus cloud tops, Journal of Geophysical Research, 85(A13), 8151, doi:10.1029/JA085iA13p08151.

Fels, S. B., and R. S. Lindzen (1974), The interaction of thermally excited gravity waves with mean flows, Geophysical Fluid Dynamics, 6(2), 149–191, doi:10.1080/03091927409365793.

Gierasch, P. J. (1975), Meridional Circulation and the Maintenance of the Venus Atmospheric Rotation, Journal of the Atmospheric Sciences, 32(6), 1038–1044, doi:10.1175/1520-0469(1975)032⟨1038:MCATMO⟩2.0.CO;2.

Horinouchi, T., S.-y. Murakami, T. Kouyama, K. Ogohara, A. Yamazaki, M. Yamada, and S. Watanabe (2017), Image velocimetry for clouds with relaxation labeling based on deformation consistency, Measurement Science and Technology, 28(8), 085,301, doi:10.1088/1361-6501/aa695c.

Horne, J. H., and S. L. Baliunas (1986), A prescription for period analysis of unevenly sampled time series, The Astrophysical Journal, 302, 757, doi:10.1086/164037.

Hueso, R., J. Peralta, I. Garate-Lopez, T. Bandos, and A. Sánchez-Lavega (2015), Six years of Venus winds at the upper cloud level from UV, visible and near infrared observations from VIRTIS on Venus Express, Planetary and Space Science, 113-114, 78–99, doi:10.1016/j.pss.2014.12.010.

Ikegawa, S., and T. Horinouchi (2016), Improved automatic estimation of winds at the cloud top of Venus using superposition of cross-correlation surfaces, Icarus, 271, 98–119, doi:10.1016/j.icarus.2016.01.018.

Imai, M., Y. Takahashi, M. Watanabe, T. Kouyama, S. Watanabe, S. Gouda, and Y. Gouda (2016), Ground-based observation of the cyclic nature and temporal variability of planetary-scale UV features at the Venus cloud top level, Icarus, 278, 204–214, doi:10.1016/j.icarus.2016.06.011.

Imamura, T. (2006), Meridional Propagation of Planetary-Scale Waves in Vertical Shear: Implication for the Venus Atmosphere, Journal of the Atmospheric Sciences, 63(6), 1623–1636, doi:10.1175/JAS3684.1.

Khatuntsev, I., M. Patsaeva, D. Titov, N. Ignatiev, A. Turin, S. Limaye, W. Markiewicz, M. Almeida, T. Roatsch, and R. Moissl (2013), Cloud level winds from the Venus Express Monitoring Camera imaging, Icarus, 226(1), 140–158, doi:10.1016/j.icarus.2013.05.018.

Kouyama, T., T. Imamura, M. Nakamura, T. Satoh, and Y. Futaana (2012), Horizontal structure of planetary-scale waves at the cloud top of Venus deduced from Galileo SSI images with an improved cloud-tracking technique, Planetary and Space Science, 60(1), 207–216, doi:10.1016/j.pss.2011.08.008.

Kouyama, T., T. Imamura, M. Nakamura, T. Satoh, and Y. Futaana (2015), Vertical propagation of planetary-scale waves in variable background winds in the upper cloud region of Venus, Icarus, 248, 560–568, doi:10.1016/j.icarus.2014.07.011.

Lebonnois, S., N. Sugimoto, and G. Gilli (2016), Wave analysis in the atmosphere of Venus below 100-km altitude, simulated by the LMD Venus GCM, Icarus, 278, 38–51, doi:10.1016/j.icarus.2016.06.004.

Lee, Y., T. Imamura, S. Schröder, and E. Marcq (2015), Long-term variations of the UV contrast on Venus observed by the Venus Monitoring Camera on board Venus Express, Icarus, 253, 1–15, doi:10.1016/j.icarus.2015.02.015.

Lee, Y. J., A. Yamazaki, T. Imamura, M. Yamada, S. Watanabe, T. M. Sato, K. Ogohara, G. L. Hashimoto, and S. Murakami (2017), Scattering Properties of the Venusian Clouds Observed by the UV Imager on board Akatsuki, The Astronomical Journal, 154(2), 44, doi:10.3847/1538-3881/aa78a5.

Limaye, S. S., and V. E. Suomi (1981), Cloud Motions on Venus: Global Structure and Organization, Journal of the Atmospheric Sciences, 38(6), 1220–1235, doi: 10.1175/1520-0469(1981)038⟨1220:CMOVGS⟩2.0.CO;2.

Machado, P., T. Widemann, J. Peralta, R. Gonçalves, J.-F. Donati, and D. Luz (2017), Venus cloud-tracked and doppler velocimetry winds from CFHT/ESPaDOnS and Venus Express/VIRTIS in April 2014, Icarus, 285, 8–26, doi:10.1016/j.icarus.2016.12.017.

Molaverdikhani, K., K. McGouldrick, and L. W. Esposito (2012), The abundance and vertical distribution of the unknown ultraviolet absorber in the venusian atmosphere from analysis of Venus Monitoring Camera images, Icarus, 217(2), 648–660, doi:10.1016/j.icarus.2011.08.008.

Nakamura, M., T. Imamura, N. Ishii, T. Abe, Y. Kawakatsu, C. Hirose, T. Satoh, M. Suzuki, M. Ueno, A. Yamazaki, N. Iwagami, S. Watanabe, M. Taguchi, T. Fukuhara, Y. Takahashi, M. Yamada, M. Imai, S. Ohtsuki, K. Uemizu, G. L. Hashimoto, M. Takagi, Y. Matsuda, K. Ogohara, N. Sato, Y. Kasaba, T. Kouyama, N. Hirata, R. Nakamura, Y. Yamamoto, T. Horinouchi, M. Yamamoto, Y.-Y. Hayashi, H. Kashimura, K.-i. Sugiyama, T. Sakanoi, H. Ando, S.-y. Murakami, T. M. Sato, S. Takagi, K. Nakajima, J. Peralta, Y. J. Lee, J. Nakatsuka, T. Ichikawa, K. Inoue, T. Toda, H. Toyota, S. Tachikawa, S. Narita, T. Hayashiyama, A. Hasegawa, and Y. Kamata (2016), AKATSUKI returns to Venus, Earth, Planets and Space, 68(1), 75, doi:10.1186/s40623-016-0457-6.

Newman, M., and C. Leovy (1992), Maintenance of Strong Rotational Winds in Venus' Middle Atmosphere by Thermal Tides, Science, 257(5070), 647–650, doi: 10.1126/science.257.5070.647.

Peralta, J., R. Hueso, and A. Sánchez-Lavega (2007), Cloud brightness distribution and turbulence in Venus using Galileo violet images, Icarus, 188(2), 305–314, doi:10.1016/j.icarus.2006.12.005.

Peralta, J., A. Sánchez-Lavega, M. A. López-Valverde, D. Luz, and P. Machado (2015), Venus's major cloud feature as an equatorially trapped wave distorted by the wind, Geophysical Research Letters, 42(3), 705–711, doi:10.1002/ 2014GL062280.

Pollack, J. B., O. B. Toon, R. C. Whitten, R. Boese, B. Ragent, M. Tomasko, L. Esposito, L. Travis, and D. Wiedman (1980), Distribution and source of the

UV absorption in Venus' atmosphere, Journal of Geophysical Research, 85(A13), 8141, doi:10.1029/JA085iA13p08141.

Rossow, W. B., and G. P. Williams (1979), Large-Scale Motion in the Venus Stratosphere, Journal of the Atmospheric Sciences, 36(3), 377–389, doi:10.1175/1520-0469(1979)036⟨0377:LSMITV⟩2.0.CO;2.

Rossow, W. B., A. D. Del Genio, S. S. Limaye, L. D. Travis, and P. H. Stone (1980), Cloud morphology and motions from Pioneer Venus images, Journal of Geophysical Research, 85(A13), 8107, doi:10.1029/JA085iA13p08107.

Sánchez-Lavega, A., S. Lebonnois, T. Imamura, P. Read, and D. Luz (2017), The Atmospheric Dynamics of Venus, Space Science Reviews, 212(3-4), 1541–1616, doi:10.1007/s11214-017-0389-x.

Scargle, J. D. (1982), Studies in astronomical time series analysis. II - Statistical aspects of spectral analysis of unevenly spaced data, The Astrophysical Journal, 263, 835, doi:10.1086/160554.

Schubert, G., C. Covey, A. D. Genio, L. S. Elson, G. Keating, A. Seiff, R. E. Young, J. Apt, C. C. Counselman, A. J. Kliore, S. S. Limaye, H. E. Revercomb, L. A. Sromovsky, V. E. Suomi, F. Taylor, R. Woo, and U. von Zahn (1980), Structure and circulation of the Venus atmosphere, Journal of Geophysical Research, 85(A13), 8007, doi:10.1029/JA085iA13p08007.

Shapiro, I. I., D. B. Campbell, and W. M. de Campli (1979), Nonresonance rotation of Venus, The Astrophysical Journal, 230, L123, doi:10.1086/182975.

Sugimoto, N., M. Takagi, and Y. Matsuda (2014), Waves in a Venus general circulation model, Geophysical Research Letters, 41(21), 7461–7467, doi:10.1002/2014GL061807.

Svedhem, H., D. Titov, F. Taylor, and O. Witasse (2009), Venus Express mission, Journal of Geophysical Research, 114(5), E00B33, doi:10.1029/2008JE003290.

Takagi, M., and Y. Matsuda (2006), Dynamical effect of thermal tides in the lower Venus atmosphere, Geophysical Research Letters, 33(13), L13,102, doi:10.1029/2006GL026168.

Takagi, M., and Y. Matsuda (2007), Effects of thermal tides on the Venus atmospheric superrotation, Journal of Geophysical Research, 112(D9), D09,112, doi:10.1029/2006JD007901.

Titov, D. V., F. W. Taylor, H. Svedhem, N. I. Ignatiev, W. J. Markiewicz, G. Piccioni, and P. Drossart (2008), Atmospheric structure and dynamics as the cause of ultraviolet markings in the clouds of Venus, Nature, 456(7222), 620–623, doi:10.1038/nature07466.

TRAVIS, L. D., D. L. COFFEEN, J. E. HANSEN, K. KAWABATA, A. A. LACIS, W. A. LANE, S. S. LIMAYE, and P. H. STONE (1979), Orbiter Cloud Photopolarimeter Investigation, Science, 203(4382), 781–785, doi:10.1126/science.203.4382.781.

Watanabe, M., Y. Takahashi, M. Sato, S. Watanabe, T. Fukuhara, K. Hamamoto, and A. Ozaki (2012), MSI: a visible multispectral imager for 1.6-m telescope of Hokkaido University, in Proc. SPIE, vol. 8446, edited by I. S. McLean, S. K. Ramsay, and H. Takami, p. 84462O, doi:10.1117/12.925292.

Yamamoto, M., and H. Tanaka (1997), Formation and Maintenance of the 4-Day Circulation in the Venus Middle Atmosphere, Journal of the Atmospheric Sciences, 54(11), 1472–1489, doi:10.1175/1520-0469(1997)054⟨1472:FAMOTD⟩2.0.CO;2.